University of Nottingham
UK | CHINA | MALAYSIA

Faculty of Science and Engineering

Department of Mechanical, Materials, and Manufacturing Engineering

Fabrication and Characterizations of Additively Manufactured PVDF-HFP Composites for Potential Force Sensing Applications

Author : Khaled Mohamed Metwalli

Supervisor : Dr. Khameel Bayo Mustapha

Co-Supervisor : Prof. Yousif Abakr

Statement of Declaration

" I declare that this thesis has been composed solely by myself and that it has not been submitted, in whole or in part, in any previous application for a degree. Except where states otherwise by reference or acknowledgment, the work presented is entirely my own."

Table of Contents

List of Figures

List of Tables

Acknowledgments

First and foremost, I would like to express my heartfelt gratitude to my supervisor, Dr. Khameel Bayo Mustapha, whose guidance and encouragement were invaluable throughout my research process. Dr. Mustapha's constructive feedback and insightful advice helped me shape my ideas and approach the research more effectively. He was always attentive to any issues I approached him with, and his motivational support kept me going during challenging times. I owe Dr. Mustapha a great deal of respect and gratitude for his unwavering support. He was always available to offer his guidance and expertise, and his willingness to assist me at every step was invaluable.

I am also immensely grateful to Mr. Mohd Saiful Bahrain, a member of the mechanical engineering workshop staff, who provided invaluable assistance with assembling the extruder and offered continuous help and suggestions for 3D printing. His knowledge and expertise were essential to the success of my project.

I would also like to extend my sincere appreciation to my family and friends, who have been a constant source of encouragement and support throughout my academic journey. Their unwavering love and support have given me the strength to persevere through the challenges and difficulties of graduate study.

Finally, I wish to express my deep appreciation to the Institute of Tropical Forestry and Forest Products (INTROP) at the University of Putra Malaysia (UPM) for granting me permission to use their extruder for my research. I would also like to thank my friend Moustafa Alaa, who provided essential assistance with the machine and showed me around the UPM campus.

I am grateful to everyone who has helped me along the way. Without their invaluable support and encouragement, this work would not have been possible.

List of Publications

K. B. Mustapha and K. M. Metwalli, "A review of fused deposition modelling for 3D printing of smart polymeric materials and composites," *European Polymer Journal,* vol. 156, p. 110591, 2021/08/05/ 2021, doi: https://doi.org/10.1016/j.eurpolymj.2021.110591.

K. B. Mustapha, K. M. Metwalli, A. A. B. Baharuddin, and Y. Abakr, "3D printing of polyvinylidene fluoride composite films with enhanced electroactive betα-phase for flexible wearable pressure sensors," *Materials Today: Proceedings,* vol. 70, pp. 321-327, 2022/01/01/ 2022, doi: https://doi.org/10.1016/j.matpr.2022.09.245.

Nomenclature

Abbreviation	Meaning	Abbreviation	Meaning
AlN	Aluminium Nitride	**PLA**	Polylactic acid
BTO	Barium Titanate	**PLLA**	Poly-L-lactic acid
CAD	Computer-aided design	**PVDF**	Polyvinyldene fluoride
CNT	Carbon nanotube	**PVDF-TrFE**	Polyvinylidene fluoride-tetrafluoroethylene
DMF	Dimethylformamide	**PZT**	Lead zirconate titanate
EPAM	Electric poling assisted additive manufacturing	**FESEM**	Field Emission Scanning electron microscopy
FDM	Fused deposition modelling	**SR**	Stretch ratio
FTIR	Fourier-transform Infrared spectroscopy	**DMA**	Dimethyl acetamide
MPB	Morphotropic phase boundary	**DMF**	Dimethyl formamide
NFES	Near field electrospinning	**DMSO**	Dimethyl sulfoxide
PDA	Polydopamine	**DOE**	Design of Experiment
PDMS	Polydimethylsiloxane	PVDF-HFP	Polyvinylidene fluoride-hexaflouropropylene

Abstract

Polyvinyldene fluoride (PVDF) and its copolymers have attracted considerable interest among researchers as piezoelectric materials since their discovery. Due to their satisfactory piezoelectric properties and excellent mechanical characteristics, they have found various applications, including in flexible force sensors. Researchers often reinforced the polymer matrix with fillers to enhance its performance as force sensors. However, the solvents commonly used in the mixing process were often deemed hazardous and toxic, leading to the search for an alternative. Among the potential fabrication methods, researchers have reported that using Fused Deposition Modeling (FDM) to 3D print PVDF composites has resulted in improved piezoelectric performance. In this study, a copolymer of PVDF, Polyvinyldene fluoride- hexaflouropropylene (PVDF-HFP), was reinforced and 3D printed to investigate the influence of the fillers on its piezoelectric characteristics and identify the effect of the printing parameters on its piezoelectric and mechanical properties. Initially, the pure polymer was 3D printed to investigate the effect of the printing parameters and the Design of Experiment (DOE) method was employed to optimize the printing parameters. The composite was synthesised through the solution casting of a PVDF-HFP matrix reinforced with Barium Titanate and Untreated Activated Carbon. To investigate its viability as an alternative solvent, Dimethylsulfoxide (DMSO) was selected as the solvent. The optimum mixture design of experiments (MDOE) method was employed to assist in investigating the effect of the fillers and help optimize the filler content in the matrix. The utilization of the MDOE was successful, and the formulation of 84.21 wt.% PVDF-HFP, 15.00 wt.% BTO, and 0.79 wt.% UAC predicted by the software recorded the maximum β-phase of 71.895%. It is also worth noting that DMSO was deemed a viable alternative due to the tested formulations recording β-phase content values that are comparable to values reported in literature. The DOE analysis run on the pure PVDF-HFP showed that using a higher printing temperature, lower printing speed, and thinner layer thickness resulted in a maximised β-phase content. The following information were carried forward to aid in printing the PVDF-HFP composite. It was shown that the printed composite recorded a lower force sensitivity when compared to the pure polymer despite the slightly higher β-phase. Despite limited performance, all printed samples still demonstrated piezoelectricity and were capable of detecting forces as low as 1N confirming that FDM-printed PVDF copolymer composites have potential as flexible force sensors.

1. Introduction

1.1 Background

For decades, flexible force sensors have become a part of daily human actions by playing a critical role in several industries such as the biomedical, automotive, and robotics industries. Force sensors are utilised in measuring and monitoring force values for several systems. For instance, flexible force sensors can be used to help robots mimick the human grabbing, monitor the stress on an implanted artificial bone, detect and distinguish the type of human motion, or monitor the deformation of a tyre [1-5].

The three major types of flexible force sensors are capacitive, piezoresistive, and piezoelectric [6]. Capacitive force sensors generally utilise a parallel plate arrangement where one flexible electrode deforms while the other is fixed. When a force is exerted, the flexible electrode is deflected reducing the gap between the electrodes increasing the capacitance; hence, the change in capacitance can be related to the force change. Capacitive force sensors offer a wide range of advantages such as high sensitivity and the toleration of high temperatures [6, 7]. However, the drawbacks to using capacitive force sensors are their sensitivity to lower electrostatic discharge voltages and the high fabrication cost due to the low manufacturing volume [8].

Piezoresistive force sensors detect force change by measuring the deformation of a diaphragm made up of piezoresistive material. This material exhibits changes in electrical resistance when deformed, and these changes can be related to the change in force being applied. The disadvantages of using piezoresistive force sensors include that its output is temperature dependant in addition to requiring higher power for operation when compared to the remaining sensors [9]. Piezoelectric force sensors generate charge under mechanical stress. The charges can be collected using electrodes and a relation between the change in charge or voltage and pressure can be obtained. There are growing appeals for piezoelectric force sensors due to their self-powering and insensitivity to electromagnetic interference and radiation qualifying them for applications in harsh conditions [10].

Among several suitable piezoelectric materials, PVDF-composites stand out due to their flexibility and excellent piezoelectric response [11].

Lead-based piezoelectric ceramic fillers have traditionally been favored due to their better piezoelectric performance when compared to other types of fillers. However, the negative consequences associated with the use of lead-based materials, including environmental pollution and health risks, have prompted researchers to seek out alternative materials such as Barium Titanate (BTO) [12]. In addition to the concerns of using lead-based fillers, the research community is shifting away from using hazardous and toxic solvents to fabricate PVDF composites such as as N,N dimethylformamide (DMF) and Dimethylacetamide (DMA)[13]. Instead, the focus is shifting towards exploring environmentally friendly solvents like dimethyl sulfoxide (DMSO) [14]. Among the available fabrication techniques, the recent developments in 3D printing PVDF composites using the fused deposition modelling (FDM) process provide an unexplored fabrication technique which can be utilised for mass fabrication of complex structures [15].

In this study, the possibility of using poly(vinylidene fluoride-hexafluoropropylene) (PVDF-HFP) copolymer for force sensing applications by investigating the effect of reinforcement on its microstructural properties was explored. To this end, filaments of PVDF-HFP composite were fabricated for use in FDM printing. The study then evaluated the influence of selected FDM printing parameters on the characteristics and electromechanical response of the PVDF-HFP. The information collected were carried forward to help investigate the effect of FDM on the characteristics and electromechanical properties of the PVDF-HFP composite. The composite consisted of using polar solvent DMSO to reinforce PVDF-HFP with Barium Titanate (BTO) and untreated activated carbon (UAC) fillers, aiming to investigate the effect of the fillers on the piezoelectric response and to confirm the viability of DMSO as an alternative solvent for the process. In the following sections, a background on the piezoelectric effect, piezoelectric sensors, piezoelectric material classification, and fabrication methods are presented.

1.2 Objectives

- To fabricate the piezoelectric PVDF copolymer composite through the Fused Deposition Modeling (FDM) process
- To determine the influence of reinforcement on the piezoelectric properties of the additively manufactured PVDF composite
- To investigate the effect of the FDM process on the mechanical and microstructural properties of the printed composites
- To test the electromechanical performance of the PVDF copolymer composite

2. Literature Review

2.1 The piezoelectric effect

Derived from the word piezo, Greek work for push, the piezoelectric effect is the ability of a material to produce electric charges when a mechanical stress is applied on them. It was first discovered in 1880 by the Curie brothers, Pierre and Jacques [16]. The brothers were able to demonstrate the piezoelectric effect in naturally occurring structures such as tourmaline, quartz, and Rochelle salt. The converse piezoelectric effect , application of an electrical field results in a mechanical deformation of the piezoelectric material, was predicted by Lippmann [17] and confirmed by the Curie brothers in 1881. The piezoelectric effect was a topic to study for decades and scientists were able to synthesise piezoelectric materials in laboratory such as the synthesis of Barium Titanate (BTO) by several independent research groups in 1943 and the discovery of the piezoelectric response of Lead Zirconate Titanate (PZT) by Jaffe et. al. [18, 19] in 1954. The progress in research was not exclusive to the synthesis of piezoelectric ceramics as in 1969, Kawai [20] discovered the high piezoelectric response of Poly(vinylidene fluoride) (PVDF) which was added to the list of flexible piezoelectric materials with a wide range of potential applications such as sensors, energy harvesters, and flexible electronics.

2.1.1 Piezoelectric Mechanism

Figure 2.1 illustrates a simple molecular model for the piezoelectric effect's working mechanism. As obvious in Figure 2.1(a), when the material is not under stress, the gravity centres of the positive and negative charges coincide resulting in an electrically neutral molecule. When a force is exerted on the material, the internal structure gets deformed causing the separation of the negative and positive charge centres resulting in the generation of little dipoles (Figure 2.1 (b)). The opposing poles inside the material are cancelled and a charge appears on the surface of the material which means the material is polarized (Figure 2.1(c)) [21]. As demonstrated in Figure 2.2(a), the applied pressure on the material results in its polarization; hence, the generation of an electric field causing the flow of free charges in the conductor. The free charges will flow in the circuit to neutralize the polarization effects. When the force is removed, the polarization disappears, and the flow of the free charges is reversed causing the material to return to its original state (Figure 2.2 (b)) [21, 22].

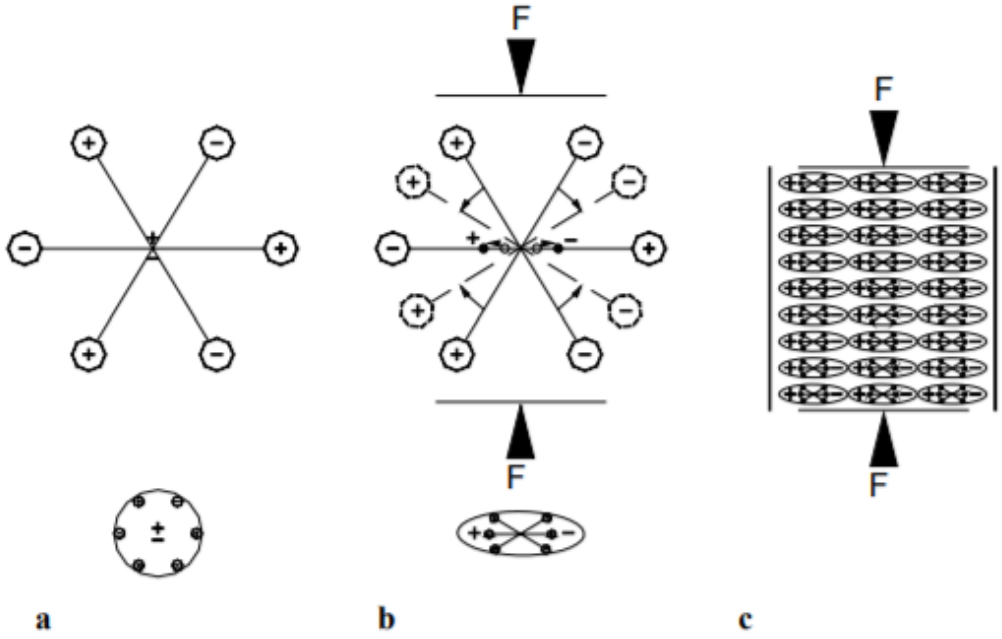

Figure 2.1 : Illustration of the piezoelectric effect a) Undisturbed molecule b) Molecule subjected to a force c) Polarizing effect on the surface [21]

.

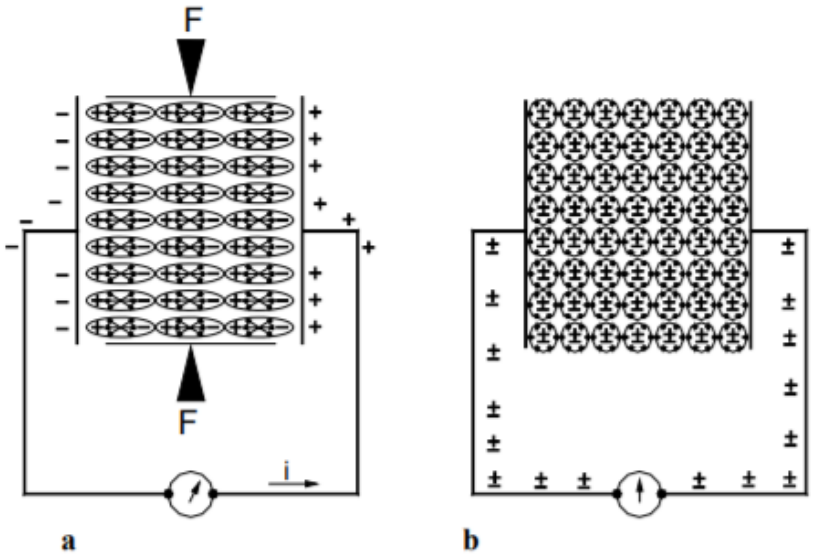

Figure 2.2 : The piezoelectric effect a) Neutralizing current flowing through the circuit based on a piezoelectric material under applied stress (force) b) Absence of current with the absence of the force [21]

In most of the piezoelectric materials, the net polarization is usually equal to zero as dipoles are randomly distributed across the structure as demonstrated in Figure 2.3(a). To align the dipoles in one direction, the poling process needs to be applied. The poling process as shown in Figure 2.3(b) consists of applying a very high dc electric field on the material along a certain direction under a certain temperature. After the electric field is removed, a net dipole moment remains and the material shows maximum piezoelectric response in the direction of poling (Figure 2.3 (c)) [23].

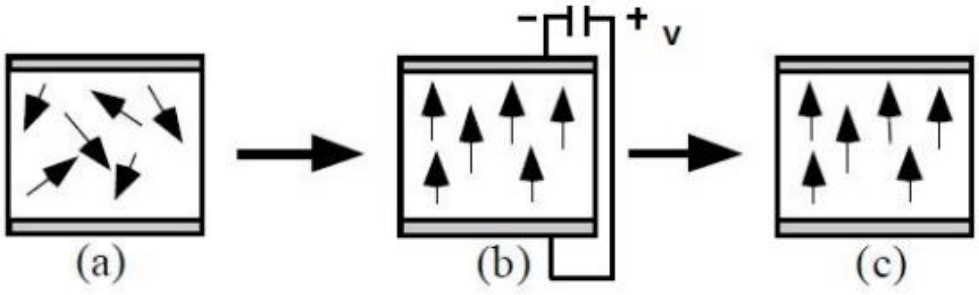

Figure 2.3 : Poling process [23]

2.1.2 Piezoelectric constitutive equations and relevant mathematical relations

The experiments conducted by the Curie brothers demonstrated that the piezoelectric material showed a linear response when low stress/electric fields were applied [21, 24]. When the piezoelectric material is under stress, a variation in the polarization occurs resulting in charge appearing on the surface of the material. The relationship can be described using the following formula [22, 25]:

$$P_p = dT \tag{2.1}$$

where P_P is the piezoelectric polarization vector, d is the piezoelectric strain coefficient, and T is the stress applied on the material. The converse piezoelectric effect can be formulated in a similar manner using the following formula [22, 25]:

$$S_P = dE \tag{2.2}$$

where S_P is the strain produced and E is the value of the applied electric field.
The piezoelectric effect is the coupling between the elastic variables, T and S, and the dielectric variables, D and E. The tensor relations are described using the following formulas [22, 25] :

$$S_i = s_{ij}^E T_j + d_{ik} E_k \tag{2.3}$$

$$D_m = d_{mj} T_j + \varepsilon_{mk}^{\mathrm{T}} E_n \tag{2.4}$$

With the s_{ij}^E as the elastic compliance tensor of the material at constant electric field, ε_{mk}^T as the dielectric constant tensor at a constant stress, d_{ik} and d_{mj} as the piezoelectric constant tensors, S_i is the strain in the i direction, D_m is the electric displacement in the m direction, T_j as the stress in the j direction, and E_k as the electric field applied in the k direction.

The substrates i and j take values between 1 and 6 while m,n, and k take values between 1 and 3. Figure 2.4 shows the tensor directions used in the relations.

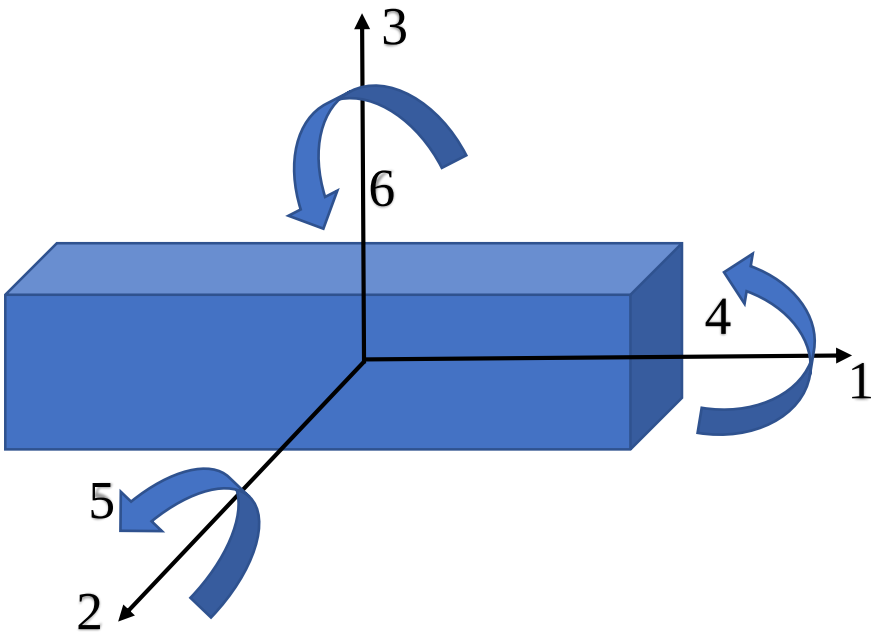

Figure 2.4 : Tensor directions generally used with piezoelectric materials

Equations 2.3 and 2.4 can be expanded into the form:

$$\begin{Bmatrix} S_1 \\ S_2 \\ S_3 \\ S_4 \\ S_5 \\ S_6 \end{Bmatrix} = \begin{bmatrix} s_{11} & s_{12} & s_{13} & s_{14} & s_{15} & s_{16} \\ s_{21} & s_{22} & s_{23} & s_{24} & s_{25} & s_{26} \\ s_{31} & s_{32} & s_{33} & s_{34} & s_{35} & s_{36} \\ s_{41} & s_{42} & s_{43} & s_{44} & s_{45} & s_{46} \\ s_{51} & s_{52} & s_{53} & s_{54} & s_{55} & s_{56} \\ s_{61} & s_{62} & s_{63} & s_{64} & s_{65} & s_{66} \end{bmatrix} \begin{Bmatrix} T_1 \\ T_2 \\ T_3 \\ T_4 \\ T_5 \\ T_6 \end{Bmatrix} + \begin{bmatrix} d_{11} & d_{12} & d_{13} \\ d_{21} & d_{22} & d_{23} \\ d_{31} & d_{32} & d_{33} \\ d_{41} & d_{42} & d_{43} \\ d_{51} & d_{52} & d_{53} \\ d_{61} & d_{62} & d_{63} \end{bmatrix} \begin{Bmatrix} E_1 \\ E_2 \\ E_3 \end{Bmatrix} \tag{2.5}$$

$$\begin{Bmatrix} D_1 \\ D_2 \\ D_3 \end{Bmatrix} = \begin{bmatrix} d_{11} & d_{12} & d_{13} & d_{14} & d_{15} & d_{16} \\ d_{21} & d_{22} & d_{23} & d_{24} & d_{25} & d_{26} \\ d_{31} & d_{32} & d_{33} & d_{34} & d_{35} & d_{36} \end{bmatrix} \begin{Bmatrix} T_1 \\ T_2 \\ T_3 \\ T_4 \\ T_5 \\ T_6 \end{Bmatrix} + \begin{bmatrix} \varepsilon_{11} & \varepsilon_{12} & \varepsilon_{13} \\ \varepsilon_{21} & \varepsilon_{22} & \varepsilon_{23} \\ \varepsilon_{31} & \varepsilon_{32} & \varepsilon_{33} \end{bmatrix} \begin{Bmatrix} E_1 \\ E_2 \\ E_3 \end{Bmatrix} \tag{2.6}$$

Since most piezoelectric materials are orthotropic so the matrix can be reduced to this form [25]:

$$\begin{Bmatrix} S_1 \\ S_2 \\ S_3 \\ S_4 \\ S_5 \\ S_6 \end{Bmatrix} = \begin{bmatrix} \frac{1}{Y_1^E} & -\frac{v_{12}}{Y_1^E} & -\frac{v_{13}}{Y_1^E} & 0 & 0 & 0 \\ -\frac{v_{12}}{Y_1^E} & \frac{1}{Y_1^E} & -\frac{v_{23}}{Y_1^E} & 0 & 0 & 0 \\ -\frac{v_{31}}{Y_3^E} & -\frac{v_{32}}{Y_3^E} & \frac{1}{Y_3^E} & 0 & 0 & 0 \\ 0 & 0 & 0 & \frac{1}{G_{23}^E} & 0 & 0 \\ 0 & 0 & 0 & 0 & \frac{1}{G_{13}^E} & 0 \\ 0 & 0 & 0 & 0 & 0 & \frac{1}{G_{12}^E} \end{bmatrix} \begin{Bmatrix} T_1 \\ T_2 \\ T_3 \\ T_4 \\ T_5 \\ T_6 \end{Bmatrix} + \begin{bmatrix} 0 & 0 & d_{13} \\ 0 & 0 & d_{23} \\ 0 & 0 & d_{33} \\ 0 & d_{24} & 0 \\ d_{15} & 0 & 0 \\ 0 & 0 & 0 \end{bmatrix} \begin{Bmatrix} E_1 \\ E_2 \\ E_3 \end{Bmatrix} \quad (2.7)$$

$$\begin{Bmatrix} D_1 \\ D_2 \\ D_3 \end{Bmatrix} = \begin{bmatrix} 0 & 0 & 0 & 0 & d_{15} & 0 \\ 0 & 0 & 0 & d_{24} & 0 & 0 \\ d_{31} & d_{32} & d_{33} & 0 & 0 & 0 \end{bmatrix} \begin{Bmatrix} T_1 \\ T_2 \\ T_3 \\ T_4 \\ T_5 \\ T_6 \end{Bmatrix} + \begin{bmatrix} \varepsilon_{11} & 0 & 0 \\ 0 & \varepsilon_{22} & 0 \\ 0 & 0 & \varepsilon_{33} \end{bmatrix} \begin{Bmatrix} E_1 \\ E_2 \\ E_3 \end{Bmatrix} \quad (2.8)$$

Where Y^E represents the Young's Modulus at a constant electric field while G^E represents the shear modulus at a constant electric field. The 'v' represents the Poisson's ratio.

2.1.3 Piezoelectric Sensing Mechanisms

Piezoelectric force sensors depend on the direct piezoelectric effect for functioning. Specially, the relation between the applied stress, force or pressure, and the generated charges on the surface. For a sensor configuration, the case is considered to be an open-circuit case, electric field equals zero, therefore can be written as [25]:

$$D_m = d_{mj} T_j \quad (2.9)$$

Equation 2.9 shows that the linear relationship between the electrical displacement and the applied stress relies on the piezoelectric coefficient which certifies the importance of the role played by the piezoelectric coefficient in the sensor sensitivity. For force sensors, the main functioning modes are the d_{33} and d_{31}. In the $d33$ mode, the force is to be exerted across the thickness, and on the surface normal to the upper or lower surface along the 3-axis which is the polarization direction (Figure 2.5 (a)). On the other hand, the force is to be exerted in along the 1-axis and perpendicular to the polarization direction in the d_{31} mode (Figure 2.5 (b)) [26].

.

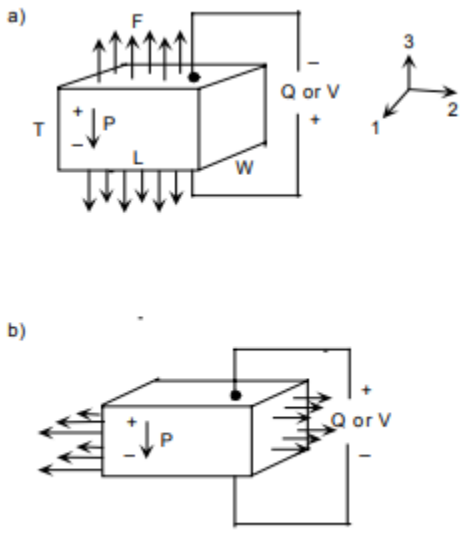

Figure 2.5 Operating modes a) d_{33} operating mode b)d_{31} operating mode [26]

The relationship between charge, voltage, and force exerted for both modes can be derived from Equation 2.9 [26].

$$Q_3 = d_{33}F_3 \tag{2.10}$$

$$Q_3 = \frac{d_{31}F_3L}{t} \tag{2.11}$$

$$V_3 = \frac{d_{33}F_3t}{\varepsilon_{33}LW} \tag{2.12}$$

$$V_3 = \frac{d_{31}F_3}{\varepsilon_{11}L} \tag{2.13}$$

Q is the charge collected at the electrodes, where L and W refer to the length and width of the elecrtodes, and t represents thickness of the piezoelectric material, respectively. It is clear that the force applied are proportional to the voltage generated so if proper configurations are arranged to obtain the electrical output values when a force is exerted, the sensor can be calibrated and utilized in several sensing applications.

2.2 Benefits and drawbacks of piezoelectric force sensors

Extensive research is still being carried out on piezoelectric force sensors due to their inherent advantages over other sensing mechanisms [27]. For instance, most sensors require high deformation to exhibit sensitivity which could unintentionally result in affecting the structure of the sensor [28].

On the contrary, piezoelectric sensors directly respond to the applied force; hence, the sensor exhibits high sensitivity with very low strain [28]. Another advantage is that piezoelectric sensors do not require an external voltage or a current source unlike other sensing mechanisms. In addition, piezoelectric sensors are insensitive to electromagnetic interference and radiation as well as showing distinctive ruggedness which qualifies them to function efficiently under harsh conditions [10].

The major drawback of piezoelectric force sensors is their inability to measure static forces due to the decay of charge generated on the surface. In detail, when the force is applied on the piezoelectric material, the polarization of the material changes resulting in charge generation on the surface. Free carriers of opposite polarity are attracted to the charges on the surface causing the balance of potential and the decay of charge with time until it reaches zero [29]. Due to this phenomenon, piezoelectric sensors can only be used for dynamic measurements.

Piezoelectric force sensors can be utilized in different applications that require dynamic measurements such as ballistics [30] and turbulence [31] due to their rapid response and ruggedness..

2.3 Piezoelectric material classification

2.3.1 Piezoelectric single crystals

Piezoelectric single crystals were the first group of piezoelectric materials to be discovered in the experiments conducted by the Curie brothers. Piezoelectric single crystals can be found in nature and can be synthesised in labs. The most popular natural single crystals are Quartz, Topaz, Tourmaline, and Rochelle salt [32]. Some of their potential applications are piezo lighters and piezoelectric pickups for acoustic devices [33]. Some examples of man-made single crystals are Lithium niobate (LN), $Pb(Mg_{1/3}Nb_{2/3})–PbTiO_3$ (PMN–PT), and $Pb(In_{1/2}Nb_{1/2})–Pb(Mg_{1/3}Nb_{2/3})–PbTiO_3$ (PIN–PMN–PT)[34]. They are mainly utilized in electro-optical and acoustic applications [35-38]. For a single crystal to exhibit piezoelectricity, a critical criterion should be fulfilled which is the lack of centre of symmetry [39]. Single crystals lacking a centre of symmetry may potentially exhibit piezoelectricity. Figure 2.6 highlights the structural difference between crystal structures exhibiting and lacking the centre of symmetry [40]. When a force is applied on the cubic crystal structure exhibiting centre symmetry shown in Figure 2.6(a), the centre of charge will not move due to the symmetry of

the charges at their respective corners; hence, the polarization of the crystal is zero. In contrast, a force on the hexagonal crystal structure lacking centre symmetry shown in Figure 2.6(b) results in shifting the centres of positive and negative charges against each other due to their triangular symmetry; therefore, the polarization of the crystal is not zero [41]. Out of all 32 crystal classes, 21 point groups are non-centro-symmetric, and 20 of them exhibit piezoelectricity. Point group 432 is the only crystal class lacking a centre of symmetry not exhibiting piezoelectricity as the produced piezoelectric charges along the <111> axes cancel themselves out [42, 43].

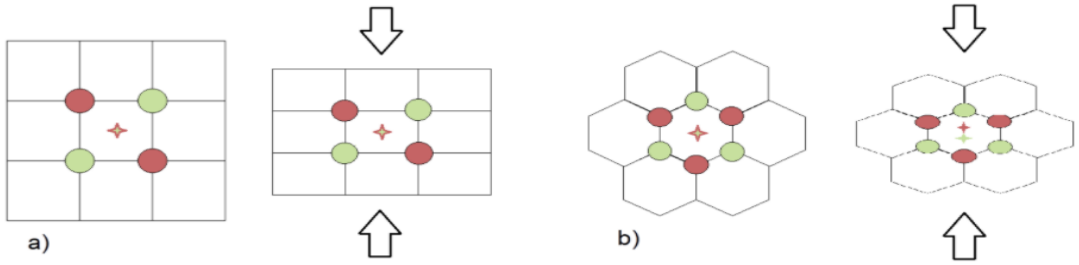

Figure 2.6: Crystal Structures a) with a centre of symmetry; b) without a centre of symmetry [42]

2.3.2 Piezoelectric polymers

Piezoelectric polymers are distinguished by their flexibility, low density, high strength, high impact ratio, and low dielectric constant. Piezoelectric polymers make better sensors when compared to piezoelectric ceramics due to having a higher piezoelectric voltage coefficient, g [44]. Piezoelectric polymers can be divided into amorphous and semicrystalline polymers. Table 2.1 compares several piezoelectric polymers in terms of their classification, dielectric constant, and piezoelectric coefficient.

For semicrystalline polymers, the piezoelectricity depends on the crystalline phase with a net dipole moment which can be oriented using the poling process [45]. Semicrystalline polymers include PVDF, nylon-9, polyureas, poly-L-lactic acid (PLLA), and poly (b-hydroxybutyrate) (PHB).

Table 2.1: Comparison between different piezoelectric polymers

Material	Classification	Dielectric Constant	Piezoelectric coefficient/s at room temperature	reference
PVDF	Semi-crystalline	8-12	d_{31} = 16 pC/N d_{32} = 3 pC/N d_{33} = -20 - -23 pC/N	[45]
Polyurea 5	Semi-crystalline	2-4	d_{31} = 4 pC/N	[46, 47]
Nylon 9	Semi-crystalline	2.5-3	d_{31} = 1.1 pC/N	[48]
Nylon-11	Semi-crystalline	2.5-3	d_{31}= 3 pC/N	[48-50]
PLLA	Semi-crystalline	2.82	d_{31} = 1.58 pC/N d_{14} = 9.82 pC/N	[51, 52]
Polyimide (poly2-6)	Amorphous	4	d_{33} = 0.091 pC/N	[53]
Polyimide (poly2CN)	Amorphous	4	d_{33} = 0.168 pC/N	[53]
P(VDCN-VAc)	Amorphous	5.6	d_{31}= 7 pC/N	[54]

The most popular and studied semicrystalline polymer is PVDF due to having a higher piezoelectric coefficient compared to the remaining piezoelectric polymers. According to numerous sources, PVDF has the potential to exist in five different polymorph states, namely $\alpha, \beta, \gamma, \delta, \varepsilon$ [55-57]. Among these, the α-phase is considered the most stable while the β-phase has the highest dipolar moment. The stability of the α-phases arises from its nonpolar, orthorhombic crystal structure. The chains in the α-phase are packed in an all-trans conformation, with a zigzag pattern that gives the crystal a layered structure.

The β-phase, on the other hand, has a polar triclinic crystal structure with the chains are packed in a trans-gauche-trans-gauche conformation, with a helical arrangement that gives the crystal

a three-dimensional structure resulting in a higher dipole moment. The structural difference between both polymorphs is illustrated in Figure 2.7 [58].

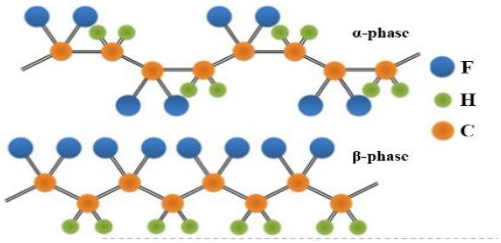

Figure 2.7: structural difference between the α- and β- phases in PVDF [58]

According to various experimental studies, the β-phase contributes the most to the piezoelectric, pyroelectric and ferroelectric properties of the PVDF [59, 60]. Under favourable conditions, transition occurs between the polymorph states [61]. For instance, β-phase can be obtained by uniaxially stretching the α-phase film to 4-5 times the nominal dimension under a temperature between 70 °C and 100 °C. The utilization of several methods such as corona poling, laser-enabled poling, thermo-mechanical treatment, humidity, high-pressure crystallization, annealing, and addition of various fillers can induce the polymorph states' transition to β-phase [61-66]. Some additional processes to obtain the β-phase are portrayed in Figure 2.8.

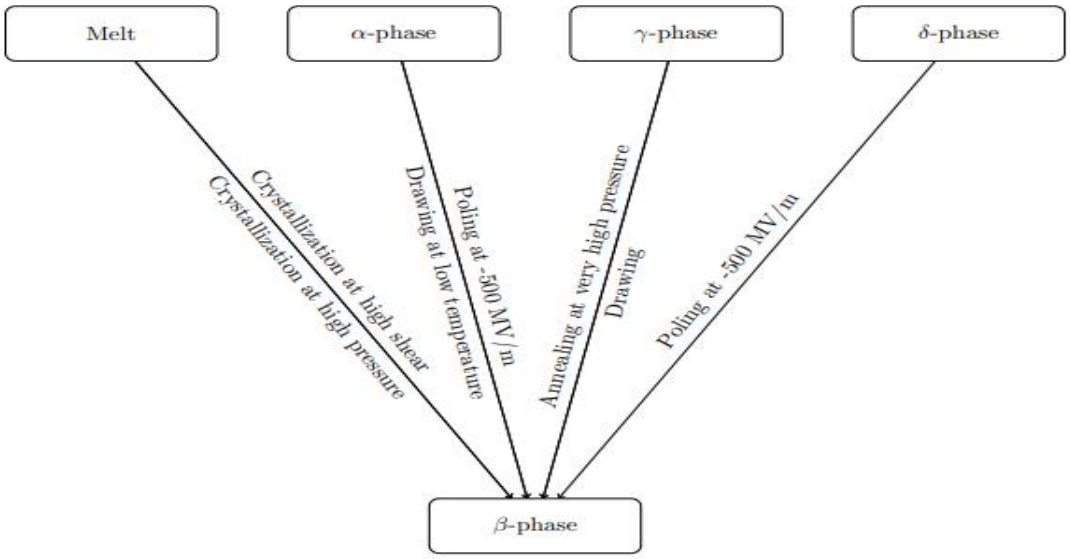

Figure 2.8: Schematic summary of the processes utilised to obtain β-phase

On the other hand, amorphous polymers do not have crystalline phases, and the state of polarization is rather quasi-stable due to the freezing of molecular dipoles[67].

According to M. G. Broadhurst and G. T. Davis [68], for an amorphous polymer to exhibit piezoelectricity, it must satisfy four essential conditions.

First, a molecular dipole should be available. The second condition to be met is the ability of the polymer to align the dipoles. The polarization is induced by applying an electric field at a temperature higher than the transition temperature, $T>T_g$, followed by reducing the temperature below T_g in the presence of the electric field resulting in remnant polarization due to the freezing of aligned dipoles. The third condition depends on the polymer having a mechanism to lock the aligned dipoles. The final criterion is the ability of the polymer to strain as a response to applied stress. Since the remnant polarization disappears in the contiguity of T_g, the polymer needs to be used in its glassy state; hence, the polymer is very stiff. Polyimides, poly(vinylidene cyanide-vinyl acetate) (P(VDCN-Vac)), and poly(arylene ether nitrile) (PAEN) are the most reported amorphous polymers exhibiting piezoelectricity in literature [53, 54, 69]. The literature on amorphous piezoelectric polymers is very limited due to the poor commercial interest. The lack of interest is induced by the low piezoelectric response of amorphous polymers[67].

2.3.3 Piezoelectric ceramics

Piezoelectric ceramics are distinguished by their very high piezoelectric coefficients and dielectric constants. In addition to other favourable properties such as chemical inertness and high compressive strength [70].

The most widely used and researched piezoelectric ceramics are barium titanate (BTO) , lead zirconate titanate (PZT), and potassium niobate (KNN, $K_{0.5}Na_{0.5}NbO_3$). Table 2.2 reports several piezoelectric ceramics included in literature along their dielectric constants and piezoelectric coefficients.

Table 2.2 : Comparison between several piezoelectric ceramics

Material	**Dielectric constant**	**Piezoelectric coefficient/s at room temperature**	**Reference**
BTO	1260-1700	d_{31} = -78 pC/N d_{33} = 190 pC/N	[71]
PZT	200-5000	d_{33} = 100-1000 pC/N	[45]
KNN	250	d33 ~ 60 pC/N	[72]
0.98KNN-0.02BZT	581	d_{33} = 109 pC/N	[72]
0.95KNN – 0.05LT	570	d_{33} ~ 200 pC/N	[73]
Zinc Oxide (ZnO)	8.66	d_{31} = -5 pC/N d_{33} = 5.9 pC/N	[74]

Most commercially available piezoelectric ceramics crystallize in the perovskite structure (ABO_3) [75]. Figure 2.9 shows a simple illustration of the perovskite structure in BTO. For simplicity, the structure is described as a cubic unit cell with large cations (A) on the surface, smaller cations (B) in the body centre, and Oxygens (O) in the faces' centres. The perovskite structure is the network of corner-sharing oxygen octahedra linked together in a cubic array with smaller cations filling the central octahedral holes and larger cations occupying the dodecahedral holes[76, 77].

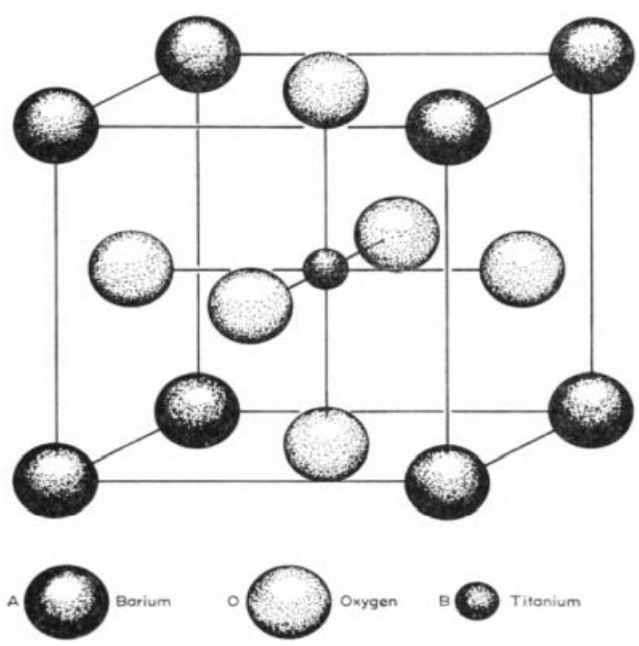

Figure 2.9: Perovskite crystalline structure for BTO [18]

For instance, Barium Titanate shows a perovskite structure above its Curie temperature. Since the perovskite structure provides a symmetrical arrangement for electrical charges, an internal dipole moment is not produced; hence, the ceramic does not exhibit piezoelectricity. Below its Curie temperature, the structure distorts into a tetragonal structure resulting in the shifting of the small cation (Ti^{4+}) off the centre. A net dipole moment is generated as an outcome to the displacement of the small cation [18, 76, 78]. As first verified by R.B. Gray [79], BT exhibits piezoelectricity when electrically poled due to the alignment of the dipoles. Despite the significantly high coupling coefficient and non-water solubility of BT, the low Curie temperature and the large temperature coefficient of electromechanical parameters of BT fuelled the search for an alternative. The investigation using several ions such as Pb and Ca resulted in the synthesis of PZT [80].

Also crystallizing in the perovskite structure, (PZT) is a ceramic material with chemical formula $Pb(Zr_xTi_{1-x})O_3$ [81]. A very interesting feature of PZT is the presence of the morphotropic phase boundary (MPB) . The MPB separates the ferroelectric phase into two regions: a rhombohedral crystalline phase region rich in Zr ions and a tetragonal crystalline phase region rich in Ti ions [77] . At room temperature, the MPB exists in the region where Zr/Ti = 52/48 [82, 83].

As reported in many sources, PZT compositions near the MPB shows the highest dielectric constant and piezoelectric response compared to other regions. Due to the aforementioned

properties, PZT was the most demanded piezoelectric ceramic for decades [77]. However, increased concerns regarding the health and environmental issues associated with the utilisation of lead throughout its life cycle sparked the investigation for a lead-free piezoelectric material [84, 85]. Recently, niobium-based piezoelectric ceramics such as KNN leaded the search for a lead-free piezoelectric ceramic due to its high dielectric constant and piezoelectric response [86]. As KNN shows a lower piezoelectric response compared to KNN, several studies have been conducted to improve its piezoelectricity by the modification of the parent KNN structure by the replacement of cations in the A or B site of the KNN structure such as the modification with $LiTaO_3$ (LT) or $Bi(Zn_{0.5}Ti_{0.5})O_3$ (BZT) done by Guo, et al. [73] and Dwivedi, et al. [72], respectively.

2.3.4 Piezoelectric composites

To overcome the brittle nature of piezoelectric ceramics and the relatively low electrical properties -compared to that of ceramics- of piezoelectric polymers, piezoelectric composites were developed. A piezoelectric composite generally consists of a polymer matrix reinforced with piezoelectric ceramic fillers which integrates the desired traits of polymers and ceramics. The traits combination yields a material with low density, flexibility, excellent mechanical properties, and enhanced piezoelectric response which would meet the requirements for specific devices or applications [87, 88].

Apart from ceramics fillers, conductive, magnetorestrictive, natural, and organic piezoelectric fillers can also be utilised. For instance, conductive fillers such as Carbon nanotubes (CNT) are generally used with other fillers as they enhance the piezoelectric flux generation in addition to their ability to resolve the low coupling coefficients issue arising in piezoelectric composites[89, 90]. While natural piezoelectric fillers such as Rochelle Salt offer a cheaper environment friendly alternative to ceramic fillers [91, 92]. Whereas reinforcing a piezoelectric polymer matrix with magnetostrictive fillers such as $Zn_{0.2}Mn_{0.8}Fe_2O_4$ (ZMFO) results in a magnetoelectric composite where the electrical polarisation can be manipulated by a magnetic field or by the magnetization induced by an applied electric field due to the combined piezoelectric and magnetostrictive phases [93, 94].

Several factors affect the piezoelectric performance of piezoelectric composites including, but not limited to, the filler's particle size, volume fraction of the filler, temperature, and poling parameters [88]. For instance, an increase in the particles size enhances the piezoelectric

coefficient, $d33$, due to the reduction of the interfacial porosity of the composite[95, 96]. It was also reported in many sources that an increase in the filler's volume fraction yields a higher $d33$ and dielectric constant values [97-101]. The reason behind that is the dominant contribution of the ceramic fillers to the electrical properties of the composite.

Temperature is also a key factor in determining the piezoelectric properties the composites as the calcination temperature of piezoelectric ceramics and the transition temperature of polymers affect the dielectric and piezoelectric performance of the composites [88, 102, 103]. Poling plays a great role in improving the piezoelectricity of composites as an increase in the poling electric field results in a composite with higher d_{33}. It is worth mentioning that increasing the field past a certain value results in a constant value of d_{33} due to reaching the composite's saturation poling [104, 105]. Other factors affecting the piezoelectric properties are illustrated in Figure 2.10 [88]. The piezoelectric coefficients and dielectric constants of several piezoelectric composites reported in literature are shown in Table 2.3.

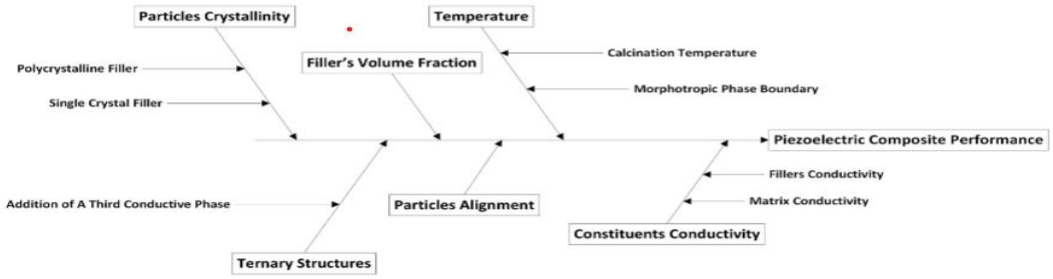

Figure 2.10 : Fishbone diagram stating the key factors affecting the piezoelectric performance of composites [88]

Table 2.3: Summary of composites included in literature

Polymer Matrix	**Reinforcing ceramic filler**	**Volume fraction of filler**	**Dielectric constant**	**Piezoelectric coefficient d_{33} (pC/N)**	**Reference**
PVDF	PZT	10%	9.84	4	[106]
PVDF	PZT	50%	68.1	14	[107]
PVDF	PZT	80%	-	95	[108]

PVDF	BTO	-	23.89	7.8	[109, 110]
PVC	PZT	30%	8.61	4	[111]
PVC	PZT	60%	73.11	22	[111]
Epoxy	BTO	32%	-	~3	[112]
Epoxy	Lead titanate (PT)	70%	-	70	[113, 114]
Polyurethane	PZT	33%	24	23.7	[115-117]
Polyester resin	PZT	60%	84	26	[118]

2.4 Fabrication Methods

The fabrication of piezoelectric sensors is not exclusive to a certain method; therefore, the potential fabrication techniques are to be highlighted in this section. Table 2.4 compares different fabrication methods for piezoelectric sensors reported in literature in terms of sensor dimensions, sensitivity, working mode, and experimenting range.

Table 2.4 : Comparison between piezoelectric sensors fabrication methods

Sensor	Working mode	Dimensions	Manufacturing method	Experimenting range	Max Sensitivity
[119] pressure sensor for human motion monitoring		2.6x2.3 cm^2 T= 36-42micro	Facial solution casting	12-243N	9.3V/12N(33KPa) for 17% PDA@BTO/PVDF
[120] pressure/force sensor with µ-PDMS layer			Photo-lithography	0.23-10KPa 0.01N-0.44N	31.8pC/10kPa for sensor with the µ-PDMS layer
[121] self powered pressure sensor from NFES PVDF fibres		Substrate 40*20*2	Near field electrospinning of PVDF fibres on metallised 3d printed substrate.		
[122] force sensor manufactured from PVDF fabric			electrospinning	3-5N	42mV/N
[123] pressure sensor for catheter applications	Compression Lateral stretching	1x1 & 1.5x1.5cm^2 T= 1 & 6 µm	Lithography for Spin coated PVDF-TrFe	0-300mmHg	
[124] biodegradable	Shear mode	Film 5x5 mm^2 T = 27 µm	Thermal annealing and	0-18kpa	

force sensor (PLLA)			mechanical stretching		
[125] flexible pressure sensor using AlN thin films	Compression deflection	T=1 µm	Radio frequency magnetron reactive sputtering system	0-8.5MPa	30pC/N (deflection) 0.7pC/N (compression)
[126] 3d force sensor based on one layer of PVDF	Compression		Heating and Stretching		0.41V/N for the Z-axis
[127] force sensor based on synthesised PVDF nanofibres			Electrospinning		160mV/kPa
[128] piezoelectric force sensor for minimally invasive surgeries	Deflection Compression	30*10 mm^2 for middle section T= 25 µm	photolithography	1mN-5N	
[129] testing the sensing ability of 3D printed PVDF			EPAM		0.36nA/N
[130] Enhanced Piezoelectric response for 3D printed PVDF composites	Tension	6*35 mm^2 T = 0.55mm	FDM	10-80N	9.06mV/N For 18 wt% BTO, 0.4 wt% MWCNT

[131] 3D printing of PVDF/PR blends for pressure sensing applications	Tension	Stereolithography (SLA)	20-80N	2.25pA/N for 2 wt% PVDF
[132] 3D printed stretchable piezoelectric sensor	Compression	Digital Light Processing (DLP)	30-60N	59.8mV/N

2.4.1 Electrospinning

Electrospinning, derived from "electrostatic spinning", is regarded as one of the most efficient methods to fabricate nanofiber films due to its simple operating mechanism and low cost. Figure 2.11 depicts the mechanism of an electrospinning system. Influenced by the high voltage, liquid droplets of a polymer solution come out of a nozzle. An adequate voltage application on the liquid droplet results in charging the body of the liquid, and the surface tension is counteracted by the electrostatic repulsion which causes the stretching of the droplet at a critical point of liquid stream eruption that is known as the Taylor cone; hence, fibres are fabricated and deposited at a collector plate [133, 134].

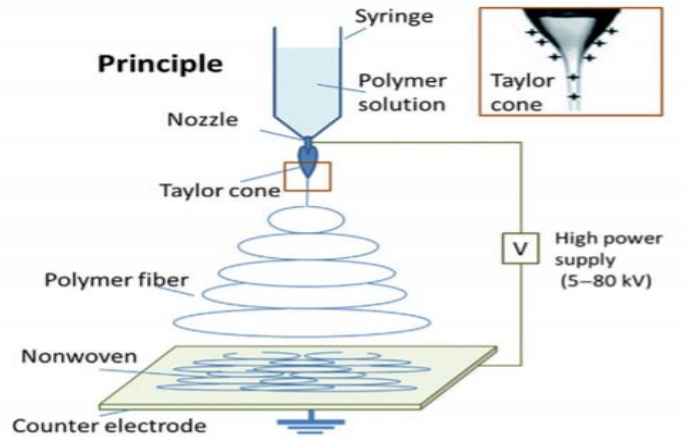

Figure 2.11 : Electrospinning's working mechanism [131]

For instance, Saha, et al. [127] fabricated a piezoelectric force sensor by the synthesis of PVDF nanofibers using the electrospinning process. To achieve the optimal size of PVDF nanofibers, the ratio of solvents , Dimethylformamide (DMF) and acetone , were varied. The solvent ratio of 7:3 offered the thinnest beads free nanofibers among the other ratios. The weight fraction of PVDF was varied to obtain the maximum sensitivity. The sensor fabricated by a solvent ratio of 7:3 and 12 wt% PVDF recorded the maximum sensitivity of 160mV/kPa.

While Wang, et al. [122] manufactured a force sensor based on electrospun PVDF fibres and studied the effect of flow rate and applied voltage on the crystalline morphology and the sensitivity of the sensor. The scanning electron microscopy (SEM) and Fourier-transform infrared spectroscopy (FTIR) test results showed that the optimum conditions for electrospinning are an applied voltage and flow rate of 12kV and 0.02 ml min^{-1}, respectively. The samples processed using those parameters showed the narrowest diameter distribution and the most β-phase formation compared to the other samples. The results from the cyclic tests confirmed the relation between crystalline morphology and sensitivity as the samples produced under the optimum parameters had the highest sensitivity of 42mV N^{-1}.

Whereas Fuh, et al. [121] fabricated a self-powered pressure sensor by the deposition of PVDF fibres produced by the near field electrospinning (NFES) on the top of a topologically tailored metallised 3D printed substrate. The topologies experimented were the planar, square, and sinusoidal surface substrates. The results from pressing the sensor or applying 0.5% cyclic strain at 4hz showed that the sinusoidal surface substrate produced the most voltage and current. Under 0.5% cyclic strain, the sinusoidal surface substrate produced 4V while the planar and the square surfaces produced 2V and 3.5V, respectively. The reason behind the sinusoidal surface's better output is having longer electrospun fibres. The effect of the sinusoidal amplitude was analysed, and it was shown that the voltage produced is proportional to the sinusoidal amplitude due to having longer electrospun fibres and experiencing more strain during the stretching/releasing stages. The sensors were arrayed in matrix to produce a foot pressure mapping sensor. The foot exerts different values of pressure along its area so each sensor will be measuring a different pressure value contributing to mapping the pressure values across the foot.

2.4.2 Photolithography

Photolithography is another technique that is widely used to pattern parts on a thin film or the bulk of a substrate, wafer. Its working mechanism depends on imaging a structure written in a lithographic mask onto a photosensitive resist deposited on the wafer. There are two options to be followed in photolithography, either positive or negative resist. An illustration of the process using the positive resist is shown in Figure 2.12. the first step involves a deposition of the metal on the substrate. (Figure 2.12 (a)). The next step is spin coating the photoresist on the sample followed by the softbake process, leaving the sample at temperatures between 60°C and 100°C for up to 30 minutes, (Figure 2.12 (b)). Afterwards, an illumination of the sample through a mask and suitable light is done (Figure 2.12 (c)). Therefore, the structure of the mask is imaged on the resist causing photochemical changes. After hard-baking for 20-30 minutes at temperatures between 120°C and 180°C (Figure 2.12(d)), the open metal areas are etched away (Figure 2.12 (e)) removing the photoresist and leaving the metal on the substrate (Figure 2.12 (f)). As Figure 2.13 depicts, a similar process occurs for the negative resist, the photoresist is spin coated on the substrate leaving voids which are filled by the deposited metal. The resist is chemically removed leaving the metal on the substrate [135]. The photolithography technique has been used to fabricate piezoelectric pressure and force sensors as in [120, 123, 128]

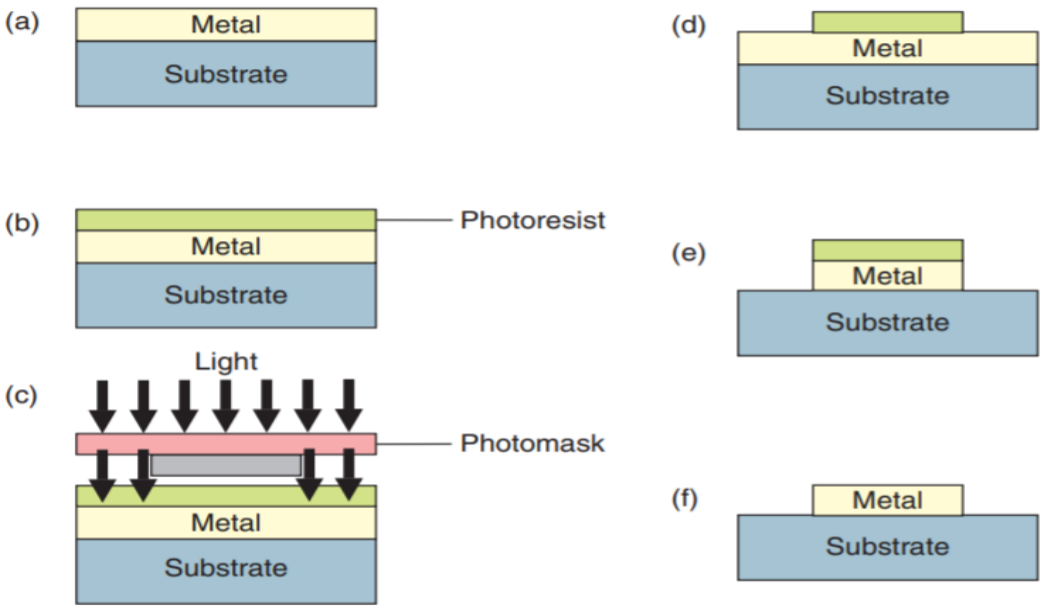

Figure 2.12: Illustration of using positive resist [135]

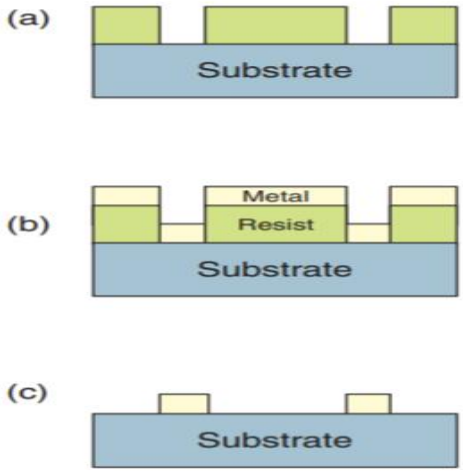

Figure 2.13: Illustration of using negative resist [135]

Sharma, et al. [123] designed and fabricated a pressure sensor as a potential candidate in catheter applications. The process of fabrication was the standard photolithography along spin coating of PVDF-TrFe. The effect of the thickness of the film and the type of electrodes design on the sensitivity was studied. According to Equation 2.14, as the thickness of the film increases, the output voltage should increase. The results from the experiments contradicted the equation, as the sensor of the thinner thickness(1μm) had 1.7 times the sensitivity of the thicker film sensor (6 μm). A potential reason for the contradiction was that the spin coating caused a higher surface tension in the thinner film causing a higher crystallinity when compared to the thicker film. It was found out that the sandwich type electrode design had 3 times higher sensitivity when compared to the parallel type as the piezoelectric coefficient for operating in the compression mode is 2 times higher than the coefficient operating in lateral stretching.

$$V = \frac{F d g_{3n}}{A} \tag{2.14}$$

Where d, A, and g_{3n} represent the thickness of the film, area of the electrodes, and piezoelectric voltage coefficient, respectively.

Choi, et al. [120] designed and manufactured a pressure/force sensor by integrating a piezoelectric sensor based on the photolithography of a PZT thin film with a microstructured polydimethylsiloxane (μ-PDMS) layer and irreversibly bonding them using a PDMS adhesive layer. The design was based on mimicking human skin, the μ-PDMS layer was mimicking the dermis and was integrated to act as a viscoelastic layer to enhance the sensitivity of the sensor. The results showed that the sensor with μ-PDMS layer showed a linear correlation between

charge and force while the sensor without the µ-PDMS layer showed a non-linear correlation after a certain region.

Results showed that the pressure response time and the sensitivity for the sensor with the µ-PDMS layer were recorded to be 5.4ms/KPa and 31.84pC/KPa, respectively. It was also shown that the sensitivity of the sensor with µ-PDMS layer was approximately 3 times the max sensitivity of a sensor without the µ-PDMS layer proving that the integration of the µ-PDMS layer enhanced the sensitivity. The sensor was able to distinguish small differences in pressure by discriminating a quick gentle sweep and slow strong sweep.

Qasaimeh, et al. [128] designed, modelled, and fabricated a piezoelectric force sensor to be integrated with graspers for a potential application in minimally invasive surgeries. The proposed sensor is able to measure and detect the applied force and its location. The force position is a crucial feature as it can notify surgeons of the presence of hidden anatomical features like lumps, voids, and pulsating arteries. The sensor consists of 3 layers. The top layer will be a micromachined Silicon plane fabricated by the photolithography technique integrated with a tooth design for the grasping function. The second layer consists of 9 sensing units arranged in 3 columns which are patterned on the PVDF film. Both layers are to be supported by a layer of Plexiglas. The sensor design was modelled to evaluate the performance of the sensor and its ability to measure forces and detect their locations. The simulation results showed a linear relationship between the force applied and the output voltage. The results also were able to demonstrate the sensor's ability to evaluate concentrated and point loads. The results from the experiments conducted on the fabricated sensor confirmed the numerical results; hence, proved the ability of the sensor.

2.4.3 Fused Deposition Modelling (FDM)

FDM is an additive manufacturing process which fabricates a 3D model directly from the computer-aided design (CAD) model by the integration of several systems and processes such as the CAD system, materials science, computer numerical control, and the extrusion process. In a brief description of the FDM process, a filament is drawn into the liquefier head where it is melted to a semi-liquid state to be extruded through a nozzle depositing beads to fill a layer on the platform in a temperature-controlled chamber. The platform moves in the z-direction depending on the assigned layer thickness while the computer-controlled head moves in the X-Y plane (Figure 2.14)[136-138]. FDM has gained popularity among fabrication methods due

to its low cost and efficiency. It has recently been utilised in the fabrication of piezoelectric pressure and force sensors.

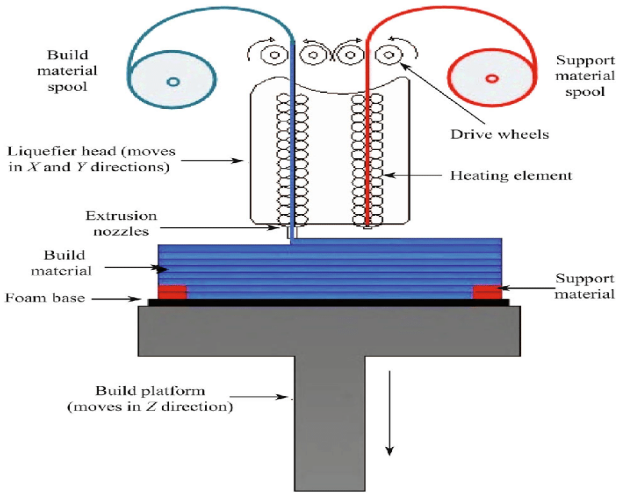

Figure 2.14: Illustration of the FDM process [138]

For instance, Kim, et al. [130] fabricated a piezoelectric pressure sensor by using the FDM process to 3D print a PVDF nanocomposite film. To find the optimum loading content, Various loading contents of BTO and multi-walled carbon nanotubes (MWCNTs) were experimented. The highest generated output voltage was obtained at a loading content of 18 wt% BTO and 0.4 wt% MWCNT. The same loading content recorded the highest piezoelectric coefficient $d31$ with a value of 0.13pC/N. The sensor showed mechanical and piezoelectric stability as no variation in the output voltage was noticed after 2000 periodic cycles and 3 days, respectively.

Lee and Tarbutton [129] examined how well a PVDF film, which was created using the electric poling assisted additive manufacturing process (EPAM), responded to sensing. The EPAM process involves adjusting a FDM printer to generate high voltage between the extruder's nozzle and the printing bed to align the filament's dipoles (Figure 2.15). The sensitivity of the PVDF film was tested for sensing and found to be 0.36nA/N. They also observed that PVDF treated with plasma exhibited 3-4 times more piezoelectricity than untreated PVDF.

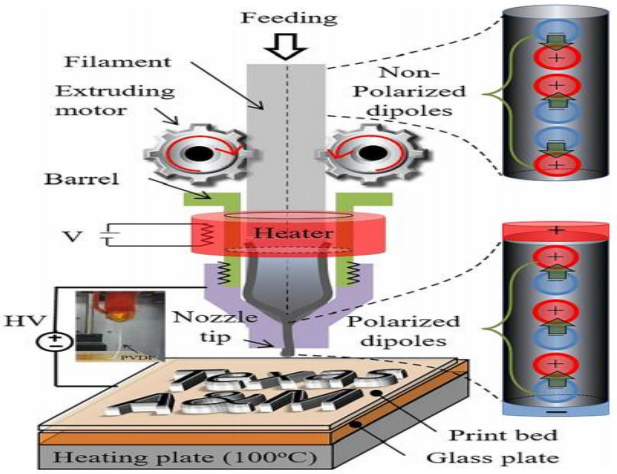

Figure 2.15: EPAM process [129]

Kim, et al. [139] evaluated the piezoelectric effect and the mechanical properties of a potential piezoelectric sensor from a PVDF composite 3D printed by the EPAM process. The PVDF was reinforced with several loading contents of BTO particles varying from 3-15 wt%. The experiments showed that a 15 wt% BTO reinforcement resulted in a piezoelectric coefficient of 0.101pc/N demonstrating a 1342% increase to the piezoelectric coefficient of the non-poled PVDF. The mechanical characterization tests showed an opposite trend as the content of BTO increased past 3 wt% BTO, the tensile and the fatigue strength of the composite decreased.

The potential reasons behind the reduction in tensile and fatigue strength with higher content of BTO could be due to the creation of defects and stress accumulation from agglomerates.

Tarbuttona, et al. [140] studied the phase transformations and the shock sensor ability of PVDF 3D printed by the EPAM process. The results showed that polymer after printing was 35% crystalline, and the crystalline phase consisted of 35% β phase crystals. Single and dual layers of PVDF were printed to evaluate their ability as shock sensors. The drop test results show that the single layer sensor recorded a higher charge coefficient of 0.66pC/N while the dual layer only recorded 0.23pC/N.

2.4.4 Stereolithography (SLA)

Stereolithography, also known as vat polymerization, is an additive manufacturing technique that uses a single or multiple UV laser beams to cure a liquid photopolymer resin in a layer by layer manner[141-143]. Briefly, the laser source is placed over a platform in a resin reservoir. The computer aided laser source projects laser beam in a controlled path over the platform to

cure resins by photopolymerization. After the first layer has been cured, the platform is lowered into the resin and another layer is cured on top of the first layer [144]. Once the curing process is over, the printed product is usually rinsed in a solvent to remove any present uncured resins[145].

As research and investigations on the SLA process progressed, other techniques were created by modifying the SLA process such as micro-stereolithography (μSL) and digital light processing (DLP). μSL utilises a lens to focus the laser beam in addition to using a smaller laser light spot which yields an improved resolution in the micrometre range [146, 147].
While DLP uses a digital projector coupled with an array of micro-mirrors to flash an image of the whole layer on the resin at once which reduces the exposure time (Figure 2.16) [148, 149].

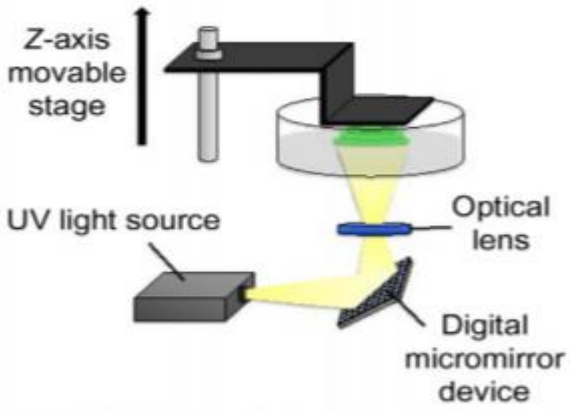

Figure 2.16: schematic representation of the DLP process [148]

The SLA technique was utilised to print several piezoelectric materials such as KNN, BT, and PZT [150-152]. For instance, Chen, et al. [151] printed complex structures from KNN-based piezoceramic green parts using the micro-stereolithography method (Figure 2.17). The printing process was followed by a two step thermal debinding and sintering processes to enhance the density of the printed structures. The printed structures exhibited piezoelectric properties with d_{33} = 170pC/N and ε_r= 2150 which is inferior to KNN ceramics fabricated using the traditional methods. The cause of the relative poor performance could be the voids' presence after the sintering process.

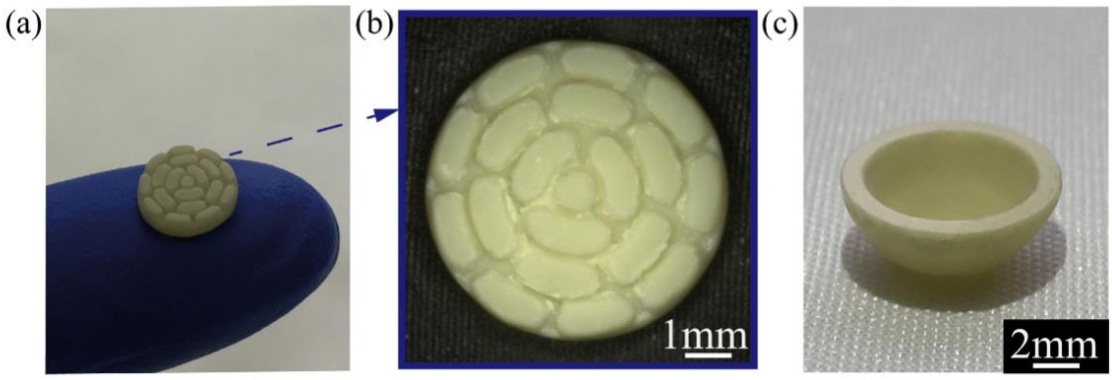

Figure 2.17: Images of complex structures printed using the µSL process. a) 2D segmented annular array for ultrasound transducer b) optical microscopy image of the annular array c) a hollow hemisphere [151]

Whereas Kim, et al. [131] employed the SLA technique to fabricate photopolymer resin (PR) based PVDF blends for pressure sensing applications. The direct mixing between PR and PVDF results in sediments which would result in poor piezoelectric performance; hence, DMF is used as a solvent to evenly disperse PVDF molecular chains to prevent their agglomeration. To obtain the optimum PVDF:DMF ratio and PVDF loading content in PR, several loading contents and ratios were experimented. The 1:10 ratio and 2%wt PVDF/PR showed the best piezoelectric properties with d_{31} = 0.014pC/N. The printed blend also reported a current of 0.18nA when a dynamic force of 80N was exerted.

While Zhou, et al. [132] 3D printed a stretchable piezoelectric nanogenerator using the DLP process. BT nanoparticles were mixed with photocurable resins, AUD and EAA, to form the printable ink. The optimal loading content of BT nanoparticles were 15%wt as higher content would result in blocking the UV light; therefore, the ink will not be cured. Under the optimal loading content, the printed nanogenerator recorded a maximum strain and a d_{33} of 434% and 0.78pC/N, respectively. The nanogenerator was experimented under dynamic forces ranging from 30-60N, and showed a sensitivity of 59.8mV/N which is similar to the commercial sensors used for motion monitoring.

2.4.5 Binder Jetting (BJ)

Binder Jetting is another additive manufacturing process used to print piezoelectric materials. Usually used to print ceramic and metallic materials, BJ can be simply described as the selective deposition of a binding liquid to join powdered materials[153]. To fabricate parts using the BJ process, the following steps need to be fulfilled[154, 155]. The spreading of a thin layer of powder on the build box, the area on the powder bed where the printing occurs, is considered to be the first step (Figure 2.18). The powdered layer is then levelled and loosely compacted by a counter-rotating roller. Then, the binding liquid is deposited on selected areas on the build box to form the first layer of the part. To dry and prepare the layer for the spreading of the upcoming layer, an electrical heater passes over the powder bed. After the binder has dried, the building platform is lowered by the thickness of one layer with the aid of the piston supporting the powder bed, and the whole process is repeated until the part is fabricated.

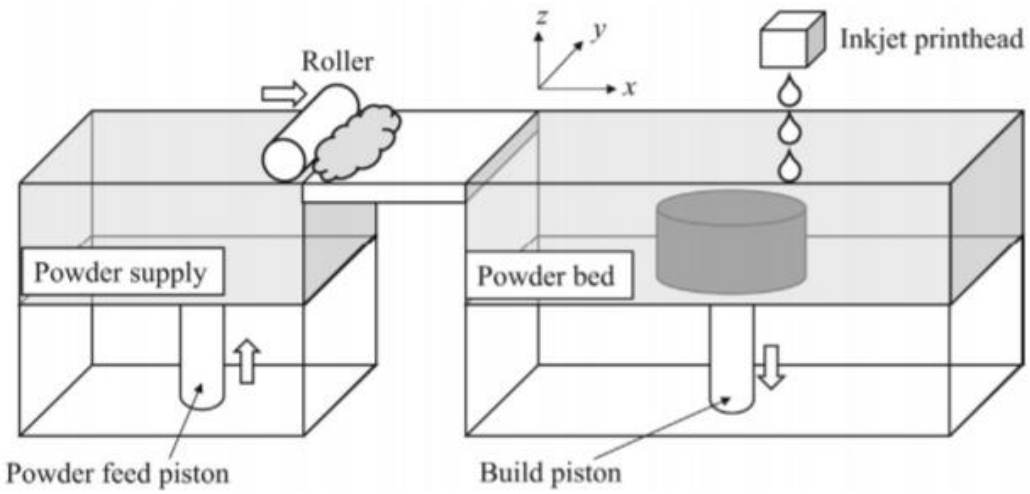

Figure 2.18: Schematic representation of the Binder Jetting process [155]

Due to the fragility of the fabricated green parts, post-processing steps are required to enhance their mechanical properties[156, 157]. The post-processing steps include powder removal, debinding, and sintering.

Despite being utilised in printing ceramics, the BJ was never used to fabricate piezoelectric sensors. Yet, it has been employed to fabricate and investigate the piezoelectric and dielectric properties of Barium Titanate. Where Gaytan, et al. [157] investigated the effect of the binder saturation and the sintering temperature on the density, dielectric properties, and piezoelectric performance of the BTO parts fabricated by the BJ process. It was found out that a binder saturation less that 60% would not provide the desired geometry. It was also reported that the

highest density, dielectric constant range at a frequency of 1kHz, and piezoelectric properties were obtained at a sintering temperature of 1400°C with 3.93g/cm^3, 600-725, and 74.1pC/N, respectively. The reason behind the better properties of specimens sintered at 1400°C could be their small grain size

2.4.6 Other Techniques

Apart from the mentioned techniques before, other methods have been used to fabricate piezoelectric pressure and force sensors such as radio frequency magnetron reactive sputtering system, thermal mechanical stretching, and facial solution casting.

For instance, Yang, et al. [119] manufactured a flexible piezoelectric pressure sensor for human motion monitoring by using facial solution casting method on the composite PDA@PVDF/BTO.
Due to the poor dispersion of BTO in PVDF, the surface of BTO was modified by polydopamine (PDA). Several weight percentages of PDA@BTO to PVDF were experimented to obtain the mass fraction with the best properties. The SEM images showed that using PDA to modify the surface resulted in absence of cracks or defects which are present in the PVDF/BTO composite. The results from testing the piezoelectric composite film with a linear motor showed that force and voltage were linear as expected. The bending test on the sensor demonstrated that increasing the bending angle resulted in an increase of the voltage produced as well as showing that the response time of the sensor was 61ms. The fatigue test done on the 21% PDA@BTO/PVDF sensor for 1000 cycles on 12N resulted in a 6.7% decrease in the voltage which indicates the excellent stability and durability of the sensor.
The optimum mass fraction was 17 wt% of PDA@BTO which obtained a peak voltage of 9.3V when an impact force of 12N was applied.

Whereas Ting, et al. [126] utilised the thermal stretching technique to design and fabricate a 3D piezoelectric force sensor from a one layer of thin PVDF film. The PVDF was heated and stretched to a stretch ratio (SR) of 6 before the poling process. 6 electrodes were deposited on the film to conduct the poling process. Horizontal-side polarization was applied to measure force changes in the X and Y-axis directions while thickness polarization was done to measure forces in the Z-axis direction. As expected, the sensitivity of the sensor along the Z-axis

direction was more than the other directions. To enhance the sensitivity in the X and Y directions, an interdigital electrode pattern was implemented. As a result, the piezoelectric coefficient $d33$ and the sensitivity of the sensor along the X and Y-axis directions increased to approximately equal their correspondent values in the Z-axis direction. .

While Curry, et al. [124] integrated thermal annealing to the thermal stretching process to design and fabricate a biodegradable force sensor utilizing the shear piezoelectricity of PLLA. Due to the poor piezoelectricity of PLLA, multiple layers will be fabricated to enhance the sensitivity of the sensor. The sensor consisted of only biodegradable material such as Molybdenum and Magnesium as electrodes and Poly(lactic acid) (PLA) was used to encapsulate the sensor. The sensor was mechanically modelled to find the relationship between the normal stress and the shear stress. It was found out that a PLLA film cut to 45 degrees, relative to the stretching direction, exhibits the maximum piezoelectricity in the normal stress directions. Experiments proved the theoretical deductions as only the sensors based on PLLA films cut relative to the stretching direction produced an output voltage when a force was applied. The sensor was placed in an incision below a mouse's diaphragm to detect the breathing pattern to show the potential applications of the sensor.

Akiyama, et al. [125] designed and fabricated a highly flexible pressure sensor by using the radio frequency magnetron reactive sputtering system to prepare oriented Aluminium Nitride (AlN) thin films on a flexible PET substrate. The piezoelectric response of the sensor was 0.7pC/N which is lower than the piezoelectric coefficient d_{33} (3-5 pC/N), this could be due to the low crystallinity of the piezoelectric film.

The capabilities of the sensor were evaluated by measuring the human pulse wave forms and comparing them to a commercial sphygmomanometer. At stress levels of 10kPa, the resolution of the pulse waves produced by the sensor were similar to the sphygmomanometer. The piezoelectric response of the sensor under the deflection mode was reported to be 30pc/N, and that the piezoelectric response of the sensor can be enhanced by decreasing the thickness and Young's Modulus of the substrate.

2.5 Research Gap

Despite the considerable amount of research conducted on PVDF, there is still a research gap in the exploration of its co-polymers. Existing literature has predominantly concentrated on PVDF, and less attention has been paid to its co-polymers. Furthermore, the high cost of PVDF has driven the need to identify cost-effective alternatives. Therefore, it is necessary to investigate alternative materials that could potentially substitute for PVDF in the development of piezoelectric devices.

The limited literature on PVDF copolymers, especially PVDF-HFP, restricts access to approaches for enhancing the piezoelectricity of this material. In particular, investigations on the effect of 3D printing parameters on the mechanical and piezoelectric properties of PVDF-HFP are yet to be carried out, creating another research gap that needs to be addressed. Addressing these gaps is crucial for PVDF-HFP samples to meet the necessary specifications if they are to be used as alternatives to PVDF.

In summary, although there is literature available on PVDF and its use in piezoelectric devices, alternative materials and methods to enhance their piezoelectric performance still need to be explored. These research gaps are detailed further in Chapters 3 and 4, where the research methodology and approach used to address them are explained.

3. Methodology for Fabrication and Characterizing the Properties of 3D-printed PVDF-HFP

This research project focuses on investigating the additive manufacturing (AM) of poly(vinylidene fluoride-co-hexafluoropropylene) (PVDF-HFP) and its composites using fused deposition modeling (FDM) for a potential use in force sensor applications. Despite the growing body of literature on AM techniques, there remains limited research on PVDF-HFP and its composites, particularly with respect to the effect of processing parameters on the properties of printed samples.

To justify the choice of PVDF-HFP and FDM as the material and fabrication method, a comparison with other potential polymers and fabrication methods is presented in this chapter. This will determine the most suitable options for producing samples with the desired properties for the force sensor application. Optimization of processing parameters will also be undertaken to enhance the piezoelectricity of the fabricated samples. The Design of Experiments (DOE) method will be utilized to aid in understanding the effects of the printing parameters and their interactions in addition to predicting the paramters that optimize the response.

In the subsequent chapter, techniques for enhancing piezoelectricity will be reviewed and selected based on their suitability for the application at hand. The information will provide justification for choosing the reinforcement technique in addition to the fillers chosen (Barium Titanate and Untreated Activated Carbon). The optimal mixture design of experiments (MDOE) was employed to analyse the effect of the fillers on the β-phase content of the polymer matrix. It was also utilized to predict the formulation with the highest β-phase content. To fabricate the samples to run the samples needed for MDOE, solution casting technique was used. This arose another point of investigation, an alternative solvent instead of the hazardous DMA and DMF must be found. The polar solvent DMSO was used and the viability of its employment was also investigated. The information obtained from these investigations will be used to print the composite. To evaluate the material for potential force sensor applications, the

printed samples undergone electromechanical tests to confirm their piezoelectricity and evaluate their force sensitivity.

Throughout Chapter 3 and Chapter 4, appropriate characterization techniques will be employed to analyze the structure, mechanical, and thermal properties of the samples, in order to gain a comprehensive understanding of their behavior and optimize their performance. Figure 3.1 depicts a flowchart of the processes to be followed in this investigation.

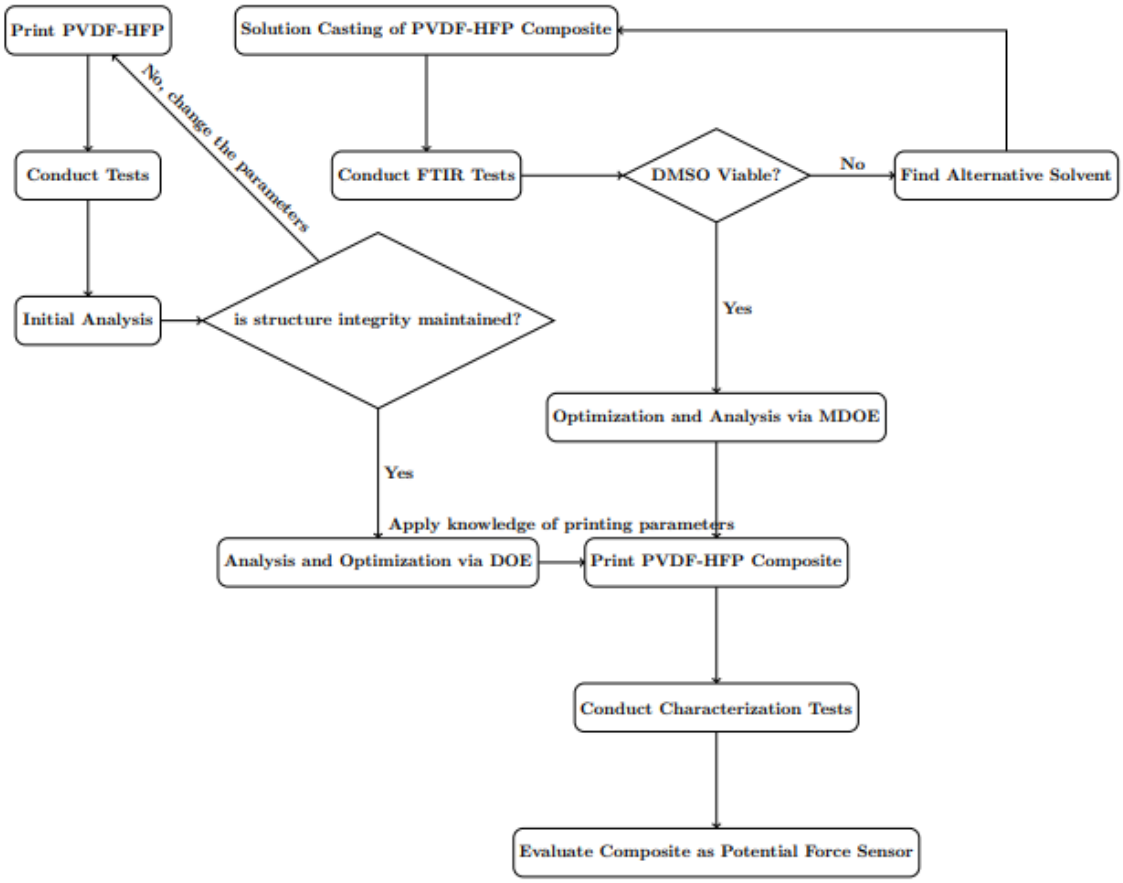

Figure 3.1: Methodology Flowchart

3.1 Piezoelectric polymer selection

The requirements that should be met to fabricate a functional piezoelectric force sensor are excellent piezoelectric and mechanical properties. Due to the brittle nature of piezoceramics and the relatively low piezoelectric properties, piezoelectric polymers and composites were utilised to fabricate piezoelectric force sensors. Since PVDF and its' copolymers dominate the remaining piezoelectric polymers by a huge margin when comparing the piezoelectric properties, the choice for the piezoelectric polymer can be narrowed down to PVDF and its'

copolymers.The superior piezoelectric properties were not the only reasons since PVDF provides excellent chemical strength, resistance to UV radiation, and high mechanical strength and toughness[158, 159].

Another point in PVDF and its' copolymers' favour is that it can be 3D printed by the FDM process due to being a thermoplastic polymer[160]. As the homopolymer have been overviewed earlier, the following section will contain an overview on the structure and piezoelectricity of the copolymers, followed by a comparison to justify the material selection.

3.1.1 Polyvinyldene Flouride (Hexaflouropropylene) (PVDF-HFP)

The structural difference between PVDF and PVDF-HFP rises from the incorporation of HFP to the original structure as shown in Figure 3.2 [161]. This simple change results in reducing the crystallinity of the polymer increasing its flexibility [162, 163]. The incorporation of HFP also results in a reduction in the solubility of PVDF due to the presence of the Flourine atoms[164, 165].

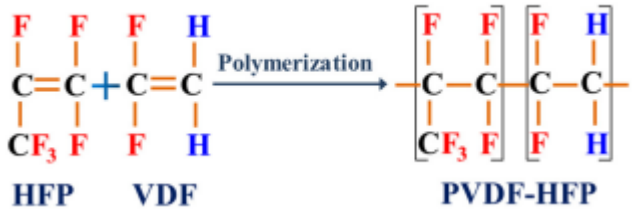

Figure 3.2 : Polymerization of PVDF-HFP [161]

Regarding the piezoelectricity, PVDF-HFP exhibits piezoelectricity in the same mechanism PVDF uses to exhibit piezoelectricity. For instance, it was mentioned by He, et al. [166] that the PVDF-HFP exhibits piezoelectricity, and that it depends on the orientation of the polymer chains just like the homopolymer (PVDF). In the same paper, the β-phase activity of stretched and annealed samples of PVDF-HFP were investigated. Despite no poling was done to either samples, the stretched samples recorded a $d33$ of 12.6 pC/N while the annealed samples registered a $d33$ of 9.5pC/N. It was also reported in another paper by by Huan, et al. [167] that the $d33$ of a stretched and poled PVDF-HFP film is 24pC/N which is a very close value to what the homopolymer reports in literature.

3.1.2 Polyvinyldene Flouride Triflouroethylene (PVDF-TrFE)

Following the similar synthesis process, PVDF-TrFE is synthesised using the polymerization of the VDF monomer with the TRFE monomer Figure 3.3 [161]. The incorporation of the TrFE monomer results in enhancing the crystallinity and improving the orientation of good growth crystallinity. However, a molar concentration of 11% or higher of TrFE induces defects produced by the fluorine atoms restricting the formation of the α-phase below the Curie temperature[168].

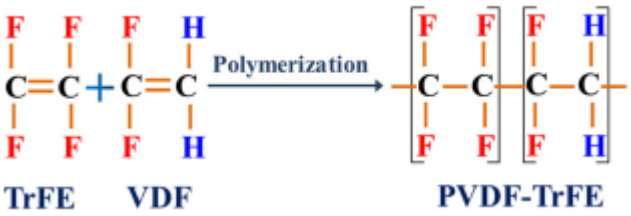

Figure 3.3 : Polymerization of PVDF-TrFE [161]

Regarding piezoelectricity, PVDF-TrFE is slightly different since the employment of the TRFE monomer results in a smooth formation of the β-phase meaning that mechanical stretching and the other phase transformation techniques are not required [168, 169]. Since the TrFE monomer content dictates the crystallinity of the polymer, it can also affect the piezoelectricity of the polymer greatly. For instance, Omote, et al. [170] reported a $d33$ coefficient of 38pC/N for single crystal films of PVDF-TrFE (75-25 mol%). In another work by Hu, et al. [171], it has been reported that a PVDF-TrFE (80-20 mol%) film poled using an in-situ polarization technique recorded a $d33$ coefficient of 28pC/N.

3.1.3 Comparison between candidate polymers

Due to the presence of three suitable candidates for the piezoelectric polymer position, a comparison must be done to choose the appropriate polymer. Owing to their shared structural similarities, these polymers exhibit analogous chemical characteristics, including inertness, hydrophobicity, and thermal stability, alongside comparable mechanical properties such as Young's Modulus [172-174]. Consequently, conducting further comparisons of either mechanical or chemical properties are deemed insignificant. Several factors will be deciding the suitable piezoelectric polymer.

Starting with the most important one, the piezoelectric performance of the polymers. Out of the other polymers, PVDF-TrFE recorded the highest piezoelectric performance according to several works in literature with an average $d33$ value ranging from 30 to 38 pC/N followed by the other polymers with a range of 20-30 pC/N. Another point in PVDF-TrFE's favour was that its' structure allows the formation of the β-phase smoothly without the need for any transformation techniques. The previous information are in PVDF-TrFE's favour; however, they are not enough to eliminate any of the other polymers since they recorded similar piezoelectric performances despite PVDF-TrFE's slightly higher results. The second factor chosen was the cost. PVDF-TrFE was found out to be tenfold the price of the other polymers which were approximately of the same value [175, 176]. PVDF-TrFE is to be eliminated due to its very high cost which is not justified by its piezoelectric performance since the other candidates recorded similar performances.

With PVDF and PVDF-HFP remaining as the polymer candidates, a comparison between their FDM printability can take place due to the fact that they are thermoplastic polymers in addition to FDM being one of the promising fabrication methods to be chosen for the study. The comparison was done in a study conducted by Mullaveettil, et al. [177] where filaments of PVDF and PVDF-HFP were 3D printed to investigate their mechanical properties. Another aim of the study was to provide a comprehensive guide for the 3D printing process tailored to PVDF-based materials. It was noticed that PVDF-HFP samples lack warpage and show adequate adhesion unlike the homopolymer due to its higher degree of crystallinity. Regarding the mechanical properties, it was reported that the homopolymer registered the highest tensile and compressive modulus values for 100% infill density with 1800MPa and 1100MPa, respectively. On the other hand, the copolymer only registered 60% of the tensile and compressive modulus values reported by the homopolymer. This could also be explained by the higher degree of crystallinity of the homopolymer. For the flexural properties, the copolymer registered the best properties due to its lower degree of crystallinity.

Despite FDM not chosen as the fabrication method yet, it can still be used to settle the debate between the homopolymer and PVDF-HFP. Since warping can cause the total loss of samples , it would be a safer bet to proceed with PVDF-HFP. This choice was also reinforced with other reasons like its similar piezoelectric performance for a lower cost in comparison to PVDF.. Another reason was that PVDF-HFP has not received much attention and this study could spark the interest of other researchers looking for a PVDF alternative.

3.2 Comparison between fabrication methods

Due to the presence of several potential fabrication methods to manufacture a force sensor, a comparison between the possible methods and the selection of the fabrication technique will be done in this section. A summary of the advantages and drawbacks for each technique can be found in Table 3.1.

Before addressing the additive manufacturing methods, the benefits and limitations of the photolithography and electrospinning techniques are to be compared. For instance, the photolithography process creates extremely small patterns and creates precise control over the shape and size of objects created[178]. On the other hand, it is an expensive process which requires extremely clean conditions. The procedure also lacks the ability to cut in the horizontal direction in addition to its low effectivity when fabricating parts without a flat surface[178, 179]. As the disadvantages outweigh the advantages of the process, it will be excluded as a possible fabrication method.

The electrospinning process offers a simple low-cost process which can control the fibre morphology[180]. In addition, electrospun piezoelectric fibres do not require poling due to the high voltage application causing the alignment of the dipoles [133, 181]. On the contrary, the electrospinning process usually operates in hazardous conditions such as high voltage and the usage of toxic volatile solvents[182, 183]. In addition, the characteristics of electrospun fibres depend on a lot of variables that need to be monitored and controlled such as but not limited to the solution concentration, feed rate, tip-to-collector distance, and applied voltage[184]. Despite the benefits of using the electrospinning process, the environmental impacts of the hazardous working conditions rule out the electrospinning technique as a possible fabrication method.

After ruling out the photolithography and electrospinning processes, the additive manufacturing processes remain as potential fabrication methods. The additive manufacturing processes that have been utilised to print piezoelectric materials are FDM, SLA, and BJ.

Starting with Binder Jetting, the BJ process offers several advantages when compared to other additive manufacturing processes. For instance, BJ can be employed for virtually any powdered feedstock[185, 186]. In addition, the building rate for BJ is higher as only the binding liquid is being printed[153]. Another advantage is that parts fabricated by BJ do not experience thermal

stresses and distortions due to the lack of any significant heating or melting processes in the BJ system[187]. On the other hand, the post-processing plans haven't been developed for majority of the materials. In addition, a relatively higher surface roughness and lower resolution are obtained using BJ when compared to other AM processes[153]. Finally, there is limited work on BJ of polymers due to the rarity of polymer fabrication from powders; hence, limited formulations are available[186]. As the proposed material for the force sensor fabrication is polymer based, the BJ process will be excluded due to its limited work on polymers.

After all techniques have been eliminated, FDM and SLA remain. SLA offers a simple operation method with higher resolution, surface precision, and efficiency when compared to FDM and other AM processes while FDM provides a low-cost user friendly high speed fabrication method[147, 188].

However, SLA presents a significant challenge to our study which is its' compatibility with PVDF-HFP since it is the chosen material for this study. As known, PVDF-HFP is a thermoplastic polymer and is not a photopolymer which makes it incompatible with SLA. There have been experiments to reinforce the photopolymer resin with PVDF by Kim, et al. [131]; however, their studies showed that a maximum of 2%wt of PVDF was incorporated and the fabricated sample yielded a very low piezoelectricity when compared to the pristine polymer. Other hurdles also introduced by SLA are that it is not suitable for multi-material mixing, the presence of chemical wastage after the process, and the high cost of equipment.

On the other hand, FDM demonstrates excellent compatibility with PVDF-HFP while the downside for using FDM is that it produces parts with weak mechanical properties [142, 147, 188]. While SLA provides slight improvement in resolution and mechanical properties, these advantages are outweighed by its incompatibility with PVDF-HFP, the cost difference, and the environmental impact caused by the chemical wastage. Considering practicality, cost effectiveness, and potential challenges, FDM emerges as the preferred choice to be employed to fabricate the force sensor.

Table 3.1 : comparison between the fabrication methods

Fabrication Method	Benefits	Drawbacks
Electrospinning	Simple and low-cost equipment Fibre Morphology can be controlled Fabricated piezoelectric parts do not require poling	Toxic solvents Many variables need to be controlled for the process
Photolithography	Creation of extremely small patterns Precise control over the shape and size of objects created	Expensive process Procedure can only cut in the vertical direction High efficiency when fabricating a flat shape only. Requires extremely clean operating conditions
FDM	Low Cost User friendly High speed	Weak mechanical properties
SLA	Simple operation method High resolution High surface precision High efficiency	Not suitable for multi-material mixing The chemical wastage after the process Expensive equipment

		Slow printing
BJ	High building rates Fabricated parts do not experience thermal stress	High surface roughness Low resolution Very limited work on polymers

3.3 Fabrication and Testing

3.3.1 Extrusion and Printing

Resin pellets of PVDF-HFP (Sigma Aldrich) were acquired and subsequently converted into filament for 3D printing purposes. Filament fabrication was achieved using an in-house extruding system consisting of a single screw extruder (Filastruder) and a filament winder (Filawinder) (Figure 3.4). The pellets were fed to the Filastruder preheated to 180°C and had an exit nozzle diameter of 1.75mm. As the filament was extruded, it underwent air-cooling and passed through the infrared dynamic positioning sensor. The sensor utilized a laser emitting specific frequencies to monitor the filament's color. The winding motor speed was adjusted based on the changes in frequency as the filament moved. After the filament was spooled, several diameter measurements from different points across the filament were taken concluding that the resulting pure PVDF filament was cylindrical and had a uniform diameter of 1.75±0.15 mm. The Fused Deposition Modeling process was carried out using a low cost Creality Ender-3 Max 3D printer, as illustrated in Figure 3.5. The printer is equipped with a 0.4mm nozzle and features a Carborundum Glass printing bed. To enhance the initial layer adhesion, a thin coat of Elmer's disappearing purple glue stick was applied before commencing any print.

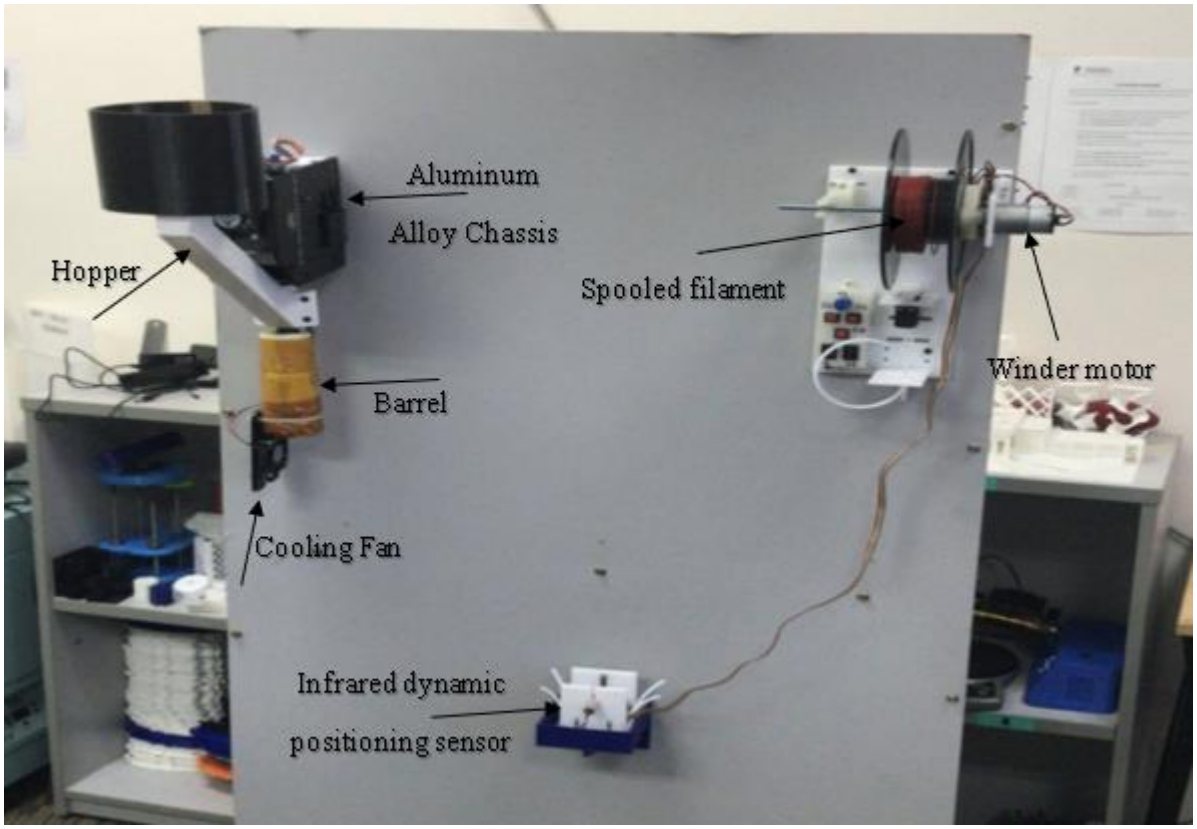

Figure 3.4 : Filament extruding Setup

Figure 3.5 : Creality Ender-3 Max 3D printer

The printing parameters were a topic that required further thought due to the fact that they impact the mechanical properties of the samples as seen in the works by Mullaveettil, et al.

[160] and Porter, et al. [189]. Moreover, as reported by Momenzadeh [190], certain adjustments to printing parameters, such as reducing the nozzle diameter or increasing the infill density, have been found to enhance the β-phase content of the printed samples, thereby improving their piezoelectric behavior. This increase in β-phase content is attributed to the additional residual stress within the polymer. Residual stress in a printed part arises from various factors, with the primary one being the multiple heating and cooling cycles involved in the 3D printing process [191, 192]. While increased residual stress is advantageous for enhancing the β-phase content in printed samples, it has adverse effects on the structural integrity of the parts. Higher residual stress levels can lead to issues like distortion, interlayer cracking, and part delamination, thereby hindering the structural integrity of the printed components [193].Therefore, the printing parameters should be tailored to optimize the β-phase content while maintaining an adequate structural integrity. Further information regarding the approach chosen to optimize the β-phase will be discussed in the upcoming subsection.

To determine the appropriate printing parameters, Table 3.2 was created to consolidate the processing parameters that exhibited variations when printing PVDF, PVDF-HFP, and their composites in existing literature. It is worth noting that PVDF-HFP was 3D printed in few works so PVDF was used an additional guide due to the similar chemical structure Several parameters, such as infill density, nozzle diameter, and line width, consistently fell within a similar range of values, and therefore, these settings were maintained, as outlined in Table 3.3.

While Table 3.2 revealed discrepancies in bed temperature values across different studies, with the majority reporting higher temperatures ranging from 90-100°C, it's noteworthy that a couple of works by the same author reported much lower temperatures, as low as 23°C. Our preliminary tests were conducted with the objective of identifying a suitable range for testing the effect of bed temperature on the printing process. However, these tests revealed that reliable adhesion of the printed samples was consistently achieved only at a bed temperature of 110°C. Given the practical limitations of the 3D printer available for this study, which can only heat the bed to a maximum of 110°C, this temperature was selected for maintaining consistent material adhesion throughout the study.

Table 3.2 demonstrates that researchers commonly printed samples within an extrusion temperature range of 230-260°C. While this temperature range may appear high for polymers, PVDF boasts a wide melt processing window (180-265°C) [160]. Nevertheless, it has been noted by Kim, et al. [194] that attempting to print below 230°C leads to issues with bed

adhesion. Researchers commonly avoided temperatures higher than 260°C to prevent approaching the upper limit of the melt processing window, which ends at 265°C. Instead, they often opted for temperatures exceeding 230°C because higher extrusion temperatures are recognized for their ability to reduce viscosity, thereby facilitating smoother melt flow with a lower pressure drop. In addition, it enhances the fusion of adjacent layers improving the mechanical strength of the printed sample [195-197]. Furthermore, since the primary objective of this study is to enhance the β-phase content, it's essential to consider that higher extrusion temperatures lead to increased residual stress, resulting in a rise in the β-phase content. However, as the structural integrity of the samples is equally crucial alongside β-phase content, it is imperative to investigate the effects of varying temperatures within the range of 230-250°C. This comprehensive analysis ensures the attainment of structural integrity and optimal piezoelectric properties for the sensor. Notably, the upper limit of 250°C was chosen to align with the maximum temperature capability of the 3D printer.

For the printing speed, the range used in literature was 10-30mm/s. It is known that using a lower printing speed usually results in a more precise prints as higher speeds of dynamic systems give rise to jerky motion affecting the stability of the nozzle[195]. On the other hand, using lower speeds increases the time needed to print samples. It is also worth noting that using lower speeds will result in a longer cooling-heating cycles increasing the residual stress improving the β-phase content. Therefore, investigating the effect of varying the printing speed in the range 10-30 mm/s should be done to understand the relation between the printing speed and the β-phase content.

For the layer thickness, it is observed in Table 3.2 that the previous works have printed PVDF or its copolymers using layer thicknesses varying from 0.1-0.3mm. Using a thicker layer can be done to reduce the printing time. However, the shorter printing cycles come at the cost of a worse surface finish. The aforementioned information indicate the using thinner layers would improve the printing quality while increasing the printing time. It must also be taken into consideration that using thinner layers would mean more layers to print resulting in more cooling-heating cycles that would increase the residual stress improving the β-phase content.

Hence, layer thickness values in the range 0.1-0.3mm should be investigated to confirm the hypothesis regarding the relation between the layer thickness and the β-phase content.in addition to obtain the layer thickness that maximises the β-phase content while maintaining the structural integrity of the sample. The remaining printing parameters were kept constant and

the values were just as reported in previous works. Table 3.3 presents the remaining printing parameters used in printing the samples. Further details regarding how the experiments were going to be conducted and which characterization techniques took place can be found in the upcoming sections.

Table 3.2 : summary of processing parameters in literature

Material	Extrusion temperature/C°	Bed temperature/C°	Printing speed	Layer thickness/mm	Reference
PVDF	250	23	10mm/s	0.3	[194]
PVDF	220-240	NA	NA	0.1-0.15	[198]
PVDF	230	100	200mm/min	NA	[199]
PVDF/MWCNT	230	23	10mm/s	NA	[200]
PVDF	230	90	20mm/s	NA	[160]
PVDF-HFP	230	90	20mm/s	NA	[160]
PVDF-HFP	250-260	100	10-30mm/s	NA	[201]
PVDF-HFP/Li-KNN	260	NA	20mm/s	NA	[202]

Table 3.3 : List of printing parameters used to fabricate the samples

Printing Parameters	Incorporated Value
Layer Thickness	0.1-0.3mm
Line width	0.4mm
Wall thickness	0.8mm

Infill Density	100%
Infill Pattern	Lines
Printing Temperature	230-250°C
Bed Temperature	110°C
Printing Speed	10-30mm/s
Nozzle Diameter	0.4mm

3.3.2 Design of Experiment

After deciding the printing parameters to be investigated, a novel approach – Design of Experiments – has been employed to understand the effect of the printing parameters and the β-phase content in the printed samples. Conventionally, researchers would investigate different combinations for several factors and deduce the optimized from the combinations they experimented. On the other hand, the Design of Experiments (DOE) is a structured method of experimentation that systematically evaluates the impact of changes in certain factors on the response of a process. By controlling and manipulating one or more factors, DOE enables researchers to isolate each factor's effect and its relationship with the response, optimizing the process and enhancing overall performance [203]. Different types of DOE approaches are available, including full factorial designs, fractional factorial designs, and response surface methods, each with unique benefits and limitations. The choice of method will depend on the specific goals and constraints of the experiment.

One statistical method, the full factorial design, tests all possible combinations of factor levels, comprehensively identifying main effects and interactions between a set of factors on a response variable. This approach determines the most critical factors and their optimal settings while detecting interactions that could impact the response. However, it can be time-consuming and resource-intensive, especially when dealing with many factors and levels [204].

However, the full factorial design can be time-consuming and resource-intensive, especially if there are many factors and levels. In such cases, fractional factorial designs can be used. The fractional factorial design selects a subset of all possible combinations of input variables,

reducing the number of experimental runs required while still providing sufficient information to estimate the effects of the input variables on the response. However, fractional factorial designs have limited resolution, making it difficult to distinguish between all possible interactions between variables, leading to confounding and potentially missing important effects [204, 205].

Response surface design is an experimental method that refines models by analyzing and optimizing a system's response after identifying critical factors using screening or factorial designs. This technique is useful in situations where the response is expected to have a curved shape, allowing for modeling the response's curvature using quadratic terms. Therefore, response surface designs are valuable in optimizing responses where there is curvature [204].

After a brief overview of different options for Design of Experiments (DOE), the approach chosen is as follows: a full factorial design will be used to investigate the effects of three factors (temperature, printing speed, and layer thickness) on the β-phase content of 3D printed samples while maintaining structural integrity. The decision to focus on these specific parameters was grounded in the observation that distinct values have been applied for each parameter in the existing literature. In addition, due to the constraints in time and available resources, expanding the DOE beyond three parameters was not feasible. This decision is driven by the fact that such expansion would result in a significantly higher number of samples required for printing. Minitab 21 will be used to conduct the full factorial design, where each factor will be tested at two levels only. This choice was made to minimize the number of experiments, save time, and reduce costs. The combinations to be tested will be listed in Table 3.4, and each combination will be replicated three times to enhance the reliability of the process and the accuracy of the model generated by the software. The β-phase content will be used as the response variable. Details about quantifying the response variable will be discussed in subsequent sections.

After the test results have been analyzed, the model generated by the software will be used to predict the values at the center points of each factor. The predicted values will then be compared with ten samples fabricated using the same combination. If the predicted values match the experimental values within an acceptable confidence interval, the linearity of the model will be confirmed. If the values do not match, the presence of curvature will be suspected, and further refinement of the model will be required using response surface design. The center points were chosen because the curvature trend usually occurs in the center.

Finally, the optimization process will take place after the model has been confirmed. The software will predict the parameters that optimize the β-phase content. Further characterizations will be performed on samples printed using the optimized parameters.

Table 3.4 : DOE generated list of samples to be fabricated

Sample Number	Printing Temperature/°C	Printing Speed/(mm/s)	Layer thickness/mm
1	250	30	0.2
2	250	10	0.2
3	250	10	0.1
4	250	30	0.1
5	230	30	0.2
6	230	10	0.2
7	230	30	0.1
8	230	10	0.1

3.3.3 Characterization techniques

Dynamic Mechanical Analysis

Dynamic Mechanical Analysis (DMA) is a technique that studies the mechanical properties of materials when subjected to cyclic stresses or strains. This technique involves applying small-amplitude oscillating force or deformation to a material and measuring its resulting response as a function of time, temperature, or frequency. DMA is commonly used to characterize materials such as polymers, composites, and biomaterials due to its ability to study stiffness, elasticity, damping, and viscoelastic behavior, as well as thermal and mechanical properties such as glass transition temperature and melting temperature [206].

In this study, DMA was used to investigate the effect of the printing parameters on the mechanical properties of the fabricated samples. Dynamic mechanical analysis (DMA) experiments were conducted using the PerkinElmer DMA8000 instrument in tension mode at a frequency of 20 Hz and a heating rate of 5°C/min over a temperature range of 30 to 150°C. The fabricated samples were rectangular with dimensions of 8x40 mm^2 and a thickness of 0.6 mm, as shown in Figure 3.6.

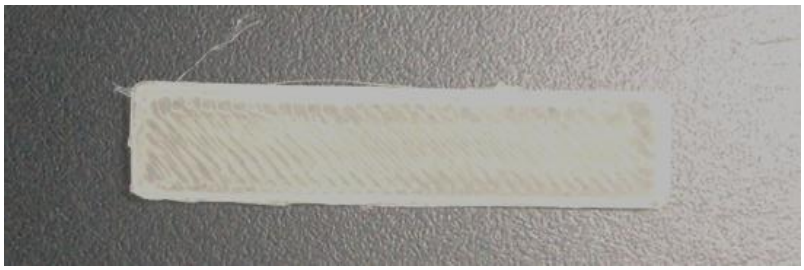

Figure 3.6 : DMA fabricated sample

Fourier Transform Infrared Spectroscopy (FTIR)

Fourier Transform Infrared Spectroscopy (FTIR) analysis is a common method for studying the chemical composition and structure of polymers. This instrument uses infrared radiation to interact with the chemical bonds in the sample, causing absorption at specific wavelengths. The resulting spectrum is recorded by the detector and displayed as a plot of absorbance vs. wavenumber (or frequency). In this study, the vibrational spectra of all samples were obtained using a PerkinElmer FTIR spectrometer with wavelengths between 600 and 1400 cm-1 and a resolution of 2 cm-1. The data from the scans were used to determine the β-phase content in films using the Beer-Lambert Law[60]. The samples fabricated for testing had a diameter of 20 mm and a thickness of 0.6 mm.

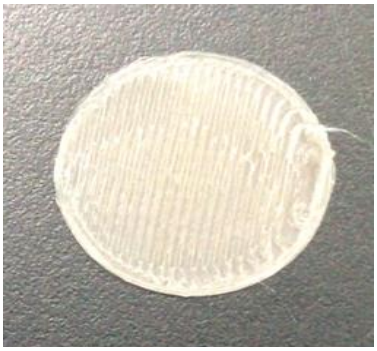

Figure 3.7 : FTIR Fabricated sample

Field Emission Surface Electron Microscopy (FESEM)

The printing surface quality and the presence of pores between the layers were characterized using Field Emission Scanning Electron Microscopy (FESEM). FESEM focuses an electron beam over the sample surface, producing various signals, including secondary electrons, backscattered electrons, and characteristic X-rays. These signals can be detected and used to generate an image of the sample surface [207]. FESEM FEI Quanta 400F was used to investigate the morphology of the samples where it was set with the following parameters: voltage = 20kV, spot size = 3.5, and working distance = 9.1mm for a secondary electron detector operating in a high vacuum mode for several magnifications.

Differential Scanning Calorimetry (DSC)

Differential Scanning Calorimetry (DSC) analysis was conducted on extruded filaments and 3D printed samples to investigate the effect of the 3D printing process on thermal properties such as melting point, crystallinity, and possible phase changes. DSC works by measuring the difference in heat flow between a sample and a reference material as they undergo controlled heating or cooling. As the temperature changes, the sample undergoes phase transitions such as melting, crystallization, glass transition, and chemical reactions, which are accompanied by the absorption or release of heat. These changes are detected by the DSC instrument as a change in heat flow [208]. The DSC analysis was performed by the DSC Q2000 TA instrument in a nitrogen atmosphere from room temperature to 200°C with a heating rate of 5°C/min.

Thermogravimetric Analysis (TGA)

Thermogravimetric analysis was performed by TGA DSC 1 Mettler Toledo instrument to investigate the thermal stability of the samples. The process involved subjecting the samples to heat, where a 10°C/min ramp was chosen to raise the temperature from room temperature to 800°C in a nitrogen atmosphere.

3.4 Results and Discussion

3.4.1 Pre-DOE analysis

After the fabrication and testing of the samples, an initial analysis was conducted to verify if there were any significant deviations between the results. The primary goal of this analysis was

to determine if a design of experiments (DOE) was necessary. Additionally, the initial analysis aimed to identify potential trends that could be confirmed by the software and help in selecting an appropriate DOE design to avoid wasting time and resources.

The FTIR spectra of the 3 fabricated samples for Sample 4 is displayed in Figure 3.8, within the range of 650-1400 cm-1. The data obtained from FTIR was used to examine the PVDF polymorphism, where the peaks observed at 840, 880, and 1279 cm-1 were identified as the β-phase. To determine the quantity of β-phase present in the samples, the fraction of β-phase was calculated using Equation 3.1, which utilizes the intensities of absorption bands at 763 cm-1 (α-phase) and 840 cm-1 (β-phase), denoted as Aα and Aβ respectively.

$$F(\beta) = \frac{A_\beta}{A_\beta + 1.26A_\alpha} \tag{3.1}$$

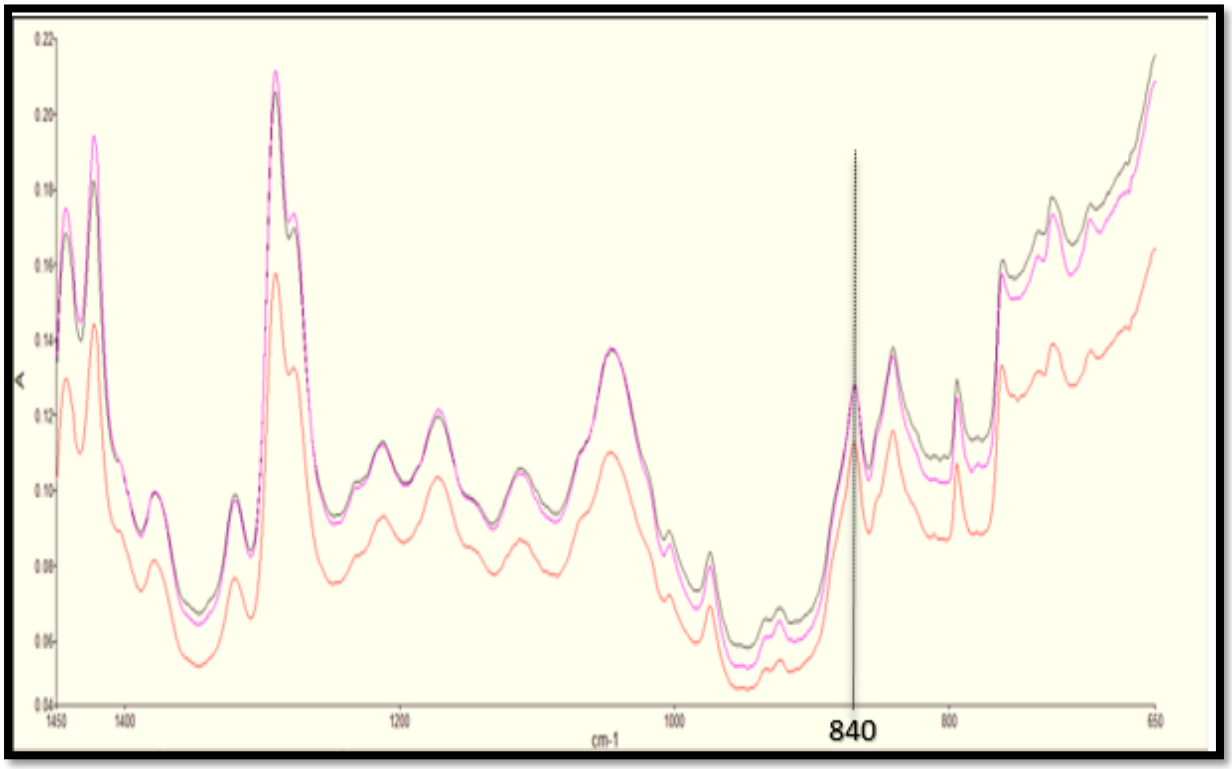

Figure 3.8 : FTIR spectroscopy of Sample 4

The value of F(β) obtained through Equation 1 represents the relative amount of β-phase to α-phase in the samples, but does not provide any information on the other phases of the printed sample such as γ, δ, ε phases.

Despite not providing information on the remaining phases, the fraction of β-phase was still chosen as the metric to be used when comparing the printed specimens. The average $F(\beta)$

values for each printed sample listed in Table 3.5 revealed a slight deviation between all samples, with sample 3 recording the highest β-phase content at 43.58%, and sample 7 recording the lowest value at 37.80%. The reported values correspond to the values reported in previous studies such as the work by Kim, et al. [209] where the printed homopolymer reported an average $F(\beta)$ of 42.87%.

Notably, the samples printed at higher extrusion temperatures showed higher β-phase content values than those printed at lower temperatures. A similar trend was observed for thinner layer thicknesses and slower printing speeds. These trends are consistent with the initial hypotheses, suggesting that higher printing temperatures, lower printing speeds, and layer thicknesses lead to higher β-phase content values. However, the accuracy of these hypotheses will need to be confirmed by the DOE analysis.

Before drawing conclusions from the initial analysis, it is important to note that all samples were printed smoothly without exhibiting warping or any visible defects, confirming the viability of the parameters and the preservation of the structural integrity.

Based on the initial analysis, it was observed that the β-phase content values varied for the samples, suggesting a need for a DOE analysis to gain a better understanding of the factors that affect the β-phase content and to optimize the printing parameters.

Table 3.5 : Average β-phase content for fabricated samples

Sample Number	F(B) / %
Sample 1	40.013
Sample 2	39.995
Sample 3	43.582
Sample 4	41.505
Sample 5	38.484
Sample 6	38.854
Sample 7	37.799
Sample 8	40.862

3.4.2 DOE Analysis

After β-phase content was chosen as the sole response to be studied, the software generated a model fitting the obtained responses using the regression fitting technique. The model used to predict the β-phase content in terms of printing parameters is postulated In Equation 3.2.

$$F(B) = -73.7 + 0.5018A + 2.54B + 675C - 0.01159AB - 2.945AC - 19.67BC + 0.0861ABC \quad (3.2)$$

Where A,B, and C represent the printing temperature, printing speed, and layer thickness, respectively.

With an R-squared value of 89.92% and an adjusted R-square value of 85.51%, the model can be deemed adequate. However, the model can not be used for analysis immediately due to the fact that the trend might have an unaccounted curvature and will need refinement. To confirm that a refinement to the model was unnecessary, the centre points test was applied. As seen in Figure 3.9, the model predicted a β-phase content value of 40.02% while the average β-phase content for the 10 fabricated samples was 40.13% which is within the 95% confidence interval specified by the software. After verifying that the model requires no refinement process, further analysis can be performed.

Settings

Variable	Setting
Temperature	240
Speed	20
Thickness	0.15

Prediction

Fit	SE Fit	95% CI	95% PI
40.0185	0.140772	(39.7201, 40.3170)	(38.5264, 41.5107)

Figure 3.9 : Prediction for the centre point sample

The software was used to conduct an analysis of variance (ANOVA) to examine the statistical significance and relevance of the model. ANOVA allowed for the assessment of the effects of individual factors and the interplay of factors on the response, with the ANOVA results presented in Table 3.6.

Table 3.6 : Analysis of Variance Table

Analysis of Variance					
Source	DF	Adj SS	Adj MS	F-Value	P-Value
Model	7	67.9016	9.7002	20.4	0
Linear	3	48.0648	16.0216	33.69	0
A	1	18.0054	18.0054	37.86	0
B	1	21.2006	21.2006	44.58	0
C	1	8.8588	8.8588	18.63	0.001
2-Way Interactions	3	15.3867	5.1289	10.78	0
AB	1	0.4259	0.4259	0.9	0.358
AC	1	8.9737	8.9737	18.87	0.001
BC	1	5.987	5.987	12.59	0.003
3-Way Interactions	1	4.4501	4.4501	9.36	0.007
ABC	1	4.4501	4.4501	9.36	0.007
Error	16	7.6096	0.4756		
Total	23	75.5113			

The Fischer value, obtained by dividing two mean squares, was employed to evaluate the statistical significance of the model, representing the ratio of explained variance to unexplained variance. The β-phase content response model F-values of 20.40 indicated that the regression model accounted for a majority of the variation in the response. The related p-value was used to determine the level of statistical significance, with values greater than 0.05 considered to indicate a non-significant model. However, as the recorded p-values were less than 0.0001, the regression equation demonstrated a strong correlation with the response. Furthermore, the linear factors and all factors' interactions apart from the (Temperature*Speed) interaction were considered significant due to their p-values, which recorded a value less than 0.05.

3.4.3 The effect of printing parameters on β-phase content

After confirming the model using center points and verifying the significance of the model and factors using the ANOVA table, a closer examination of how the factors affect the β-phase content is necessary.

While the factors recorded a p-value less than 0.05, indicating their impact on the β-phase content, the ANOVA table doesn't specify the nature of the impact, whether it is negative or positive. To understand the effect of each printing parameter, the sign coefficient in the response model should be observed. A negative sign indicates a negative impact, while a positive sign indicates the opposite.

Using the available information, it can be deduced that an increase in temperature results in an increase in the β-phase content, whereas an increase in printing speed or layer thickness negatively impacts the β-phase content values. In addition to the sign coefficients, factorial plots were used to study the effects of the factors and their interactions. Figure 3.10 shows that the factors didn't follow a horizontal line, which confirms their significance. The factorial plots also confirmed the deductions from the sign coefficients, as higher temperatures, lower printing speeds, and layer thicknesses recorded higher β-phase content values.

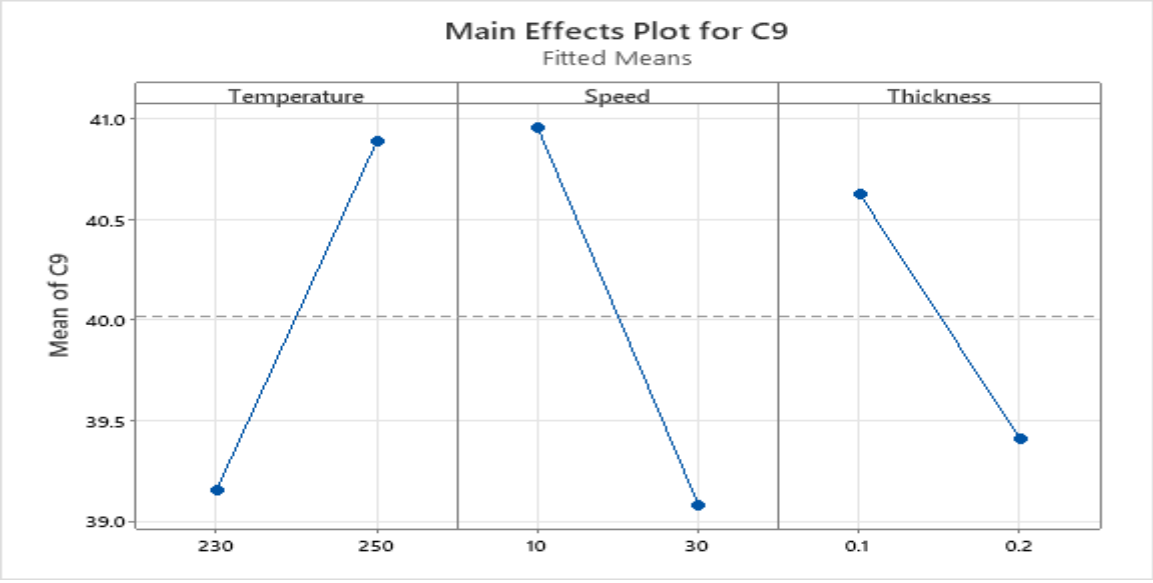

Figure 3.10 : factorial plots for the printing parameters

These deductions match the initial analysis results and confirm the hypotheses regarding residual stress. In addition to the factorial plots, the interaction plots in Figure 3.11 reveal that

the interaction between speed and temperature is insignificant, as the lines are parallel confirming the deductions of ANOVA.

However, the lines on the thickness vs temperature plot are not parallel, indicating an interaction effect between these two factors on the β-phase content value. Specifically, the effect of thickness on the β-phase content value depends on the temperature, and vice versa. This means that optimizing one factor alone may not be enough to improve the β-phase content value, as the factors depend on each other.

To further explain this interaction effect, we observed that at higher temperatures, the smaller layer thickness recorded a larger increase in the β-phase content value compared to the larger layer thickness. However, at lower temperatures, the effect of thickness on the β-phase content value was less significant. The same trend was noticed in the thickness vs speed plot, where lower thickness only recorded a significant increase in the β-phase content value when the speed was lower.

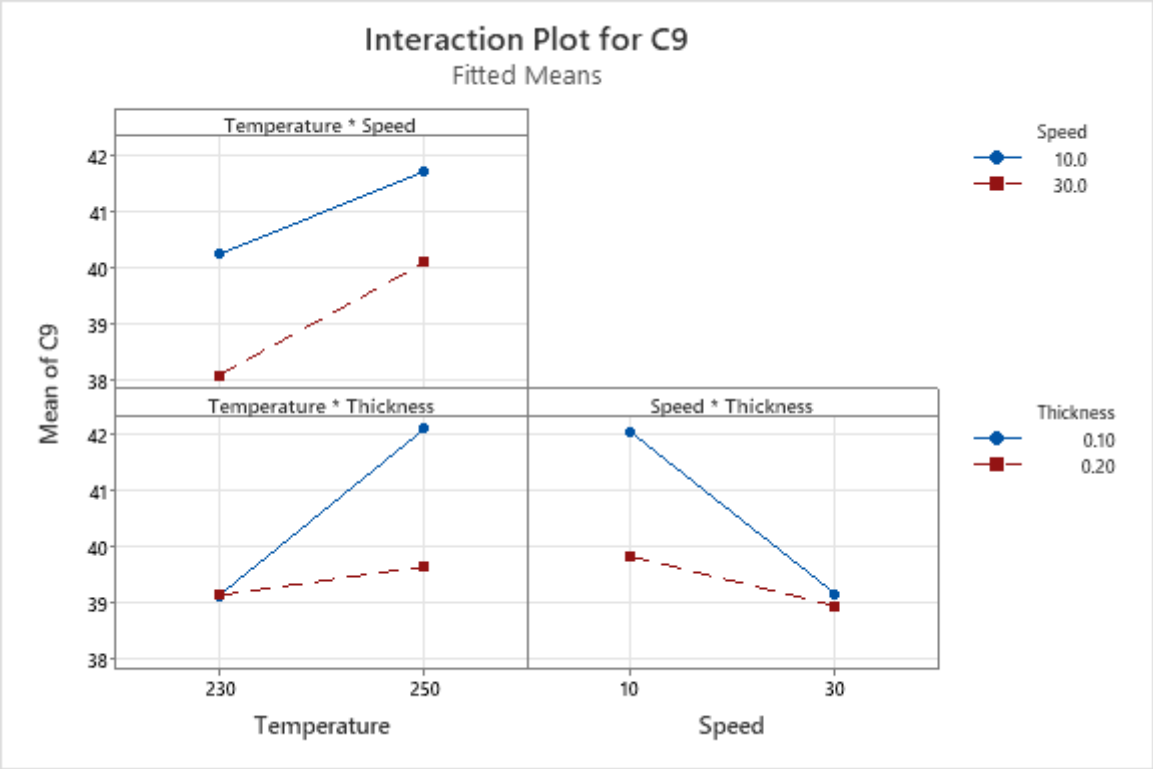

Figure 3.11 : Interaction Plots for the printing parameters

After analysing the interaction plots, it was interpreted that the optimized β-phase content value will be possible when the highest temperature, lowest printing speed and layer thickness are

used to fabricate the samples. The reason behind the deduction is that the interactions showed that an optimized factor required another optimized factor to record the highest value. However, the theory was to put to test by employing the response optimizer on the Minitab 21 software. In response optimization, you aim to identify the optimal combination of variable choices that collectively enhance a particular response or multiple responses. To quantify the optimized formulation's capability to fulfill the optimization objective, composite desirability is used as the metric. Composite desirability is a score ranging from zero to one that indicates how well the optimized formulation satisfies the optimization goal. If the composite desirability is zero, it suggests that one or more responses are outside the permissible range, while a composite desirability of one represents the ideal condition.

Based on a composite desirability of 0.96, the software predicted that a sample printed with specific parameters will record the maximum β-phase content value of 43.58%. These parameters are: temperature of 250°C, printing speed of 10mm/s, and layer thickness of 0.1 mm. The parameters match the parameters used to print Sample 3, and the average β-phase content of Sample 3 matches the predicted values generated by the software. These findings confirm the deductions regarding the interactions and demonstrate the efficacy of the model. The aforementioned parameters will be utilized to fabricate samples for further characterizations.

3.4.4 Field Emission Surface Electron Microscopy (FESEM)

The FESEM analysis was conducted to examine the surface topology of the optimized 3D printed sample. Figure 3.12 shows that occasional pores were present between the bead tracks. These results were anticipated due to the inherent characteristics of the 3D printing process and that similar outcomes were reported in previous studies on the 3D printed homopolymer by Momenzadeh [190]. A possible reasoning behind the presence of pores can be the extrusion process. As materials are being extruded from the nozzle, gaps or voids may occur causing the formation of pores.

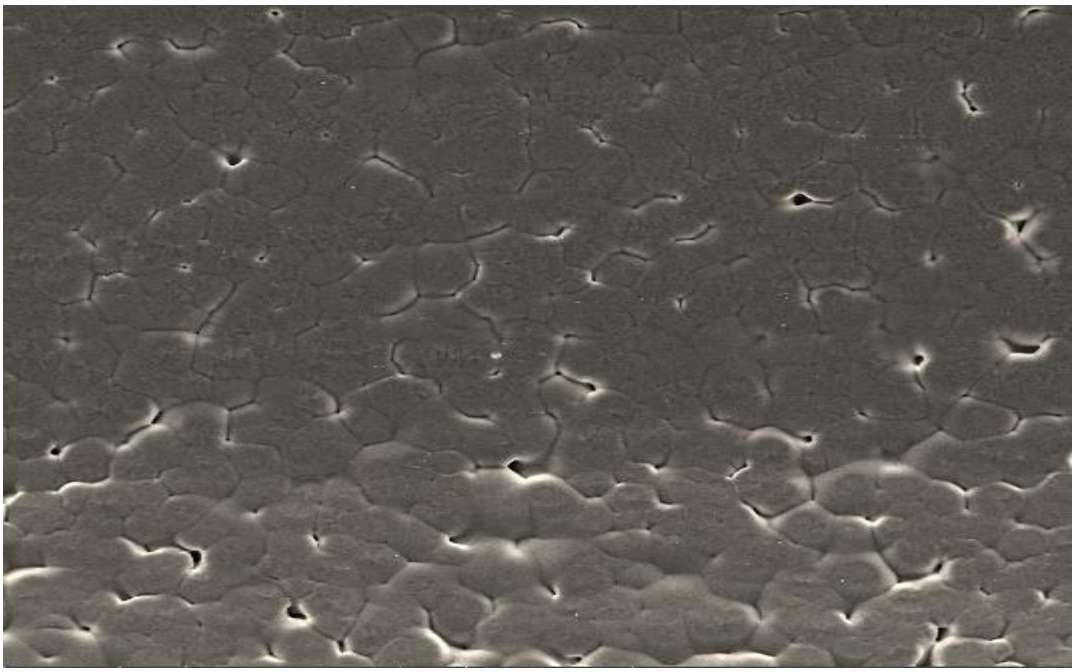

Figure 3.12 : FESEM image of optimized sample

3.4.5 Dynamic Mechanical Analysis (DMA)

In this study, DMA technique was employed to investigate the thermal and mechanical properties of 3D printed PVDF-HFP samples. While the optimized sample was the main focus of the analysis, all printing combination samples were also subjected to DMA testing to explore the effect of the printing parameters on the storage modulus, loss modulus, and other DMA-derived parameters. This approach aimed to provide insights that could inform further research on optimizing the mechanical properties of 3D printed PVDF-HFP or other polymers. To improve the reliability of the results, 3 samples of each printing combination were tested and an average value for all the results was obtained to assist in the analysis.

As shown in Table 3.7, the optimized sample exhibited the lowest storage modulus value at room temperature (28°C), whereas sample 4 recorded the highest value. Notably, the value for the optimized sample was 28% smaller than the highest recorded value. To compare the differences between the samples, DMA graphs were combined and presented in Figure 3.13.

Despite the value differences, both samples displayed a similar trend, where the storage modulus and loss modulus values decreased with increasing temperature. This trend can be attributed to the increased mobility of the polymer chains at higher temperatures, which reduces the average intermolecular forces and hence the stiffness and rigidity of the polymer.

Table 3.7: Average storage modulus values for all fabricated samples

Sample Number	Storage Modulus at Room Temperature/MPa
Sample 1	118
Sample 2	96.7
Sample 3	88
Sample 4	122
Sample 5	105
Sample 6	101
Sample 7	107
Sample 8	112

It is also worth noting that none of the samples exhibited peaks, indicating that the glass transition temperature did not occur within the testing temperature range. This similar trend was observed across all the remaining samples.

Based on these results, it can be inferred that the printing parameters primarily influenced the storage modulus values. Specifically, the samples with the lowest printing speed and highest printing parameters (such as Sample 2 and Sample 3) recorded the lowest storage modulus values, while the layer thickness was also a factor, with thicker layers recording higher storage modulus.

This finding supports the hypothesis that the residual stress caused by heating-cooling cycles may affect the mechanical properties of the samples. Moreover, the samples with lower printing temperatures displayed similar storage modulus values, regardless of the printing speed and

layer thickness. This suggests that a lower printing temperature may reduce the temperature difference between the deposited beads and the beads on the part, thereby decreasing the residual stress. This could infer an interaction between the parameters similar to the interaction observed in the β-phase analysis. These explanations serve as an initial analysis to confirm the need for further studies on the effects of printing parameters on the mechanical properties.

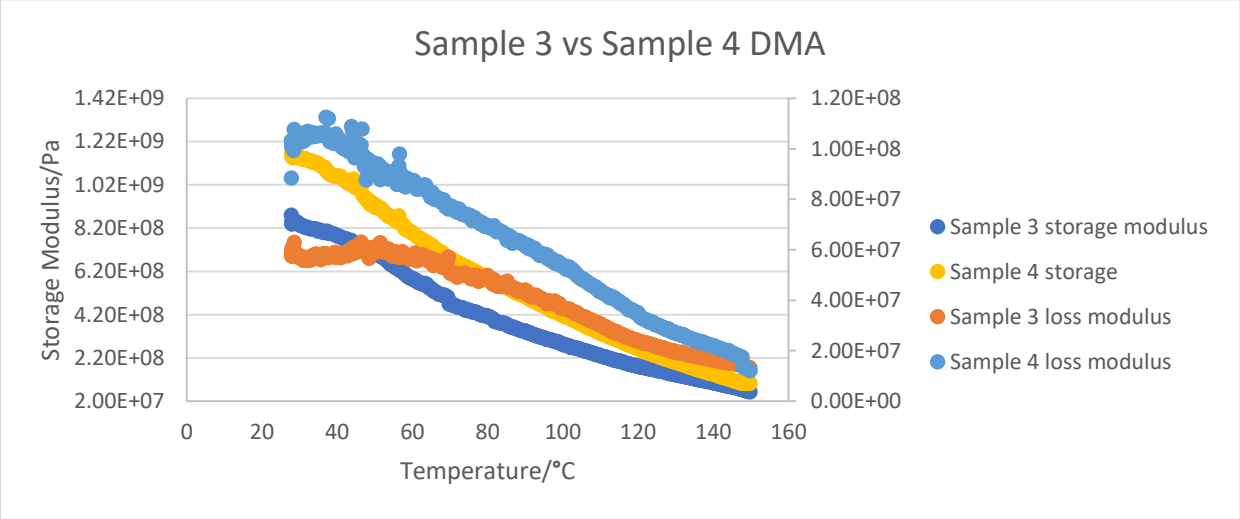

Figure 3.13 : DMA graph for Sample 3 and 4

3.5 Conclusion

In this chapter, PVDF-HFP was selected as the piezoelectric polymer to fabricate the force sensor while FDM was chosen as the fabrication method. However, the sensor can not be fabricated before understanding the effect of printing parameters on the piezoelectric performance and structural integrity of the samples.

Therefore, a DOE analysis was conducted to investigate the effect of printing parameters such as printing temperature, printing speed, and layer thickness on the β-phase content in printed samples. Increasing the residual stress on a part can enhance the β-phase content and, therefore, enhancing their piezoelectric performance. However, exceeding a certain threshold can cause warping or defects that compromise the structural integrity of the samples. The initial analysis results showed that the selected range of printing parameters resulted in no defects, confirming their feasibility for the study. The DOE analysis continued, and the results demonstrated that all printing parameters significantly influenced the β-phase content in printed samples.

Moreover, an interaction was observed between the printing parameters, where each parameter affected the response better when the other printing parameters were at their optimized values.

Using software optimization, the printing parameters were optimized, and the optimized sample was fabricated and tested. The DMA results confirmed that the optimized sample had the lowest storage modulus value at room temperature compared to the other samples, supporting the knowledge about the effect of residual stress on the mechanical properties of the samples.

4. Enhancing the Piezoelectric Performance of 3D Printed PVDF-HFP

4.1 Introduction

PVDF and its copolymers offer numerous benefits, but their piezoelectric capabilities fall short of conventional materials. As a result, many investigations have been carried out to enhance their piezoelectricity by focusing on increasing the content of β-phase crystals, which have a significant impact on the piezoelectric performance of PVDF and its copolymers. Post-processing techniques such as annealing, mechanical stretching, poling, and reinforcement of other materials have been used to enhance the piezoelectricity of PVDF.

Among the post-processing techniques, annealing is a commonly used heat treatment process that modifies the crystal structure and morphology of PVDF and its copolymers [60, 210]. Annealing can increase the degree of crystallinity and affect the crystallographic orientation of the β-phase in PVDF, leading to an increase in its piezoelectric properties. For instance, Oliveira, et al. [168] conducted a study investigating the effect of annealing on the piezoelectric properties of solvent-casted PVDF-TrFE films. Their results showed that annealing the films at a temperature of 130°C led to a significant increase in the piezoelectric coefficient d33, from 13pC/N for the casted film to a maximum of 18pC/N. However, a similar effect was not observed for PVDF-HFP, as reported by He, et al. [166]. In their studies, poling did not have much influence on the piezoelectricity, unlike the mechanical stretching process. It was observed that stretching the film increased the d33 from 5.4pC/N to 12.6pC/N, while annealing at 130°C only increased it to 6.8pC/N.

Another post-processing technique is the poling method, which involves applying an electric field or charges to a film to improve its polarization and piezoelectricity. Poling causes the alignment of the C-F dipoles in the crystalline/amorphous regions and the injection of space charges from the electrode to the film. For instance, a study by Kim, et al. [15] found that poling could increase the piezoelectric coefficient of PVDF d_{31} up to three times compared to unpoled samples and enhance the uniformity of the material's piezoelectric properties. It is

important to note that in order for the poling technique to have a significant impact on the piezoelectric properties of PVDF or its copolymers, the applied electric field must exceed the coercive field value of 50 MV/m [211].

Reinforcement techniques are preferred by researchers because of their rewarding benefits. Researchers typically reinforce piezoelectric polymers with fillers that have high piezoelectric properties to enhance the piezoelectric properties of the polymer matrix while maintaining its mechanical properties. The fillers also improve the alignment and change the orientation of the polymer chains to a preferred order with higher piezoelectricity. For PVDF and its copolymers, fillers act as a nucleation agent that induces the crystallization of the polymer in the β-phase and hinders the α-phase crystal formation. Researchers have reinforced PVDF and its copolymers with different fillers in several studies. For example, Yang, et al. [212] found that adding polydopamine surface-modified BTO to the PVDF matrix increased the β-phase content, with the highest recorded β-phase content being 68% when using 9wt% of the filler. Similarly, Gonçalves, et al. [213] reported that reinforcing PVDF with iron oxide magnetic nanoparticles also enhanced the β-phase content, with a maximum of 80% recorded when using 5wt% of the filler. Researchers have confirmed that employing a ternary structure in the PVDF matrix resulted in further enhancement of the β-phase [88].

As a result of the significant impact that the reinforcement technique has on enhancing the β-phase content of PVDF, we have decided to focus our study on this method. However, we have chosen to disregard the poling technique due to equipment limitations that only allow for an electric field strength of 800 kV/m, which, according to existing literature, will not have a significant influence on the material. In the upcoming subsection, we will discuss the selection of suitable fillers to be incorporated. Additionally, we will further analyze the feasibility of the poling technique and make a decision on whether to utilize it in our study or not, which will also be discussed in the following subsections.

4.2 Choosing the fillers

4.2.1 Secondary Structure selection

According to the aforementioned details regarding the reinforcement technique and the information reported in literature, it has been decided to reinforce the PVDF-HFP matrix with 2 fillers. Regarding the secondary structure in the matrix, several options such as ceramic,

natural, and organic fillers emerge as potential candidates. Conventionally, lead-based piezoelectric ceramic fillers have been used due to their superior piezoelectric performance in comparison to their counterpart fillers.

However, the downsides for using lead-based materials started to arise such as the environmental pollution and health risks igniting the spark to search for an alternative [214]. The alternative found by researchers was in the form of lead-free ceramic materials such as BTO, Zinc Oxide (ZnO), and potassium sodium niobate (KNN). The listed materials all possess a piezoelectric coefficient much higher than the organic and natural fillers making them suitable for this study due to not having any health or environmental risks.

To make the selection, several aspects have to be taken in to consideration such as: solubility in common solvents with PVDF, piezoelectric performance, and cost. Regarding the piezoelectric performance, BTO is reported to have the highest piezoelectric coefficient with a value of 190pC/N followed by 80pC/N recorded for KNN, leaving ZnO to be last with just 12.4pC/N [215-217]. Due to its low piezoelectric coefficient in comparison to the other candidates, ZnO is to be ruled out as an option. For the other aspects, BTO is completely solubly in multiple solvents common with PVDF such as DMF, DMA, and DMSO while KNN is only partly soluble in DMF and that is after long time of mixing (24 hours as stated by Abdullah, et al. [12]). It is also worth noting that BTO is readily available at local suppliers unlike KNN which needs to be synthesised in lab. Due to all these factors, BTO Is selected as the secondary structure to be incorporated as a filler in the PVDF-HFP matrix.

4.2.2 Ternary Structure Selection

For the ternary structure, researchers tended to employ different types of carbon based fillers. Carbon-based fillers are usually utilized to reinforce the PVDF matrix enhancing its' mechanical, electrical, and piezoelectric properties. Carbon-based fillers can come in several forms such as non-graphetizable (activated carbon and carbon black), carbon nanotubes, and graphite. As each form is different to the other, analysis of each of the carbon allotropes should be done to choose the filler to be used. The aspects to be considered in the analysis are the structural differences, cost, and the effect on β-phase formation and piezoelectricity of the PVDF matrix

.

Graphite

Graphite is a crystalline structure where the carbon atoms are arranged in hexagonal arrays where atoms are bonded to each other with strong covalent bonds Figure 4.1. The hexagonal arrays form a single layer which Is also called graphene. The layers are bonded to each other using the weak Van der Waal's interaction which explains the anisotropic behaviour of graphite. The electrical conductivity of graphite arises from the fact that each carbon is bonded is covalently bonded to 3 carbon atoms leaving a free electron which together will form a sea of delocalized electrons[218, 219]. As nucleating agents need to be of a very small size, graphene and its composites are usually investigated as nucleating agents and fillers. Graphene and Graphene oxide nanoplatelets are widely investigated fillers due to their high surface area and rumpled nature which cause strong interfacial interactions with the polymer matrix. Another reason for their popularity could be their relatively low-cost as they are produced from graphite.

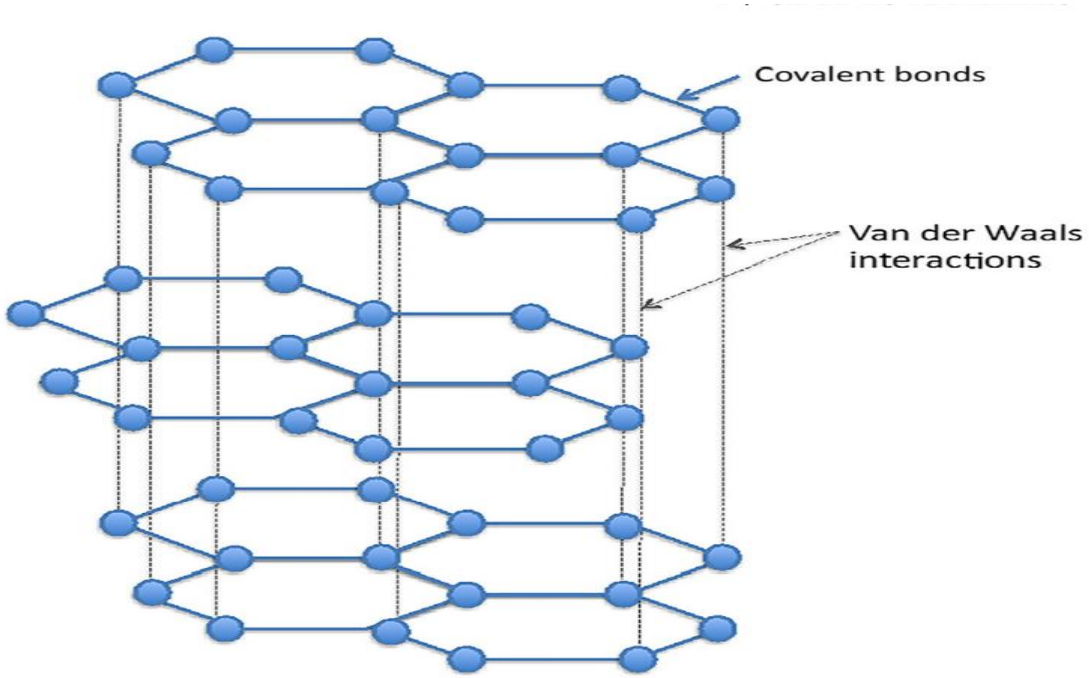

Figure 4.1 : chemical structure of graphite [208]

Graphene and its other forms have been used as fillers to improve the piezoelectricity of PVDF matrix by acting as a nucleating agent to enhance the β-phase formation. For instance, in a paper by Bidsorkhi, et al. [220] untreated graphene nanoplates (GNPs) were added to a PVDF matrix to improve the β-phase content. GNPs were synthesised by the thermal expansion of the commercial graphite intercalation compound.

Using the solution casting technique, films of PVDF/GNPs were fabricated. Despite the values of β-phase content were not reported, the FTIR results showed that increasing the weight fraction of GNPs resulted in a decrease in the A-phase content and an increase in the β-phase content simultaneously. This could be a proof that GNPs act as a nucleating agent facilitating the transformation of α-phase to β-phase. The reason behind GNPs inducing the β-phase could be that the electrostatic charges accumulated on the GNPs from the production process. The negative electrostatic surface charges will be attracted to the positive Hydrogen atoms while the positive electrostatic surface charges will be attracted to the negative fluorine atoms. The crystal phase that will allow this arrangement is the β-phase.

As mentioned in previous reports, the presence of carbonyl groups (C=O) in fillers helps enhance their dispersion in the PVDF matrix due to the strong interaction between the fluorine group (CF_2) and the carbonyl group [221, 222]. Following this fact, the fillers have been functionalized and carbonyl groups have been incorporated in their structures. For instance, El Achaby, et al. [223] investigated the effect of reinforcing the PVDF matrix with graphene oxide on the β-phase content. Graphite oxide was obtained by the chemical oxidation of natural graphite. the graphite oxide was exfoliated into graphene oxide nanosheets which were dispersed in the PVDF solution, and thin films were obtained by solution casting. El Achaby, et al. [223] reported that for 0.1wt% of Graphene oxide nanosheets, the β-phase content was 100%. The reason behind the pure β-phase polymorph is the strong interactions between the fluorine groups and the carbonyl groups. It was also reported in the paper that incorporation of graphene oxide enhanced the Young's modulus of the PVDF matrix.

Carbon nanotubes

Carbon nanotubes are members of the fullerene structural family which have a cylindrical nanostructure. They can be described as rolled tubes of graphene sheets where the walls are hexagonal rings while the ends are domed structures of six-membered rings, capped by a five-membered ring[224] (Figure 4.2). CNTs like graphene are very strong material due to the covalent bonds between the Carbon atoms.

CNTs can be classified as Single walled Carbon nanotubes (SWCNTs) or Multi-walled carbon nanotubes (MWCNT). The difference between both is that SWCNT consist of only one rolled sheet of graphene while MWCNT consist of several sheets rolled and the tubes are bonded together using the weak Van der Waal interactions. The radius of the tube and the tube chirality

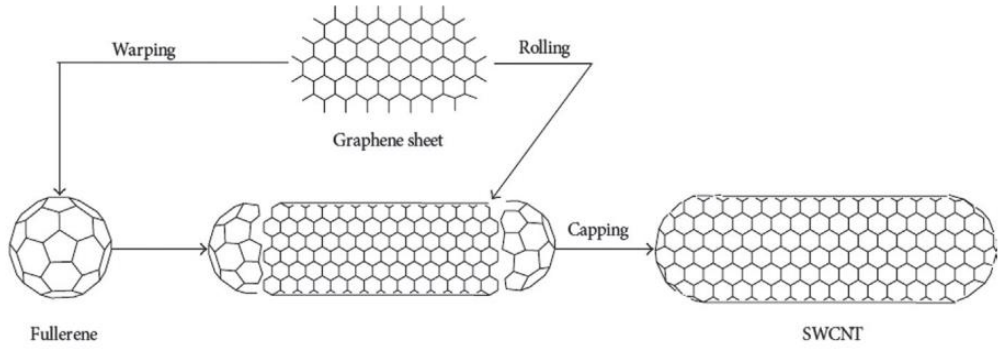

Figure 4.2 : schematic representation of how SWCNT are synthesised [212]

-the angle of orientation of the graphene sheet relative to the tube axis- determine the properties of the nanotubes. Due to their high aspect ratio, conductivity, and tensile properties, the CNTs are considered as an excellent filler candidate[225, 226].

CNTs in different forms have been investigated as fillers to improve the piezoelectricity of PVDF by acting as a nucleating agent to enhance the β-phase content. For instance, Ning, et al. [227] investigated the effect of incorporating untreated MWCNTs in PVDF on the piezoelectricity of the matrix. The solution casting technique was used to fabricate the composite films. The films were stretched and poled to enhance the β-phase content in the composite. It was reported that unstretched and unpoled composite films didn't record an increase in the β-phase when compared to the α-phase while the increase in the ratio of β-phase content to α-phase content was noticed after the stretching step was done. This could be explained by the fact that the CNTs acted as nucleating agents for all polymorphs since there are no accumulated surface charges either from the synthesis processes or the functional groups in CNTs. As known from literature, stretching the PVDF films result in a phase transformation from the α-phase to β-phase which explains the huge increase in β-phase content for stretched composite films compared to stretched pure films as the filler acted as a nucleating agent for the β-phase in that case. It is also worth noting that the optimum loading content of MWCNTs was 0.05%.

Knowing the fact that the presence of the Carbonyl groups in a filler's surface helps in the dispersion of the filler in the PVDF matrix, Manna and Nandi [221] investigated the effect of incorporating an ester-group functionalized MWCNTs in the PVDF matrix on the β-phase content for films produced by the solution casting and the melt casting techniques. It was reported that a 2wt% MWCNT/PVDF films produced by solution casting recorded 100% β-phase polymorph while the melt casted films recorded a maximum of 50% β-phase content.

The potential reason stated by the authors behind the pure β-phase polymorph is that the CNTs have a zigzag structure which matches the β-phase crystal structure; hence, the CNTs act as a nucleating agent inducing the β-phase crystallization.

Non-graphitizing fillers

A graphitizable carbon is the carbon structure that can be transformed to graphite under heating. The properties of graphitizable carbon are softness, lack of pores, and high density. On the other hand, non-graphitizing carbons are the low density carbon structures that are hard and porous, and do not yield graphite under heating[219]. Carbon black and activated carbon are examples on the non-graphitizing carbons. Carbon black which is produced by pyrolysis or the combustion of a compound containing hydrocarbons shares a similar structure to graphite as it is composed of large sheets of hexagonal arrays of carbon atoms bonded to each other.

The difference between both structures is the layer arrangement. As mentioned earlier, the layers are stacked on each other in a regular manner forming a tri-dimensional structure in the case of graphite. On the other hand, the layers in carbon black are not arranged in order forming concentric inner layers which results in a turbostratic structure. Due to the disorder in the layer arrangement, the carbon black has low crystallinity and can also be reported as an amorphous carbon[228, 229]. Activated Carbon also known as activated charcoal is obtained by chemical or thermal activation of carbon-rich materials. Similar to carbon black, activated carbon possesses a disorganized graphite structure[230]. The high internal surface area resulting from the presence of pores in the structure make carbon black and activated carbon potential candidates as fillers since increasing the specific surface area increases the surfaces available for nucleation[231]. It is worth mentioning that activated carbon has a higher specific surface area when compared to carbon black and the other fillers[232]. Carbon Black on the other hand has easier dispersion than graphene[233].

Wu, et al. [233] reinforced the PVDF-HFP matrix with carbon black(CB) to enhance its piezoelectricity. It was reported that CB(0.5%) resulted in the maximum voltage response of 3.68V which is 104% of the recorded voltage of the pristine polymer. The reasoning behind why the CB incorporation improves the piezoelectricity is that CB acts as a nucleating agent enhancing the crystallization in the β-phase. Higher contents of carbon black incorporation would result in degrading the level of crystallinity reducing the piezoelectricity.

Following the same investigation, Cai, et al. [234] investigated the effect of incorporating CB and graphene to the PVDF-HFP matrix on the β-phase and the voltage response. The graphene was added to improve the dispersion of the fillers in the matrix to improve the functioning of the fillers as nucleating agents. The results showed that fillers of loading content 0.5%CB and 0.02%graphene resulted in approximately pure β-phases after stretching and poling. The results prove that the graphene helped in the dispersion in the matrix. It was also reported that the incorporation of the fillers improved the mechanical properties of the matrix as a loading content of 0.3% CB and 0.03% graphene recorded a Young's modulus of 1073.5 MPa which is 119% higher than the pristine polymer.

Selection

As all fillers discussed proved to act as nucleating agents and improved the β-phase crystallization when the composite contains another filler that improves the β-phase or when the composite was under a process that transformed the α-phase to β-phase. The only things to be considered will be the cost, ease of mixing, and electrical conductivity. When it comes to the ease of mixing, all untreated fillers were mixed easily with the PVDF solution. Despite the functionalization of the fillers improve the β-phase crystallization, the process will not be of great advantage since the other filler incorporated will be improving the β-phase. As all fillers studied fulfilled their potential when incorporated in the PVDF matrix and the β-phase content values were close for all untreated fillers; then, the cost will be the only factor to take into consideration. Despite Carbon Black being much cheaper than other carbon fillers, it remains 50 times more expensive than activated carbon [235, 236]. As a result, activated carbon has been selected as the ternary structure in the PVDF-HFP matrix. This decision was made because it is the most cost-effective option available and also serves to address the existing gap in the literature, given the dearth of studies examining the use of activated carbon as a ternary structure.

4.3 Methodology

4.3.1 Solvent Selection

To produce a printable filament for a PVDF composite, thin films of the composite must first be fabricated. The solution casting technique has traditionally been used in previous studies to create films of PVDF and its copolymers. However, the use of hazardous solvents such as N,N

dimethylformamide (DMF) and Dimethylacetamide (DMA) in the reinforcement process has raised significant concerns [13]. These protic solvents have been employed in nearly all studies involving the strengthening of PVDF or its copolymers. Recently, attention has shifted to the use of environmentally friendly solvents like dimethyl sulfoxide (DMSO). Satapathy, et al. [237] reported that, when processed correctly, DMSO could yield a high β-phase content. Importantly, DMSO has not yet been utilized in a solution casting process for reinforcing PVDF or its copolymers with fillers.

To investigate whether DMSO can serve as a safer alternative to the toxic solvents currently in use, it has been decided to use it as the solvent in the solution casting process for creating thin films of PVDF-HFP composites.

4.3.2 Materials

Polyvinylidene fluoride-hexafluoropropylene (PVDF-HFP) and Barium Titanate (BTO) nanoparticles were purchased from Sigma-aldrich in the form of pellets and powder, respectively. Untreated activated carbon and dimethyl sulfoxide (DMSO) were acquired from EvaChem and chemAR, respectively.

4.3.3 Solution Casting process

The purpose of this study was to enhance the β-phase content in a PVDF-HFP matrix, which was achieved by fabricating several films with different formulations using the solution casting technique.

To make the films, 2.25g of PVDF-HFP pellets were dissolved in 25ml of DMSO at 85°C for 90 minutes. After the pellets completely dissolved, the specified amounts of BTO and UAC were added to the solution. The solution was vigorously stirred using a magnetic stirrer at 1200rpm for 30 minutes and then sonicated for an additional 30 minutes. The resulting solution was poured onto a glass substrate and placed in an oven at 100°C for 24 hours to yield a 0.4mm thick film (Figure 4.3). Table 4.1 shows the formulations of the films that were fabricated to determine the optimal filler content in the PVDF-HFP matrix, which were generated using the optimal mixture Design of Experiments mode available in Design Expert software®. More information about the Design of Experiments and its various types will be discussed in the subsequent subsection.

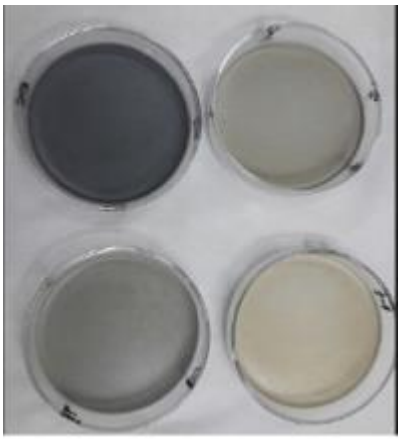

Figure 4.3: solvent casted samples after oven drying

4.3.4 Mixture Design of Experiments

Previous studies on the reinforcement of PVDF and its copolymers lacked a statistical approach for optimizing the response being investigated. In this study, we will address this gap by utilizing the optimal mixture design. Mixture design of experiments (DOE) is a statistical methodology used to optimize the formulation of a product composed of several ingredients [238]. The primary objective of the method is to predict how different components affect the response, which is usually the quality or performance of the product. The most commonly used types of mixture DOE are simplex centroid, simplex lattice, and extreme vertices.

In the simplex centroid method, center points are used to predict the relationship between the components and the response, while simplex lattice uses scattered points to predict the function more accurately. The simplex centroid method is often used to screen out the important factors, while simplex lattice is used to predict functions with a high-order polynomial accurately. Unlike these two methods, the extreme vertices method does not utilize the entire triangle plot since it is employed when one or more factors are constrained between certain values [239].

Design Expert software provides three optimal design options to consider when conducting a mixture DOE, namely D-optimal, A-optimal, and IV-optimal. D-optimal design is preferred for factorial and screening designs to identify the most critical factors by selecting points that reduce the volume of the confidence ellipsoid of the coefficients [240].

A-optimality minimizes the average variance of the polynomial coefficients. The 'IV' optimal design utilizes an integrated variance criterion that reduces the mean variance of responses in a designated area of interest [241].

In this study, the IV-optimal design was selected because of the lower average variance across the region of interest. The study aimed to reinforce PVDF-HFP, which means that the content of PVDF-HFP will never be zero. Hence, PVDF was constrained with a lower bound, implying that the extreme vertices method must be implemented. Since the optimized mixture would be used for 3D printing, the upper bound was set to 15% for fillers, as using a higher content of BTO was reported to cause clogging in the printing nozzle [209]. The lower bound was chosen as 5% to minimize the area of interest to ensure the accuracy of the results. On the other hand, values between 0.2-0.5% were reported as the optimal content when Carbon fillers, such as CNTs and carbon black, were used to reinforce the PVDF matrix [242-244]. Therefore, the activated carbon was bounded by 0 and 1%.

Using the extreme vertices IV-optimal design on the Design Expert software, 16 runs were generated for several formulations to be FTIR tested, with 11 of them to be tested, and the remaining five were done as replications. The software-assigned formulations and testing results are listed in Table 4.1. The mathematical relations between the β-phase fraction and the fillers can be estimated through multiple regressions and analysis of variance (ANOVA).

Table 4.1 : Formulations generated by Design Expert and the responses collected from FTIR

Run	PVDF (%)	BTO (%)	UAC (%)	β-phase (%)
1	84	15	1	66.8091
2	95	5	0	62.48
3	85	15	0	67.118
4	90.67	8.33	1	61.1676
5	87.25	12.5	0.25	60.5179
6	94.33	5	0.67	63.7859

7	89.5	10	0.5	66.5505
8	90.67	8.33	1	61.5764
9	94.33	5	0.67	63.5552
10	92.25	7.5	0.25	62.8303
11	87.33	11.67	1	64.6669
12	89.5	10	0.5	66.9354
13	89.5	10	0.5	68.1299
14	91.67	8.33	0	59.7029
15	84	15	1	66.9206
16	88.33	11.67	0	57.8226

4.3.5 Extrusion and Printing

Once the mixture design analysis was complete and an optimized formulation have been developed. In order to obtain the composite filament, 40 films (100g) of the optimum formulations were fabricated and desiccated into very thin squares (3mmX3mm) for the extrusion process. The mixture was introduced into the single-screw extruder (Wellzoom C) provided by the University of Putra Malaysia. The temperature of all heating zones was set to 210℃ and the extrusion speed was maintained at a constant 40 rpm. The reason behind the difference between the extrusion temperatures in this setup and the Filastruder setup mentioned in the previous chapter is that the extruder in this situation was assembled in the horizontal direction as shown in Figure 4.4. The extruded filament was passed through a water bath maintained at room temperature to solidify it.

However, the equipment did not have an auto-calibration winding system, so the diameter of the filament was adjusted manually to remain within the range of 1.6-1.75 mm by adjusting the speed of the filament tractor. Due to the limited time in the facility, a high extrusion speed was

employed resulting in the range of filament diameters achieved which still fall within the range accepted by the 3D printer (1.75±0.15mm). Figure 4.5 shows the composite and the pure filaments next to each other. It is worth noting that due to purging of the remaining materials in the extruder only 50g of composite filament were obtained. The 3D printer, Creality Ender-3 Max, was used to print the composite samples for testing.

Figure 4.4 : WellZoom C extruder and manual winder setup

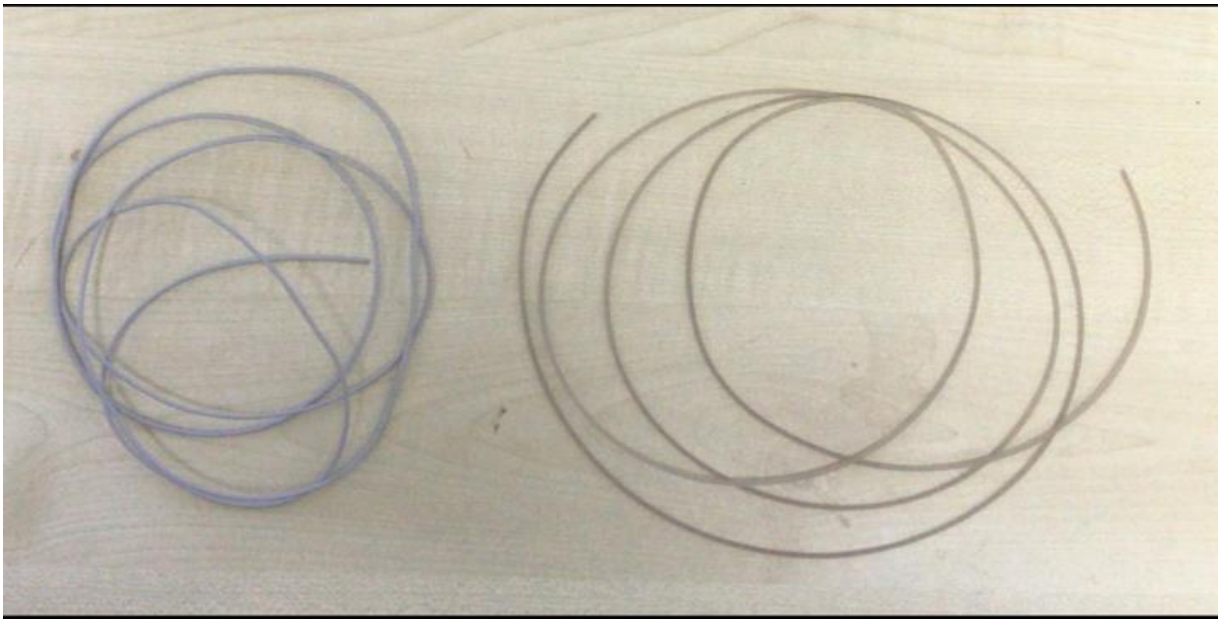

Figure 4.5 : Composite and Pure filaments (Composite to the left)

Printing parameters play a critical role in determining the properties of 3D-printed materials. Previous research has shown that a combination of the lowest printing speed, thinnest layer thickness, and highest printing temperature leads to the highest β-phase content value.

Consequently, we selected a printing speed of 10mm/s, a thickness of 0.1mm, and a printing temperature of 250°C for our experiments.It is important to note that we encountered challenges when printing at temperatures lower than 250°C. Specifically, underextrusion occurred, resulting in damaged printed samples. Furthermore, the printer's maximum temperature was 250°C, which constrained our ability to explore higher temperatures. Given these limitations, we chose not to conduct a Design of Experiment (DOE) analysis. Additionally, since the thickness and speed were already set to their minimum values, further optimization was not necessary. Another reason the DOE analysis was not conducted was to conserve resources, as only 50g of filament was available for the experiments.

4.3.6 Characterization Techniques

FTIR

The FTIR spectroscopy was utilised in several studies in this chapter. As mentioned earlier, the FTIR spectroscopy is often used to study the chemical composition and structure of polymers. In this study, FTIR was employed to aid evaluate the β-phase content in PVDF-HFP composite films fabricated using different techniques. Initially, FTIR was used to characterize the films of certain formulations specified by the Design Expert Software listed in Table 4.1. After the analysis was complete, the optimized formulation was also characterized by FTIR. A final characterization took place when FTIR was utilised to characterize the printed composite sample. Similar to the previous chapter, the vibrational spectra of all samples were obtained using a PerkinElmer FTIR spectrometer with wavelengths between 600 and 1400 cm-1 and a resolution of 2 cm-1.

DMA

DMA was used to assess the mechanical properties of the printed composite. The results obtained will be used to compare the results to the pure printed samples obtained in the previous chapter. Dynamic mechanical analysis (DMA) experiments were conducted using the PerkinElmer DMA8000 instrument in tension mode at a frequency of 20 Hz and a heating rate of 5°C/min over a temperature range of 30 to 150°C.

FESEM

FESEM was used to characterize the solution casted films and the printed composite samples. The images obtained from each sample were used to identify the relationship between the fillers and the presence of pores and microcracks. In addition, the printed sample was compared to the pure printed images obtained last chapter. The same parameters and instrument as the previous chapter were used to conduct the test.

Differential Scanning Calorimetry (DSC)

Differential Scanning Calorimetry (DSC) analysis was conducted on extruded filaments and 3D printed samples to investigate the effect of the fillers and the 3D printing process on thermal properties such as melting point, crystallinity, and possible phase changes.

DSC works by measuring the difference in heat flow between a sample and a reference material as they undergo controlled heating or cooling. As the temperature changes, the sample undergoes phase transitions such as melting, crystallization, glass transition, and chemical reactions, which are accompanied by the absorption or release of heat. These changes are detected by the DSC instrument as a change in heat flow [208]. The DSC analysis was performed by the DSC Q2000 TA instrument in a nitrogen atmosphere from room temperature to 200°C with a heating rate of 5°C/min.

Thermogravimetric Analysis (TGA)

Thermogravimetric analysis was performed by TGA DSC 1 Mettler Toledo instrument to investigate the thermal stability of the samples. The process involved subjecting the samples to heat, where a 10°C/min ramp was chosen to raise the temperature from room temperature to 800°C in a nitrogen atmosphere..

Electromechanical Characterization

In order to confirm the piezoelectricity of the fabricated samples, an electromechanical test was conducted to measure their voltage response. The objective of this test was to provide data that could be used to calculate the sensitivity of the samples. The test setup was designed to be simple and cost-effective, utilizing a support beam, an impact hammer, aluminum foil electrodes, and a multimeter (Figure 4.6).

The samples tested in this study included 3D printed pure polymer, 3D printed composite, and optimized solution-casted samples. Three samples of each type were fabricated and investigated, and their average voltage value was obtained. As shown in Equations 2.12 and 2.14, the thickness of the samples was considered to be the only geometrical aspect in the samples to affect the response; therefore it was controlled at a value of 0.4mm as the solution casted samples are fabricated to that thickness. As mentioned, the cross-sectional area of the samples did not have any influence; therefore, the printed samples were printed in a circular shape of 30mm diameter while the films were cut in approximately 40x40mm^2 squares.

The experiment was conducted as follows: 15x15mm^2 aluminum foil electrodes were placed on top of the samples, and the entire assembly was positioned on the support beam. Force was applied to the samples using an impact hammer. A data acquisition system was used to record the measured values, while the voltage response was recorded using a simple circuit linked to the multimeter. Further details regarding the results and analysis will be addressed in the upcoming section.

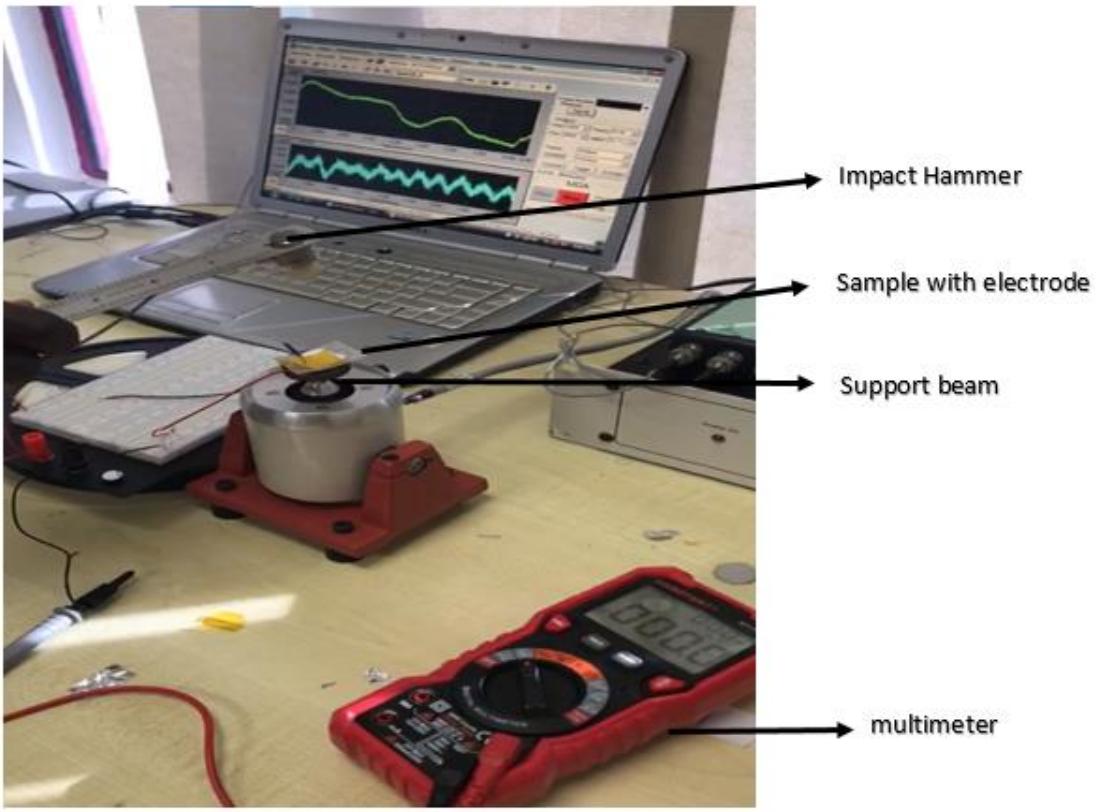

Figure 4.6 : Electromechanical Test Setup

4.4 Results and Discussion

4.4.1 Initial Analysis

The purpose of this research was to optimize the filler content in a PVDF-HFP matrix while testing the feasibility of using DMSO as an alternative solvent. To quantify the β-phase content, the β-phase content was calculated using equation 3.1, and the results were tabulated in Table 4.1. Apart from the values found in Table 4.1, a pure PVDF-HFP film was fabricated to aid in investigating the effect of fillers. With the pure film recording a β-phase content of 57.024%, it is clear that employing reinforcements resulted in a β-phase enhancement as all the formulations recorded a higher β-phase content. The maximum value (68.130%) was recorded by Run 13 with a formulation of 10wt% BTO and 0.5wt% UAC while the minimum value (57.822%) was recorded by Run 16 with a formulation of 11.67wt% BTO. From the first glance on the results in Table 4.1, it would be safe to assume that an increase in the filler content would result in an increase in the β-phase content; however, this assumption is to be tested in the mixture of design analysis section.

Arriving at the second aim of the study, the viability of using DMSO as an alternative solvent to DMF and DMA was tested by comparing the β-phase content for PVDF composites in literature. Table 4.2 lists some of the polymer/composites fabricated using the solution casting technique and their respective β-phase content. From the works available in literature, there are 3 works that are considerably similar to this work; therefore, their results can be compared. In Wu, et al. [245] and Wu, et al. [233], the highest recorded β-phase content for a pure PVDF-HFP film was 58% and 59%, respectively, while in our work the pure film recorded a β-phase content of approximately 57%. For Kim, et al. [211], it was reported that the highest recorded β-phase content for a PVDF/15wt% BTO was 65.4%. Despite the different polymer matrix, the same formulation with PVDF-HFP as the matrix recorded 62.48% as shown in Table 4.1. As the pure polymer fabricated using DMSO approximately matched the values reported in 2 studies, it is safe to assume to that DMSO can be used an alternative solvent.

Table 4.2 : β-phase content of PVDF and its copolymers composites fabricated by solution casting in literature

Polymer Matrix	Filler/s	Solvent/s	β-phase content	Reference
PVDF-HFP	0.3wt% silver nanowires	DMF	87%	[245]
PVDF-HFP	-	DMF	58%	[245]
PVDF	50wt% PZT	NA	57%	[246]
PVDF	15wt% BTO	DMA	65.4%	[211]
PVDF-HFP	20wt% BTO	DMF	45.65%	[247]
PVDF-HFP	20wt% BTO	NMP	42.15%	[247]
PVDF	5wt% Fe_2O_3	DMF	80%	[213]
PVDF	9wt% BTO	DMF	68%	[212]
PVDF-HFP	-	DMF	59%	[233]
PVDF-HFP	0.8wt% Carbon Black	DMF	80%	[233]
PVDF-TrFe	-	DMF	75%	[248]
PVDF-TrFe	5wt% CaZ	DMF	79%	[248]

4.4.2 Mixture Design Analysis

A set of experiments were conducted to obtain the required responses for the extreme vertices design. Utilizing the regression fitting technique with a 95% confidence, the Design Expert software generated a cubic model fitting the obtained responses. The model used to predict the β-phase content in terms of actual mixture components is postulated in Equation 4.1.

$$\beta_{phase} = 0.478204A + 340.97290B - 719873C - 5.52181AB + 10826.21333AC + 10932.46757BC - 73.53735ABC + 0.021873\,AB(A-B) - 36.27953\,AC(A-C) - 37.85716\,BC(B-C) \quad (4.1)$$

Where A, PVDF content (wt%); B, Barium Titanate content (wt%); and C, Untreated Activated Carbon (wt%).

To validate the model, the actual responses (experimental results) were plotted against the predicted results as illustrated in Figure 4.7.

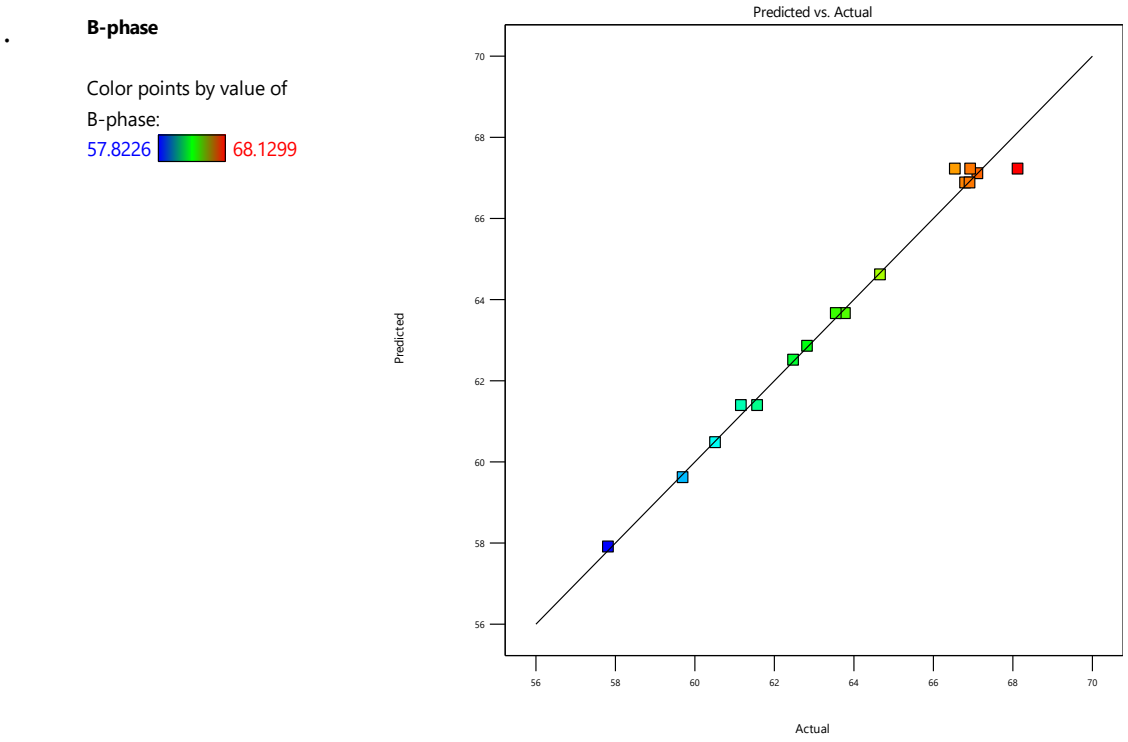

Figure 4.7: Predicted β-phase response (from model) against Actual β-phase response (from experiments)

With an R-sq of 0.9897 and an adjusted R-sq of 0.9741, the model was deemed extremely efficient in predicting the β-phase content for different formulations.

The residuals plots shown in Figure 4.8 also demonstrate the scattering of the response residuals along the plot which further confirms the adequacy of the obtained model.

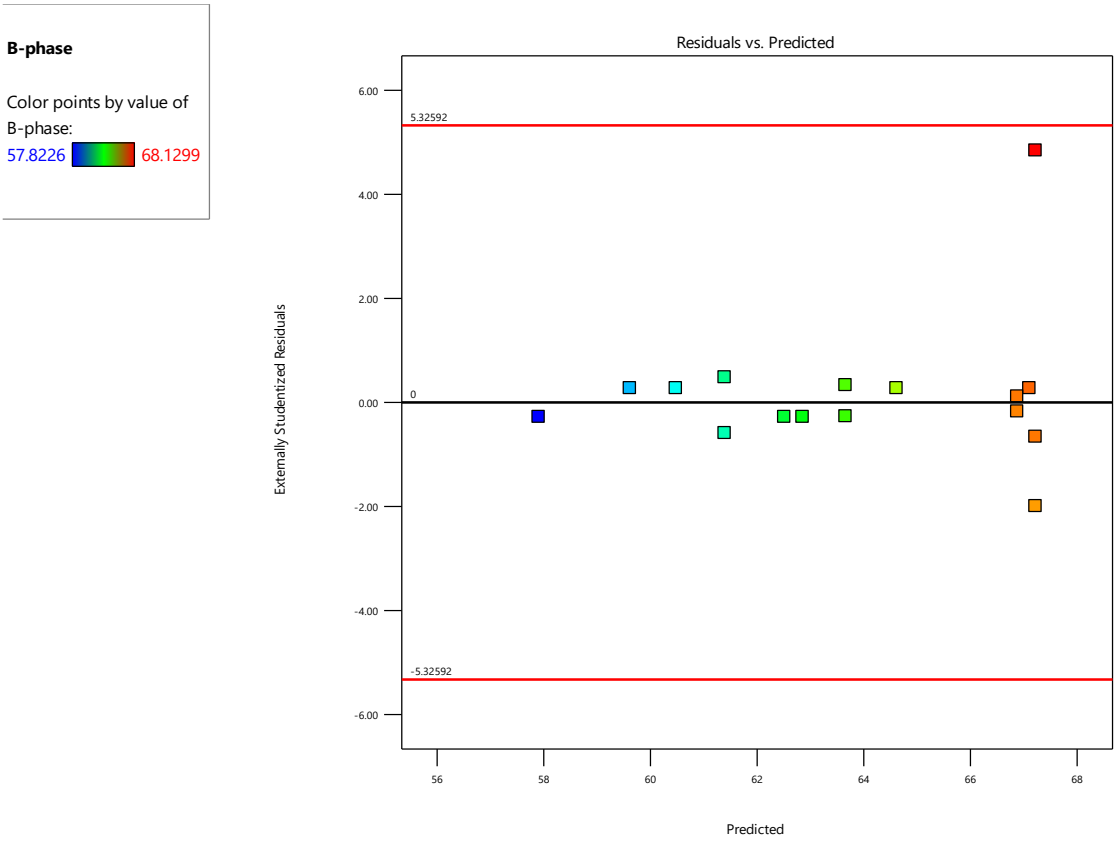

Figure 4.8 : Predicted against residuals plot

An analysis of variance (ANOVA) was carried out utilising the Design Expert software to look into the model's significance and relevance. Additionally, ANOVA displays the impact of the individual factors and the interplay of variables on the mixture's response. The ANOVA findings can be found in Table 4.3

The significance of the model can be investigated by determining the Fischer value (F-value). Calculated through the division of two mean squares, F-values represent the ratio of explained variance to unexplained variance. According to the model F-values of 63.81 for β-phase content's response, the regression model can account for the majority of the variation in the response.

To determine whether the F-ratio is large enough to suggest statistical significance, the related p-value is used. The model could not be regarded as statistically significant if the p value was greater than 0.05. As a result, the regression equation has a substantial correlation with the response since the recorded p-values are lower than 0.0001. Furthermore, the linear mixture and all variables interactions were deemed significant due to their p-values recording a value less than 0.05.

Table 4.3 : ANOVA table displaying the statistical analysis derived from the β-phase content values

Response : β-phase						
Source	**Sum of Squares**	**Df**	**Mean Square**	**F-value**	**p-value**	**Remarks**
Model	143.1	9	15.9	63.81	< 0.0001	significant
Linear Mixture	29.57	2	14.78	59.33	0.0001	significant
AB	46.2	1	46.2	185.41	< 0.0001	significant
AC	18.77	1	18.77	75.33	0.0001	significant
BC	19.53	1	19.53	78.36	0.0001	significant
ABC	18.26	1	18.26	73.3	0.0001	significant
AB(A-B)	14.91	1	14.91	59.81	0.0002	significant
AC(A-C)	17.35	1	17.35	69.61	0.0002	significant
BC(B-C)	19.71	1	19.71	79.1	0.0001	significant
Residual	1.5	6	0.2492			
Lack of Fit	0.0223	1	0.0223	0.0759	0.794	not significant
Pure Error	1.47	5	0.2946			

4.4.3 Effects of the mixture components on the β-phase content

As mentioned earlier, The ANOVA table confirmed the significance of all the variables and their effect on the β-phase content for any given formulation. The sign coefficients dictate whether a variable has a positive impact or a negative influence on the response. For instance, the analysis of the linear terms deduce that PVDF-HFP and Barium Titanate have a positive impact on the β-phase content while activated carbon influenced the β-phase content negatively.

To further examine the effect of the variables on the β--phase content, response trace plots can be utilized. Available in Figure 4.9, response trace plots employ the fitted model to depict the outcome of altering the respective variable along a hypothetical line that connects the reference blend to a vertex [249]. According to Figure 4.9, for a weight fraction of $84.0 \leq PVDF\text{-}HFP \leq 95.0$, $5.0 \leq BTO \leq 15.0$, and $0 \leq AC \leq 1.0$, it is evident that Barium Titanate and Activated carbon influence the β-phase content response significantly. Furthermore, demonstrates how the reinforcement of Activated Carbon beyond a certain threshold resulted in a redundant response while Barium Titanate showed a sinusoidal behaviour where the response was maximised toward the upper bound. As the variables could change simultaneously, response trace plots may not be sufficient to understand the effect of the alterations; therefore, the 3D surface plots must be considered. The 3D surface plots are able to link the predicted response to the variables as shown in Figure 4.10.

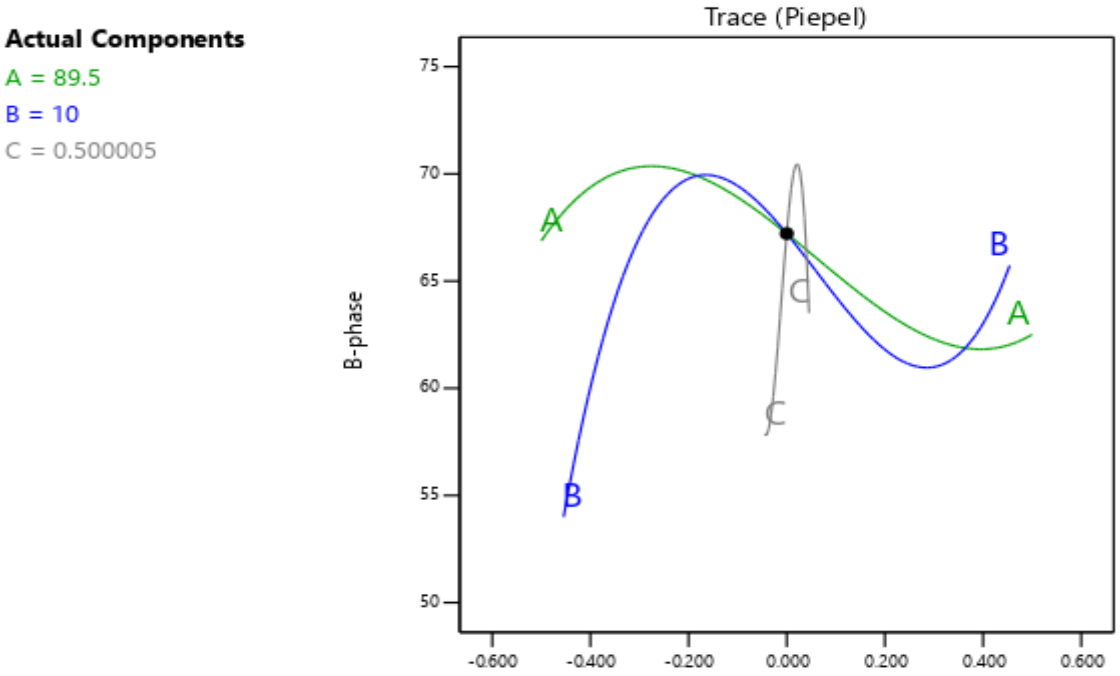

Figure 4.9 : Response Trace Plots

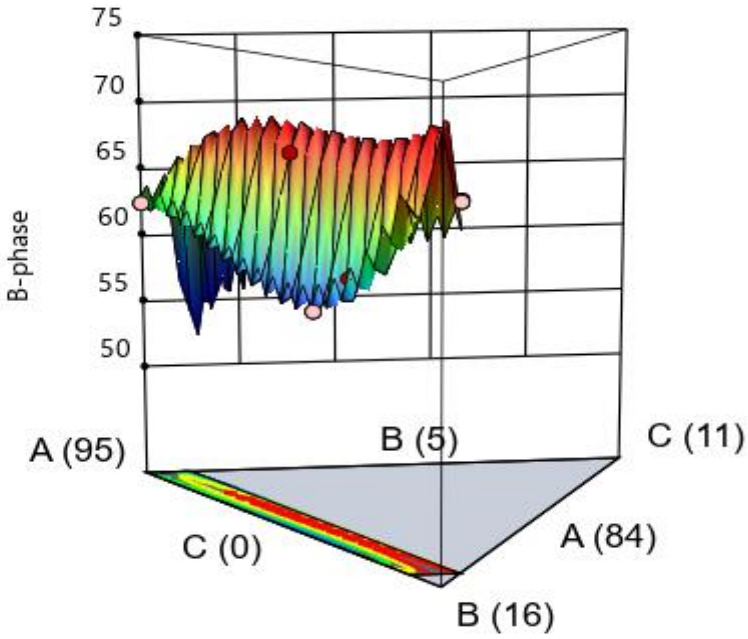

Figure 4.10 : 3D surface plot of the response

4.4.4 Response Optimization

The main aim of this study was to enhance the β-phase content in a PVDF-HFP matrix by the reinforcements of Barium Titanate and Activated Carbon as fillers. As shown in Figure 4.10, the β-phase content is maximized for a certain mixture of the components apart from the tested formulations. The current situation requires the employment of response optimization process provided by The Design Expert software. Response optimization utilizes the fitted model to predict the combination provides a response optimization process that can be employed to obtain the formulation that maximizes the β-phase content. The response optimization process enables you to pinpoint the combination of variable choices that collectively improve a particular response or a collection of responses [250]. Composite desirability is the metric used to quantify the optimized formulation's ability to satisfy the goal of optimization. With a range varying from zero to one, a composite desirability of zero signifies that one or more responses are outside the permissible range while one represents the optimum condition.

With a composite desirability of 1.00, the formulation containing 84.21 wt.% PVDF-HFP, 15.00 wt.% Barium Titanate, and 0.79 wt.% Untreated Activated Carbon was predicted to have a β-phase content of 72.504%. To verify the values obtained, five films of the same formulation were fabricated and tested. The mean experimental results showed that the formulation

recorded a β-phase content of 71.895% that lies within the confidence of intervals specified by the software and with an error margin of 0.85%.

4.4.5 FESEM Results

After fabricating the printed samples, field emission scanning electron microscopy (FESEM) was utilized to characterize the following samples: Runs 2 and 6 from Table 4.1, optimized solution casted sample, and the printed composite sample. To recall, Run 2 consisted of a solution casted sample with the formulation 95 wt.% PVDF-HFP and 5 wt.% BTO while Run 6 was a solution casted sample with the formulation 94.33 wt.% PVDF-HFP, 5 wt.% BTO, and 0.67 wt.% UAC. These samples were selected to investigate the impact of fillers and processing techniques on the morphology of the samples.

Figure 4.11 shows that the solution casted samples exhibited a characteristic spherulitic pattern, and small pores were present in the regions between the spherulites. These pores are formed during the solidification process, as the polymer crystallizes, the spherulites grow and absorb the liquid polymer phase between the crystallized polymer. Once crystallization is complete, there is no liquid phase left, resulting in a gap between the crystallized spherulites. However, Figure 4.11(a) shows that the BTO fillers were dispersed uniformly in the matrix, leaving only a small number of pores. As the filler content increased, such as in the optimal casted sample, the fillers agglomerated in certain areas and a greater number of pores were observed. The increased number of pores could be attributed to the agglomeration of the particles, which prevented the material from forming a uniform structure, leading to gaps or spaces between the particles.

The effect of incorporating carbon fillers was also investigated by comparing Runs 2 and 6. As shown in Figure 4.11(a) and (b), the amount of particles dispersed in the matrix was much higher, recording a higher number of pores, possibly due to the agglomeration shown in the figure.

Using Figure 3.12 as a reference to compare the printed composite FESEM image in Figure 4.11(d), it is evident that the composite printed sample lacked the spherulitic pattern observed in the solution-casted samples and the pure polymer printed samples.. A potential reason behind the phenomenon could be that the presence of agglomerates in the feedstock can potentially interfere with the formation of spherulites during FDM printing and affect the microstructure and properties of the printed part. This is consistent with the findings reported by Kim, et al.

[251], where the solution-casted samples exhibited the spherulitic pattern, unlike the 3D-printed samples.

Moreover, it can be observed that the 3D-printed composite contained more voids and larger micro-cracks when compared to the pure polymer. The agglomeration of fillers in the composite initially caused pores in the film, which was used to fabricate the filament used to print the composite sample. As the pore content was already high, the fused deposition modeling (FDM) technique further increased the porosity and voids, resulting in a higher pore content in the FESEM image of the printed composite.

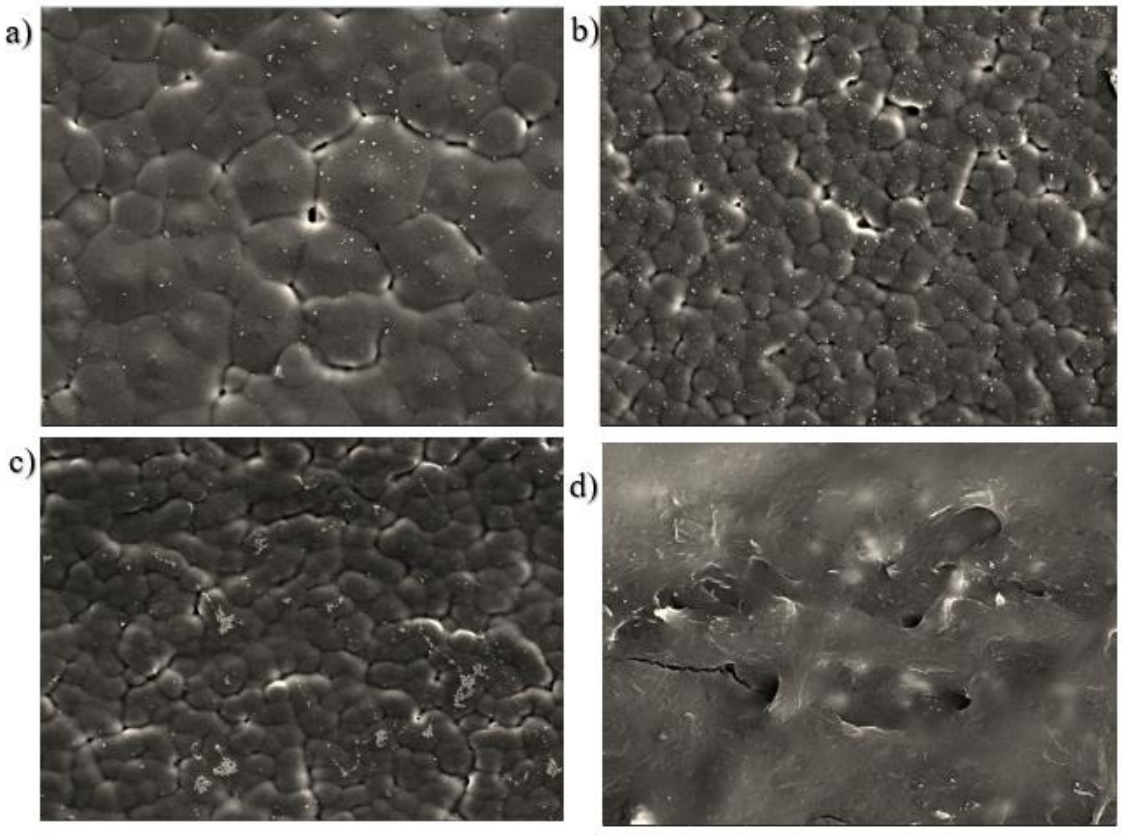

Figure 4.11: FESEM images of a) Run 2 b) Run 6 c) Optimal formulation solution cast d)printed composite

4.4.6 DMA results

The DMA technique was employed to investigate the impact of fillers' mechanical and thermal properties on the viscoelastic behavior of the printed composite. The focus was on analyzing the storage modulus, loss modulus, and phase changes. Prior to the DMA testing, it was hypothesized that incorporating fillers would enhance the storage modulus, given that both fillers had higher stiffness than PVDF-HFP. However, as observed in Figure 4.12, the pure

printed sample demonstrated higher storage modulus values for all temperatures, with a recorded value of 880 MPa at room temperature, compared to the composite sample's 320 MPa. The lower storage modulus in the composite sample can be attributed to the presence of more voids, as confirmed by the FESEM images in the previous subsection. Voids can act as stress concentrators, thereby reducing the stiffness, strength, and toughness of the material. Another possible reasoning could be the reduced crystallinity which is confirmed later in the upcoming subsections since the crystalline regions tend to contribute to the overall stiffness of the material; therefore, a reduced crystallinity would result in a reduced storage modulus.

A similar trend was observed in the loss modulus, where the composite sample recorded smaller values than the pure sample. The same reasoning can be applied to explain this trend, as voids or defects can lead to a weaker interphase region, reducing the interfacial bonding between the matrix and filler particles. This weak interphase region can subsequently impact the energy dissipation mechanism in the material, leading to a decrease in the loss modulus.

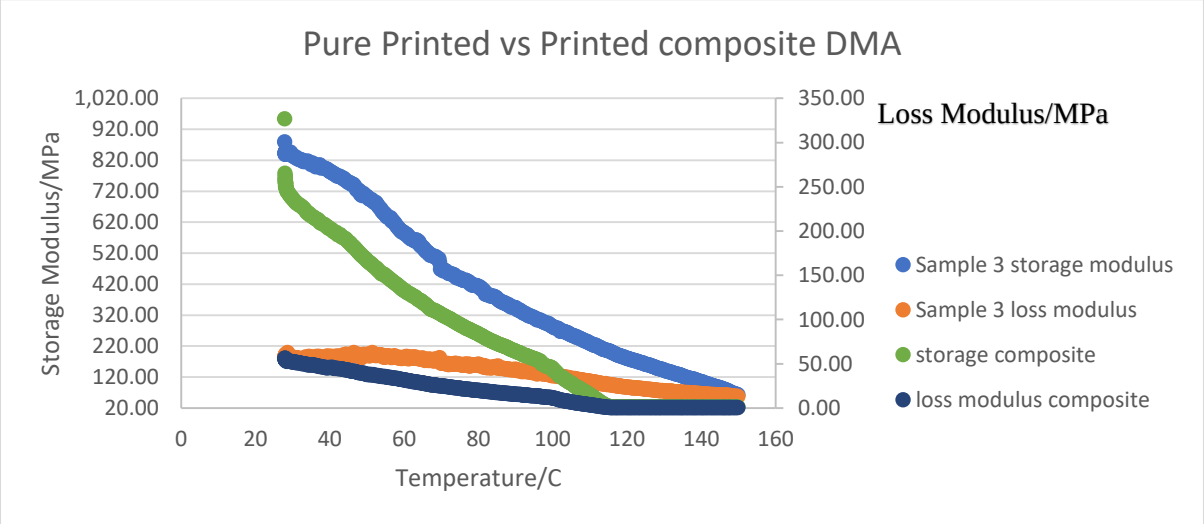

Figure 4.12 : DMA graph of the pure and composite prints

4.4.7 FTIR Results

Although the FTIR spectroscopy was conducted for the solution casted formulations to optimize the β-phase content, it is now being used to characterize the printed composite in order to investigate the effect of fillers after 3D printing. Figure 4.13 displays the FTIR graphs

for both the pure polymer and the composite prints, which show a consistent trend. Using Equation 3.1, the β-phase content was calculated for eight samples with an average of 44.28%. Despite a slight increase in comparison to the β-phase content of the printed pure polymer (43.58%), the composite recorded a value lower than expected. There could be a couple of possible reasons why the β-phase was not enhanced further. Firstly, the printing temperature was not fully optimized due to the 3D printer's limitations. As previously discussed, the interaction plots showed that a parameter can cause a bigger change if the other parameters are optimized. Therefore, the β-phase may not have been enhanced further due to the non-optimized temperature, despite optimizing printing speed and layer thickness. Another possible reason could be the agglomeration of fillers in certain areas, preventing the nucleation of β-phase in several places along the film.

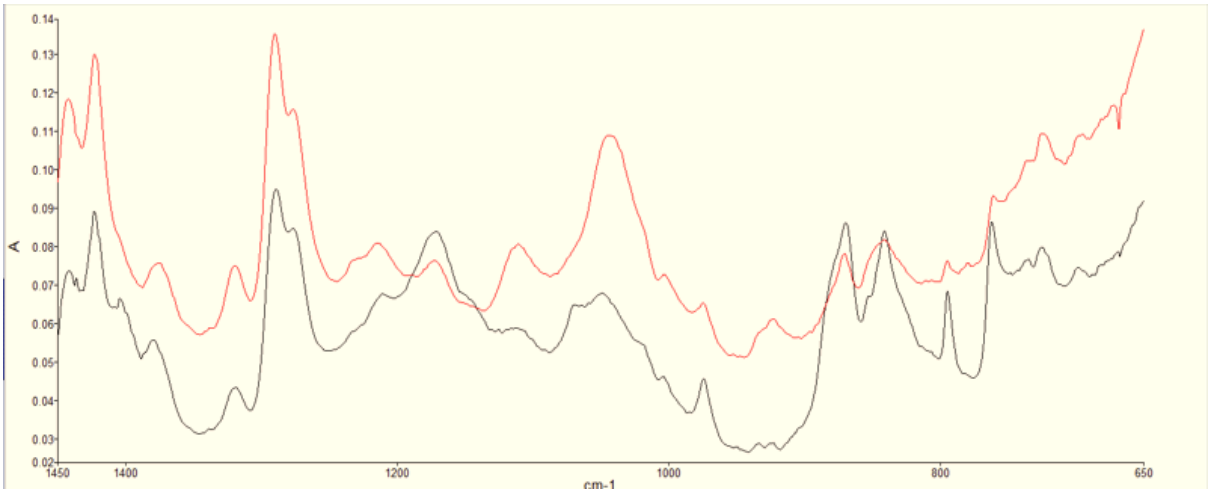

Figure 4.13 : FTIR results of pure and composite printed samples (black line indicates the composite)

4.4.8 DSC Results

The Differential scanning calorimetry test was conducted on extruded filaments and 3D printed samples from both the copolymer and the composite to investigate the effect of the fillers and the 3D printing process on the thermal properties such as the melting point, crystallinity, and the possible phase changes present. The DSC thermogram is shown in Figure 4.14. The separate thermograms are showcased in the appendix. Table 4.4 was created to highlight the important data extracted from the thermograms such as the melting point and the melting enthalpy which was used to calculate the degree of crystallinity of the samples using the formula :

$$X_C = \left(\frac{\Delta H_m}{\Delta H_m^{\Phi}}\right) x\, X_m\, x\, 100\%$$

Where X_c is the degree of crystallinity, ΔH_m is the melting enthalpy of the film, X_m is the weight fraction of PVDF in the composite, and ΔH^{Φ}_m is the melting enthalpy of 100% crystalline material, i.e., 104.5 J/g [252].

Initially, it was assumed that the incorporation of fillers in the polymer matrix will results in a material of a higher degree of crystallinity due to their action as nucleation agents. However, it can be seen that the crystallinity of the samples undergoes a reduction when the fillers are incorporated in the polymer matrix for either the filament or the 3D printed samples. Thoroughly, for the extruded filament samples, the composite recorded a 30.29% reduction when compared to the pure filament. The melting temperature peak also faced a slight decrease where the pure filament recorded 144.8C° while the composite filament recorded 142.5C°. The same trend was observed in the 3D printed samples where the composite sample recorded a 14% reduction when compared to the pure polymer. A possible reasoning for this behaviour is that the overdosed fillers in the polymer matrix acted as crystallization inhibitors by delaying or preventing the nucleation. The same phenomenon was observed before in literature in [233, 253].

Regarding the effect of FDM, the 3D printed samples exhibited a lower degree of crystallinity when compared to the extruded filament for the pure polymer or the composite. In detail, the 3D printed pure polymer recorded a 27.06% reduction compared to the pure filament sample, and the 3D printed composite recorded a 24.09% reduction to the composite filament, which displays that the 3D printing process resulted in a reduction in crystallinity. Jayswal and Adanur [254] also noticed the same phenomenon in their work on 3D printed PLA. The reason behind the reduction of crystallinity could be due to the high temperature difference between the nozzle and the printing bed, which allows for a very short time for crystallization.

Figure 4.14 : DSC analysis

Table 4.4 : Melting temperature and degree of crystallinity for different samples

Sample	**T_m (C°)**	**ΔH_m (J/g)**	**X_C (%)**
PVDF-HFP filament	144.8	22.55	21.57895
Composite filament	142.5	18.64	15.04221
3D Printed pure polymer	143.6	16.45	15.74163
3D Printed composite	141.8	14.15	11.41885

4.4.9 TGA results

The thermogravimetric analysis technique was performed to investigate the thermal stability of the samples. The instrument conducting the TGA test recorded the weight percentage of the samples as the temperature increased. The software provided data such as the initial degradation temperature and weight values for each corresponding temperature to assist in plotting the thermal decomposition of the samples and analysing the thermal decomposition of PVDF-HFP. Figure 4.15 illustrates the thermal decomposition of pure and composite PVDF-HFP polymer in filament and printed forms. To help understand the effects of filler incorporation and 3D printing process, Table 4.5 was created to list the initial degradation temperature, weight loss for each sample, and the weight loss percentage of the polymeric phase. Since BTO is thermally stable and does not undergo any thermal degradation under the same temperature range as confirmed by Fu, et al. [255], another metric other than the weight loss needs to be implemented to evaluate the effect of fillers on the thermal stability. Therefore, the weight loss percentage of the polymeric phase can be evaluated by dividing the weight loss of the sample by the weight fraction of PVDF-HFP in the sample.

As Table 4.5 shows, the pure PVDF-HFP filament recorded the lowest initial degradation temperature with 438.63C° while the composite filament recorded the highest temperature with 461.16C°. A possible reasoning to the improvement of the initial decomposition temperature is that the incorporation of fillers resulted in further crystallization of β-phase crystals, which have a higher melting point compared to the α-phase crystals [256, 257].

Table 4.5 also conveyed a higher weight loss in PVDF-HFP for the composite samples when compared to the pure samples from either the filament or the 3D printed where the pure filament recorded the highest PVDF-HFP weight loss with 80.86% and the printed pure sample recorded the lowest with 59.8%. This reduced thermal stability could be due to the agglomeration of fillers observed in the FESEM results which may act as a stress concentration point making the composite more susceptible to thermal degradation [258].

It can also be seen that the printed samples recorded a lower weight loss value when compared to the pure filament, which could be an indication that the FDM process resulted in a more thermally stable samples. A similar explanation regarding the improvement of the β-phase fraction in the polymer due to the 3D printing process can be used in this case.

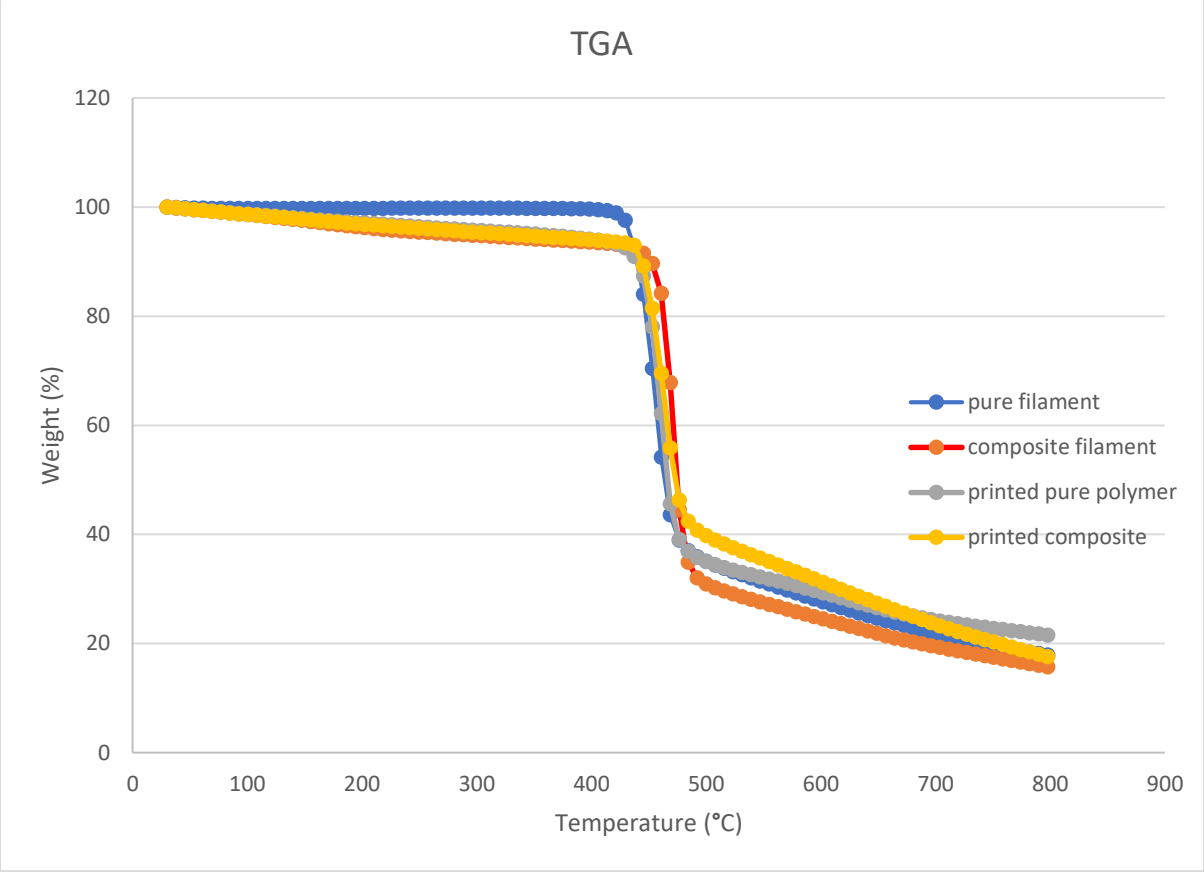

Figure 4.15 : TGA results

Table 4.5 : : List of the initial degradation temperature and weight loss for all samples

Sample	Initial Degradation temperature (°C)	Weight loss (%)	Weight loss in PVDF-HFP (%)
PVDF-HFP filament	438.63	70.4	70.4
Composite filament	461.16	68.19	80.86
3D Printed pure polymer	450.26	59.8	59.8
3D Printed composite	448.24	58.73	69.64

4.4.10 Electromechanical test results

The purpose of the study was to confirm the piezoelectricity of the fabricated samples using an electromechanical test. The voltage response of the samples was measured when a force was exerted on them. This allowed for the quantification of the sensitivity of each sample, as well as the voltage coefficient, which can be used to compare piezoelectric performance without considering geometrical differences. Table 4.6 lists the average force sensitivity and the calculated piezoelectric voltage coefficient for all samples.

First of all, the electromechanical test confirmed the piezoelectricity of the fabricated samples. Moreover, the results showed that the solution-casted sample had the highest sensitivity, with an average value of 4.09 mV/N. The pure printed sample had a sensitivity of 2.64 mV/N, while the printed composite sample had the lowest sensitivity, with a value of 1.34 mV/N. The following trend was expected since the solution-casted sample had a higher β-phase content. However, the results for the printed pure and composite samples did not match the expectations, as the composite sample had a slightly higher β-phase content but a lower voltage response was recorded. This could be due to the lower crystallinity of the printed composite sample, which is consistent with a computational model of the piezoelectric effect of PVDF [259]. The model suggests that only the crystalline regions of PVDF are responsible for any observed piezoelectricity[260]. A similar trend was observed in the work by Wu, et al. [245], where the sample with the higher β-phase recorded a lower voltage response, possibly due to the reduction in its crystallinity.

As known, a limitation of the study is that the samples did not undergo the poling process, which is known to enhance the piezoelectric performance of a sample. Thus, the piezoelectric voltage coefficient $g33$ values for the samples were much lower than those reported in the literature for PVDF (200mV.m/N) [261]. However, the $g33$ values followed the same trend as the sensitivity values, with the solution-casted sample having the highest value and the printed composite sample having the lowest value. The samples fell short when their $g33$ was compared to other material such as PZT and Quartz which recorded $g33$ values of 18.5mv.m/N and 50mV.m/N, respectively [261].

Table 4.6 : Electromechanical Test results

Sample	Force Sensitivity/ (mV/N)	Piezoelectric Voltage Coefficient, g_{33}/ (mV.m/N)
3D printed pure polymer	2.638896682	1.484379
3D printed composite	1.340511474	0.754038
Optimal solution casted	4.085464316	2.298074

4.5 Conclusions

In this chapter, the conventional techniques used to enhance the piezoelectricity of PVDF-HFP are discussed, with the reinforcement technique being selected. Barium Titanate (BTO) and Untreated Activated Carbon (UAC) were chosen as potential fillers to be incorporated in the polymer matrix, and DMSO was selected as the solvent to investigate its viability as an alternative friendly solvent. The optimum mixture Design of experiments (MDOE) method was used to optimize the formulation and understand the effects of the fillers on the β-phase content.

The initial analysis showed that DMSO was a viable alternative solvent, as it recorded similar β-phase values to other solvents for similar formulations in literature. As the MDOE was carried forward, it was deduced that Barium Titanate positively influenced the matrix unlike untreated activated carbon. The software suggested an optimal formulation of 84.21 wt.% PVDF-HFP, 15.00 wt.% BTO, and 0.79 wt.% UAC was fabricated, which recorded a β-phase content of 71.895% with a relative error of 0.85% from the predicted value.

After printing the optimized composite, several characterization techniques were performed. The FESEM analysis showed that the filler content in the matrix correlated with the amount of pores and agglomerates in the matrix. It was also reported that the 3D printed samples lacked the spherulitic pattern shown in the solution casted samples. The effect of the voids and

microcracks discovered in the FESEM images was highlighted when the DMA results reported that the printed composite recorded a smaller storage modulus when compared to the printed polymer. Additionally, the β-phase content of the printed composite was slightly higher than that of the pure polymer, but the printed polymer recorded a higher voltage response, which could be attributed to the lower crystallinity of the printed composite confirmed by DSC thermograms. In conclusion, the fabricated samples exhibited piezoelectricity and were able to detect forces in the 1N range.

5. Conclusions and Future works

The exquisite mechanical properties and commendable piezoelectric characteristics of polyvinyldene fluoride (PVDF) and its copolymers have kindled considerable interest in their application as piezoelectric materials. These materials have found extensive use in the fabrication of flexible force sensors, which have garnered significant demand across various industries. However, the use of hazardous and toxic solvents in the mixing process has raised concerns over their safety and ecological impact. Hence, the search for alternative fabrication techniques has become essential.

This study explored the use of fused deposition modeling (FDM) to 3D print PVDF copolymer composites with the aim of investigating the effect of printing parameters on the piezoelectric and mechanical properties of the samples. The copolymer PVDF-HFP was 3D printed, and a DOE analysis was conducted to investigate the effect of printing parameters such as printing temperature, printing speed, and layer thickness on the β-phase content in printed samples. The analysis revealed that all printing parameters significantly influenced the β-phase content in printed samples, and an interaction was observed between the printing parameters. It was discovered that the effect of a certain parameter is maximised when the other paramters are optimized. The following deductions were utilized by the software to predict the optimized printing paramters which are as follows: printing temperature of 250C°, printing speed of 10mm/s, and a layer thickness of 0.1mm.

Furthermore, this study investigated the use of fillers to enhance the piezoelectricity of PVDF-HFP, with Barium Titanate and Untreated Activated Carbon being chosen as the fillers. As an alternative solvent, the viability of using DMSO was investigated. The optimum mixture design of experiments (MDOE) method was used to optimize the formulation and understand the effects of the fillers on the β-phase content. The results of the MDOE analysis showed that Barium Titanate positively influenced the matrix, unlike untreated activated carbon, and DMSO was a viable alternative solvent. With a desirability of 0.96, a formulation of 84.21 wt.% PVDF-HFP, 15.00 wt.% BTO, and 0.79 wt.% UAC was deemed optimal by the software with a β-phase content prediction of 72.504%. The fabricated sample recorded 71.895% with a relative error of 0.85%.

Following the printing of the composite material that had undergone optimization, various techniques for characterization were carried out, such as FESEM and DMA analyses. The FESEM analysis revealed that the quantity of filler content present in the matrix was directly associated with the amount of pores and agglomerates in the matrix. Additionally, it was noted that the 3D printed samples exhibited no spherulitic pattern as observed in the solution-cast samples. The DMA results showed that the presence of voids and microcracks, identified through the FESEM images, had an impact as the printed composite demonstrated a smaller storage modulus than the printed polymer.

Despite recording a slightly higher β-phase content, the printed composite recorded a lower force sensitivity when compared to the pure polymer. The reason behind the relatively poor piezoelectric performance was the low crystallinity which was captured by the DSC thermogram. . It is also worth noting that poling samples would have ensured a higher voltage response in the composite despite the lower crystallinity due to poling process activating the piezoelectricity in the Barium Titanate incorporated in the filler. Despite its performance, all printed samples exhibited piezoelectricity and were able to detect forces in the 1N range. This finding demonstrates the potential of FDM-printed PVDF copolymer composites as flexible force sensors.

As for future work, several areas could be explored. First, the effect of post-processing techniques such as annealing and poling on the piezoelectric properties of the printed samples could be studied. Annealing and poling have been reported to enhance the piezoelectricity of PVDF and its copolymers, and could potentially improve the performance of the printed composite.

Second, the printing parameters for the composite could be optimized to improve the mechanical and piezoelectric properties. In this study, the printing parameters for the composite were not optimized due to the printer constraints. Finally, a novel approach to reducing the agglomerates in the solution casted samples could be developed. The FESEM analysis showed that the filler content in the matrix correlated with the amount of pores and agglomerates in the matrix. A novel approach to reducing agglomerates could potentially improve the performance of the composite.

In summary, this study provides a foundation for further research into the fabrication and optimization of PVDF-HFP composites for use as flexible force sensors. Future work in this area could lead to the development of more efficient and reliable piezoelectric materials for a variety of applications.

References

[1] Y.-W. Chen, P. P. Pancham, A. Mukherjee, E. Martincic, and C.-Y. Lo, "Recent advances in flexible force sensors and their applications: A review," *Flexible and Printed Electronics,* 2022.

[2] S. Kulinyi *et al.*, "Flexible packaging for tyre integrated shear force sensor," in *SENSORS, 2012 IEEE*, 28-31 Oct. 2012 2012, pp. 1-4, doi: 10.1109/ICSENS.2012.6411326.

[3] L. Ren, K. Yu, and Y. Tan, "Wireless and passive magnetoelastic-based sensor for force monitoring of artificial bone," *IEEE Sensors Journal,* vol. 19, no. 6, pp. 2096-2104, 2018.

[4] C. G. Núñez, W. T. Navaraj, E. O. Polat, and R. Dahiya, "Energy-autonomous, flexible, and transparent tactile skin," *Advanced Functional Materials,* vol. 27, no. 18, p. 1606287, 2017.

[5] D. Sengupta, J. Romano, and A. G. P. Kottapalli, "Electrospun bundled carbon nanofibers for skin-inspired tactile sensing, proprioception and gesture tracking applications," *npj Flexible Electronics,* vol. 5, no. 1, p. 29, 2021.

[6] F. Xu *et al.*, "Recent developments for flexible pressure sensors: A review," *Micromachines,* vol. 9, no. 11, p. 580, 2018.

[7] Avnet Abacus. https://www.avnet.com/wps/portal/abacus/solutions/technologies/sensors/pressure-sensors/core-technologies/capacitive-vs-piezoresistive-vs-piezoelectric/ (accessed 22 May, 2021).

[8] D. Sparks, "4 - MEMS pressure and flow sensors for automotive engine management and aerospace applications," in *MEMS for Automotive and Aerospace Applications*, M. Kraft and N. M. White Eds.: Woodhead Publishing, 2013, pp. 78-105.

[9] Avnet Abacus. https://www.avnet.com/wps/portal/abacus/solutions/technologies/sensors/pressure-sensors/core-technologies/piezoresistive-strain-gauge/ (accessed 23 May, 2021).

[10] Avnet Abacus. https://www.avnet.com/wps/portal/abacus/solutions/technologies/sensors/pressure-sensors/core-technologies/piezoelectric/ (accessed 24 april 2021).

[11] M. Kim and J. Fan, "Piezoelectric Properties of Three Types of PVDF and ZnO Nanofibrous Composites," *Advanced Fiber Materials,* vol. 3, no. 3, pp. 160-171, 2021/06/01 2021, doi: 10.1007/s42765-021-00068-w.

[12] I. Y. Abdullah, M. Yahaya, M. H. H. J. Jumali, and H. M. Shanshool, "Enhancement piezoelectricity in poly(vinylidene fluoride) by filler piezoceramics lead-free potassium sodium niobate (KNN)," *Optical and Quantum Electronics,* vol. 48, no. 2, p. 149, 2016/01/29 2016, doi: 10.1007/s11082-016-0433-1.

[13] A. Figoli *et al.*, "Towards non-toxic solvents for membrane preparation: a review," *Green Chemistry,* 10.1039/C4GC00613E vol. 16, no. 9, pp. 4034-4059, 2014, doi: 10.1039/C4GC00613E.

[14] K. Mustapha, K. M. Metwalli, and Y. Abakr, "3D printing of polyvinylidene fluoride composite films with enhanced electroactive beta-phase for flexible wearable pressure sensors," *Materials Today: Proceedings,* vol. 70, pp. 321-327, 2022.

[15] H. Kim, T. Fernando, M. Li, Y. Lin, and T.-L. B. Tseng, "Fabrication and characterization of 3D printed BaTiO3/PVDF nanocomposites," *Journal of Composite Materials,* vol. 52, no. 2, pp. 197-206, 2018/01/01 2017, doi: 10.1177/0021998317704709.

[16] J. Curie and P. Curie, "Phénomènes électriques des cristaux hémièdres à faces inclinées," *Journal de Physique theorique et appliquee,* vol. 1, no. 1, pp. 245-251, 1882.

[17] G. Lippmann, "Principe de la conservation de l'électricité, ou second principe de la théorie des phénomènes électriques," *Journal de Physique Théorique et Appliquée,* vol. 10, no. 1, pp. 381-394, 1881, doi: 10.1051/jphystap:0188100100038100.
[18] B. Jaffe, W. R. C. Jr., and H. Jaffe, *Piezoelectric Ceramics*. Academic Press Inc., 1971.
[19] B. Jaffe, R. S. Roth, and S. Marzullo, "Piezoelectric Properties of Lead Zirconate-Lead Titanate Solid-Solution Ceramics," *Journal of Applied Physics,* vol. 25, no. 6, pp. 809-810, 1954, doi: 10.1063/1.1721741.
[20] H. Kawai, "The Piezoelectricity of Poly (vinylidene Fluoride)," *Japanese Journal of Applied Physics,* vol. 8, no. 975, 1969, doi: https://doi.org/10.1143/JJAP.8.975.
[21] D. S. Antonio Arnau, A. A. Vives, Ed. *Transducers and Applications* 2nd ed. Springer-Verlag Berlin Heidelberg, 2008.
[22] E. Carvalho, L. Fernandes, C. M. Costa, and S. Lanceros-Méndez, "Piezoelectric polymer composites for sensors and actuators," Elsevier, 2020.
[23] Sunghwan Kim, "'Low power energy harvesting with piezoelectric generators," PhD, Dept. of Mechanical and Material Science, University of Pittsburgh, 2002.
[24] *Publication and Proposed Revision*

of ANSUIEEE Standard 176-1987

"ANSUIEEE Standard on Piezoelectricity" 1996.
[25] D. J. Leo, *Engineering analysis of smart material systems*. Hoboken, N.J: John Wiley & Sons, 2007.
[26] M. J. Ramsay and W. W. Clark, "Piezoelectric energy harvesting for bio-MEMS applications," *Smart Structures and Materials 2001: Industrial and Commercial Applications of Smart Structures Technologies,* vol. 4332, 2001, doi: 10.1117/12.429684.
[27] Z. Yang *et al.*, "Recent Advances in Self-Powered Piezoelectric and Triboelectric Sensors: From Material and Structure Design to Frontier Applications of Artificial Intelligence," (in eng), *Sensors (Basel),* vol. 21, no. 24, Dec 17 2021, doi: 10.3390/s21248422.
[28] P. Regtien and E. Dertien, "8 - Piezoelectric sensors," in *Sensors for Mechatronics (Second Edition)*, P. Regtien and E. Dertien Eds.: Elsevier, 2018, pp. 245-265.
[29] Z. Chen *et al.*, "Flexible Piezoelectric-Induced Pressure Sensors for Static Measurements Based on Nanowires/Graphene Heterostructures," *ACS Nano,* vol. 11, no. 5, pp. 4507-4513, May 23 2017, doi: 10.1021/acsnano.6b08027.
[30] L. Elkarous, C. Robbe, M. Pirlot, and J.-C. Golinval, "Dynamic calibration of piezoelectric transducers for ballistic high-pressure measurement," *International Journal of Metrology and Quality Engineering,* vol. 7, no. 2, 2016, doi: 10.1051/ijmqe/2016004.
[31] J. Meng, W. Xie, M. Brennan, K. Runge, and D. Bradshaw, "Measuring turbulence in a flotation cell using the piezoelectric sensor," *Minerals Engineering,* vol. 66-68, pp. 84-93, 2014, doi: 10.1016/j.mineng.2014.06.007.
[32] Kadco ceramics. https://www.kadcoceramics.com/blog/piezoelectric-crystal/ (accessed 4-May, 2021).
[33] I. David. "How Do Piezoelectric Crystals Work? ." https://sciencing.com/do-piezoelectric-crystals-work-5132808.html (accessed 4-May, 2021).
[34] Q. Zhou, K. H. Lam, H. Zheng, W. Qiu, and K. K. Shung, "Piezoelectric single crystals for ultrasonic transducers in biomedical applications," *Prog Mater Sci,* vol. 66, pp. 87-111, Oct 1 2014, doi: 10.1016/j.pmatsci.2014.06.001.
[35] F. Chen, "Photonic guiding structures in lithium niobate crystals produced by energetic ion beams," *Journal of Applied Physics,* vol. 106, no. 8, p. 081101, 2009, doi: 10.1063/1.3216517.
[36] H. Gnewuch, N. K. Zayer, C. N. Pannell, G. W. Ross, and P. G. R. Smith, "Broadband monolithic acousto-optic tunable filter," *Opt. Lett.,* vol. 25, no. 5, pp. 305-307, 2000/03/01 2000, doi: 10.1364/OL.25.000305.

[37] F. Tian, Y. Liu, R. Ma, F. Li, Z. Xu, and Y. Yang, "Properties of PMN-PT single crystal piezoelectric material and its application in underwater acoustic transducer," *Applied Acoustics,* vol. 175, p. 107827, 2021/04/01/ 2021, doi: https://doi.org/10.1016/j.apacoust.2020.107827.
[38] K. A. Snook *et al.*, "Design, fabrication, and evaluation of high frequency, single-element transducers incorporating different materials," *IEEE Transactions on Ultrasonics, Ferroelectrics, and Frequency Control,* vol. 49, no. 2, pp. 169-176, 2002, doi: 10.1109/58.985701.
[39] F. Li *et al.*, "Piezoelectric activity in Perovskite ferroelectric crystals," *IEEE Transactions on Ultrasonics, Ferroelectrics, and Frequency Control,* vol. 62, no. 1, pp. 18-32, 2015, doi: 10.1109/TUFFC.2014.006660.
[40] H. Ohsato, "Origin of Piezoelectricity on Langasite," 2012.
[41] http://lampx.tugraz.at/~hadley/ss2/crystalphysics/piezo.php (accessed 4-May, 2021).
[42] "Piezoelectricity." https://eng.libretexts.org/@go/page/322 (accessed 23 August, 2021).
[43] S. Trolier-McKinstry, "Crystal Chemistry of Piezoelectric Materials," in *Piezoelectric and Acoustic Materials for Transducer Applications*, A. Safari and E. K. Akdoğan Eds. Boston, MA: Springer US, 2008, pp. 39-56.
[44] J. S. Harrison and Z. Ounaies, "Piezoelectric Polymers," *NASA/CR-2001-211422,* 2001.
[45] W. Heywang, K. Lubitz, and W. Wersing, "Piezoelectric Polymers and Their Applications," in *Piezoelectricity: Evolution and Future of a*

Technology.

: Springer Berlin Heidelberg, 2008.
[46] T. Hattori, Y. Takahashi, M. Iijima, and E. Fukada, "Piezoelectric and ferroelectric properties of polyurea-5 thin films prepared by vapor deposition polymerization," *Journal of Applied Physics,* vol. 79, no. 3, pp. 1713-1721, 1996/02/01 1996, doi: 10.1063/1.360959.
[47] Y. Tajitsu *et al.*, "Ferroelectric Behavior in Thin Films of Polyurea-5," *Japanese Journal of Applied Physics,* vol. 35, no. Part 1, No. 9B, pp. 5199-5202, 1996/09/30 1996, doi: 10.1143/jjap.35.5199.
[48] G. Wu, O. Yano, and T. Soen, "Dielectric and Piezoelectric Properties of Nylon 9 and Nylon 11," *Polymer Journal,* vol. 18, no. 1, pp. 51-61, 1986/01/01 1986, doi: 10.1295/polymj.18.51.
[49] B. A. Newman, P. Chen, K. D. Pae, and J. I. Scheinbeim, "Piezoelectricity in nylon 11," *Journal of Applied Physics,* vol. 51, no. 10, pp. 5161-5164, 1980/10/01 1980, doi: 10.1063/1.327283.
[50] E. Fukada, *Recent Developments of Piezoelectric Polymers - Polyurea, Odd-Nylon, Vinylidenecyanide Copolymer, and Polylactic Acid*. 2005, pp. 106-112.
[51] F. Bernard, L. Gimeno, B. Viala, B. Gusarov, and O. Cugat, "Direct Piezoelectric Coefficient Measurements of PVDF and PLLA under Controlled Strain and Stress," *Proceedings,* vol. 1, no. 4, p. 335, 2017. [Online]. Available: https://www.mdpi.com/2504-3900/1/4/335.
[52] T. Ochiai and E. Fukada, "Electromechanical Properties of Poly-L-Lactic Acid," *Japanese Journal of Applied Physics,* vol. 37, no. Part 1, No. 6A, pp. 3374-3376, 1998/06/15 1998, doi: 10.1143/jjap.37.3374.
[53] B. Gonzalo *et al.*, "Dielectric Properties of Piezoelectric Polyimides," *Ferroelectrics,* vol. 370, no. 1, pp. 3-10, 2008/10/21 2008, doi: 10.1080/00150190802380227.
[54] S. Tasaka, N. Inagaki, T. Okutani, and S. Miyata, "Structure and properties of amorphous piezoelectric vinylidene cyanide copolymers," *Polymer,* vol. 30, no. 9, pp. 1639-1642, 1989/09/01/ 1989, doi: https://doi.org/10.1016/0032-3861(89)90323-6.
[55] K. Tashiro, H. Tadokoro, and M. Kobayashi, "Structure and piezoelectricity of poly (vinylidene fluoride)," *Ferroelectrics,* vol. 32, no. 1, pp. 167-175, 1981.
[56] S. Tasaka, J. Niki, T. Ojio, and S. Miyata, "Structure and Piezoelectricity of Poly (vinylidene fluoride) Films Obtained by Solid-State Extrusion," *Polymer journal,* vol. 16, no. 1, pp. 41-48, 1984.

[57] L. Ruan, X. Yao, Y. Chang, L. Zhou, G. Qin, and X. Zhang, "Properties and applications of the β phase poly (vinylidene fluoride)," *Polymers,* vol. 10, no. 3, p. 228, 2018.
[58] T. J. Fleck, T. D. Manship, S. F. Son, and J. F. Rhoads, "The Effect of Process Parameters on the Structural Energetic Properties of Additively Manufactured Reactive Structures," *Journal of Engineering Materials and Technology,* vol. 142, no. 4, 2020.
[59] J. Sirohi and I. Chopra, "Fundamental understanding of piezoelectric strain sensors," *Journal of intelligent material systems and structures,* vol. 11, no. 4, pp. 246-257, 2000.
[60] P. Martins, A. Lopes, and S. Lanceros-Mendez, "Electroactive phases of poly (vinylidene fluoride): Determination, processing and applications," *Progress in polymer science,* vol. 39, no. 4, pp. 683-706, 2014.
[61] R. H. Upadhyay and R. R. Deshmukh, "Investigation of dielectric properties of newly prepared β-phase polyvinylidene fluoride–barium titanate nanocomposite films," *Journal of Electrostatics,* vol. 71, no. 5, pp. 945-950, 2013/10/01/ 2013, doi: https://doi.org/10.1016/j.elstat.2013.08.004.
[62] V. T. Rathod, D. R. Mahapatra, A. Jain, and A. Gayathri, "Characterization of a large-area PVDF thin film for electro-mechanical and ultrasonic sensing applications," *Sensors and Actuators A: Physical,* vol. 163, no. 1, pp. 164-171, 2010/09/01/ 2010, doi: https://doi.org/10.1016/j.sna.2010.08.017.
[63] V. Cardoso, G. Minas, C. M. Costa, C. Tavares, and S. Lanceros-Mendez, "Micro and nanofilms of poly (vinylidene fluoride) with controlled thickness, morphology and electroactive crystalline phase for sensor and actuator applications," *Smart Materials and Structures,* vol. 20, no. 8, p. 087002, 2011.
[64] I. Y. Abdullah, M. H. H. Jumali, M. Yahaya, and H. M. Shanshool, "Facile formation of [beta] poly (vinylidene fluoride) films using the short time annealing process," *Advances in Environmental Biology,* vol. 9, no. 20 S1, pp. 20-28, 2015.
[65] R. G. Kepler and R. A. Anderson, "Ferroelectric polymers," *Advances in Physics,* vol. 41, no. 1, pp. 1-57, 1992, doi: 10.1080/00018739200101463.
[66] ANDREW J. LOVINGER, "Poly(vinylidene fluoride)," in *DEVELOPMENTS IN*

CRYSTALLINE

POLYMER-1, D. C. Bassett Ed. London: Applied Science, 1982, p. 195.
[67] Z. Ounaies, J. A. Young, and J. S. Harrison, "Design Requirements for Amorphous Piezoelectric Polymers.," *NASA/TM-1999-209359,* 1999.
[68] M. G. Broadhurst and G. T. Davis, "Piezo- and pyroelectric properties," in *Electrets. Topics in Applied Physics*, vol. 33, Sessler G.M. Ed.: Springer, Berlin, Heidelberg, 1980.
[69] C. Park, Z. Ounaies, K. E. Wise, and J. S. Harrison, "In situ poling and imidization of amorphous piezoelectric polyimides," *Polymer,* vol. 45, no. 16, pp. 5417-5425, 2004/07/21/ 2004, doi: https://doi.org/10.1016/j.polymer.2004.05.057.
[70] Schneider G.A., "fracture of piezoceramics," in *Encyclopedia of materials: Science and technology*, K.H.J. Buschow *et al.* Eds., 1st ed. Oxford: Elsevier, 2001, pp. 3319-3321.
[71] J. A. Gallego-Juarez, "Piezoelectric ceramics and ultrasonic transducers," *Journal of Physics E: Scientific Instruments,* vol. 22, no. 10, pp. 804-816, 1989/10 1989, doi: 10.1088/0022-3735/22/10/001.
[72] S. Dwivedi, T. Pareek, and S. Kumar, "Structure, dielectric, and piezoelectric properties of K0.5Na0.5NbO3-based lead-free ceramics," *RSC Advances,* 10.1039/C8RA04038A vol. 8, no. 43, pp. 24286-24296, 2018, doi: 10.1039/C8RA04038A.
[73] Y. Guo, K.-i. Kakimoto, and H. Ohsato, "(Na0.5K0.5)NbO3–LiTaO3 lead-free piezoelectric ceramics," *Materials Letters,* vol. 59, no. 2, pp. 241-244, 2005/02/01/ 2005, doi: https://doi.org/10.1016/j.matlet.2004.07.057.
[74] M. A. Fraga, H. Furlan, R. S. Pessoa, and M. Massi, "Wide bandgap semiconductor thin films for piezoelectric and piezoresistive MEMS sensors applied at high temperatures: an

overview," *Microsystem Technologies,* vol. 20, no. 1, pp. 9-21, 2014/01/01 2014, doi: 10.1007/s00542-013-2029-z.
[75] T.L. Jordan and Z. Ounaies, "Piezoelectric Ceramics Characterization," *NASA/CR-2001-211225,* 2001.
[76] W.G. Cady, *An introduction to the theory and applications of electromechanical phenomena in crystals*. New York, NY: Dover Publications, 1964.
[77] Xinhua Zhu, "Piezoelectric ceramic materials: Processing, properties, characterization, and applications," *Piezoelectric Materials: Structure, Properties and Applications.,* pp. 1-36, 2010.
[78] Wolfram Notebook. https://www.wolframcloud.com/objects/demonstrations/PiezoelectricityInBariumTitanate-source.nb (accessed 2 May, 2021).
[79] R.B. Gray, "U.S. Patent 2,486,560,

," 1946.
[80] K. Uchino, "The Development of Piezoelectric Materials and the New Perspective," in *Advanced Piezoelectric Materials*, 2017, pp. 1-92.
[81] Leslie Eric Cross, "Ferroelectric materials for electromechanical transducer applications," *Materials Chemistry and Physics*

vol. 43, no. 2, pp. 108-115

1996, doi: https://doi.org/10.1016/0254-0584(95)01617-4.
[82] A.Amin, R.E.Newnham, L.E.Cross, and D.E.Cox, "Phenomenological and structural study of a low-temperature phase transition in the PbZrO3・PbTiO3 system," *Journal of Solid State Chemistry*

vol. 37, no. 2, pp. 248-255

1981, doi: https://doi.org/10.1016/0022-4596(81)90091-8.
[83] A. Wu, P. M. Vilarinho, V. V. Shvartsman, G. Suchaneck, and A. L. Kholkin, "Domain populations in lead zirconate titanate thin films of different compositions via piezoresponse force microscopy," *Nanotechnology,* vol. 16, no. 11, pp. 2587-2595, 2005, doi: 10.1088/0957-4484/16/11/020.
[84] J. Rödel, K. G. Webber, R. Dittmer, W. Jo, M. Kimura, and D. Damjanovic, "Transferring lead-free piezoelectric ceramics into application," *Journal of the European Ceramic Society,* vol. 35, no. 6, pp. 1659-1681, 2015, doi: 10.1016/j.jeurceramsoc.2014.12.013.
[85] Y. Saito *et al.*, "Lead-free piezoceramics. ," *Nature,* vol. 432, no. 7013, pp. 84-87, Nov 4 2004, doi: 10.1038/nature03008.
[86] X. Gao *et al.*, "The mechanism for the enhanced piezoelectricity in multi-elements doped (K,Na)NbO3 ceramics," *Nat Commun,* vol. 12, no. 1, p. 881, Feb 9 2021, doi: 10.1038/s41467-021-21202-7.
[87] R. M. Guedes, "Micromechanics modeling of

hysteretic responses of

piezoelectric composites," in *Creep and Fatigue in Polymer Matrix Composites (Second Edition)*, R. M. Guedes Ed.: Woodhead Publishing, 2019, pp. 121-124.
[88] P. Eltouby, I. Shyha, C. Li, and J. Khaliq, "Factors affecting the piezoelectric performance of ceramic-polymer composites: A comprehensive review," *Ceramics International,* 2021/03/17/ 2021, doi: https://doi.org/10.1016/j.ceramint.2021.03.126.
[89] H. Kim *et al.*, "Increased piezoelectric response in functional nanocomposites through multiwall carbon nanotube interface and fused-deposition modeling three-dimensional printing@ CORRIGENDUM," *MRS Communications,* vol. 7, pp. 960-966, 2017.

[90] J. A. Krishnaswamy, F. C. Buroni, E. García-Macías, R. Melnik, L. Rodriguez-Tembleque, and A. Saez, "Design of lead-free PVDF/CNT/BaTiO3 piezocomposites for sensing and energy harvesting: the role of polycrystallinity, nanoadditives, and anisotropy," *Smart Materials and Structures,* vol. 29, no. 1, p. 015021, 2019/11/29 2019, doi: 10.1088/1361-665x/ab547d.

[91] E. Lemaire, R. Moser, C. J. Borsa, and D. Briand, "Green paper-based piezoelectronics for sensors and actuators," *Sensors and Actuators A: Physical,* vol. 244, pp. 285-291, 2016/06/15/ 2016, doi: https://doi.org/10.1016/j.sna.2016.04.024.

[92] E. Lemaire, D. Thuau, M. Souêtre, L. Zgainski, A. Royet, and A. Atli, "Revisiting two piezoelectric salts within an eco-design paradigm for sensors and actuators applications," *Sensors and Actuators A: Physical,* vol. 318, p. 112483, 2021/02/01/ 2021, doi: https://doi.org/10.1016/j.sna.2020.112483.

[93] P. Martins and S. Lanceros-Méndez, "Polymer-Based Magnetoelectric Materials," *Advanced Functional Materials,* https://doi.org/10.1002/adfm.201202780 vol. 23, no. 27, pp. 3371-3385, 2013/07/19 2013, doi: https://doi.org/10.1002/adfm.201202780.

[94] P. Martins, Y. V. Kolen'ko, J. Rivas, and S. Lanceros-Méndez, "Tailored Magnetic and Magnetoelectric Responses of Polymer-Based Composites," *ACS applied materials & interfaces,* vol. 7, 06/25 2015, doi: 10.1021/acsami.5b04102.

[95] Y. J. Choi, M.-J. Yoo, H.-W. Kang, H.-G. Lee, S. H. Han, and S. Nahm, "Dielectric and piezoelectric properties of ceramic-polymer composites with 0–3 connectivity type," *Journal of Electroceramics,* vol. 30, no. 1, pp. 30-35, 2013/04/01 2013, doi: 10.1007/s10832-012-9706-7.

[96] A. Safari, "Development of piezoelectric composites for transducers," *J. Phys. III France,* vol. 4, no. 7, pp. 1129-1149, 1994. [Online]. Available: https://doi.org/10.1051/jp3:1994191.

[97] W. D.-W. ZHANG De-Qing, YUAN Jie, ZHAO Quan-Liang, WANG Zhi-Ying, CAO Mao-Sheng, "Structural and Electrical Properties of PZT/PVDF Piezoelectric Nanocomposites Prepared by Cold-Press and Hot-Press Routes," *Chin. Phys. Lett.,* no. 12, pp. 4410-4413%V 25, 2008-11-27 2008. [Online]. Available: {http://cpl.iphy.ac.cn/CN/abstract/article_42479.shtml}.

[98] E. Venkatragavaraj, B. Satish, P. R. Vinod, and M. S. Vijaya, "Piezoelectric properties of ferroelectric PZT-polymer composites," *Journal of Physics D: Applied Physics,,* vol. 34, 2001, doi: 10.1088/0022-3727/34/4/308.

[99] K. Arlt and M. Wegener, "Piezoelectric PZT / PVDF-copolymer 0-3 composites: aspects on film preparation and electrical poling," *IEEE Transactions on Dielectrics and Electrical Insulation,* vol. 17, pp. 1178-1184, 2010, doi: 10.1109/tdei.2010.5539688.

[100] B. Satish, K. Sridevi, and M. S. Vijaya, "Study of piezoelectric and dielectric properties of ferroelectric PZT-polymer composites prepared by hot-press technique," *Journal of Physics D: Applied Physics,,* vol. 35, 2002, doi: 10.1088/0022-3727/35/16/321.

[101] K. S. Lam, Y. W. Wong, L. S. Tai, Y. M. Poon, and F. G. Shin, "Dielectric and pyroelectric properties of lead zirconate titanate/polyurethane composites," *Journal of Applied Physics,* vol. 96, no. 7, pp. 3896-3899, 2004/10/01 2004, doi: 10.1063/1.1787586.

[102] X. Kuang, Q. Gao, and H. Zhu, "Effect of calcination temperature of TiO2 on the crystallinity and the permittivity of PVDF-TrFE/TiO2 composites," *Journal of Applied Polymer Science,* https://doi.org/10.1002/app.38729 vol. 129, no. 1, pp. 296-300, 2013/07/05 2013, doi: https://doi.org/10.1002/app.38729.

[103] K. M. Rittenmyer, "Temperature dependence of the electromechanical properties of 0–3 PbTiO3-polymer piezoelectric composite materials," *The Journal of the Acoustical Society of America,* vol. 96, no. 1, pp. 307-318, 1994/07/01 1994, doi: 10.1121/1.410481.

[104] S. Huang, J. Chang, L. Lu, F. Liu, Z. Ye, and X. Cheng, "Preparation and polarization of 0–3 cement based piezoelectric composites," *Materials Research Bulletin,* vol. 41, no. 2, pp. 291-297, 2006/02/02/ 2006, doi: https://doi.org/10.1016/j.materresbull.2005.08.026.

[105] R. Senthilkumar, K. Sridevi, J. Venkatesan, V. Annamalai, and M. S. Vijaya, "Investigations on Ferroelectric PZT-PVDF Composites of 0–3 Connectivity," *Ferroelectrics,* vol. 325, no. 1, pp. 121-130, 2005/09/01 2005, doi: 10.1080/00150190500328544.
[106] P. Thongsanitgarn, A. Watcharapasorn, and S. Jiansirisomboon, "ELECTRICAL AND MECHANICAL PROPERTIES OF PZT/PVDF 0–3 COMPOSITES," *Surface Review and Letters,* vol. 17, no. 01, pp. 1-7, 2010/02/01 2010, doi: 10.1142/S0218625X10013540.
[107] L. Xiaofang, X. Chuanxi, S. Huajun, D. Lijie, L. Rui, and L. Yang, "Characterization of PZT/PVC composites added with carbon black," *Journal of Wuhan University of Technology-Mater. Sci. Ed.,* vol. 20, no. 4, pp. 60-64, 2005/12/01 2005, doi: 10.1007/BF02841284.
[108] B. Wei and Y. Daben, "Dielectric and piezoelectric properties of 0-3 composite film in PCM/PVDF and PZT/PVDF," *Ferroelectrics,* vol. 157, no. 1, pp. 427-430, 1994/07/01 1994, doi: 10.1080/00150199408229544.
[109] S. Sundaram, P.Sampathkumar, P. Gowdhaman, and V. Annamalai, "Dielectric and Piezoelectric Properties of Various Ferroelectric Ceramic-Polymer Composites," *Journal of Environmental Nanotechnology,* vol. 3, no. 3, pp. 27-31, 2014, doi: 10.13074/jent.2014.09.1412088.
[110] X.-T. Luo, L.-F. Chen, Q.-J. Huang, Q.-L. Wu, and Y.-P. Hong, "Preparation and properties of PVDF matrix piezoelectric composites containing highly aligned BaTiO3 whiskers," *Journal of Inorganic Materials,* vol. 19, no. 1, pp. 183-188, 2004.
[111] X. F. Liu, H. J. Sun, C. X. Xiong, C. Y. Zhang, H. Zheng, and M. Wei, "Effect of volume fraction and molding temperature on the electric properties of PZT/PVC composites," in *2009 18th IEEE International Symposium on the Applications of Ferroelectrics*, 23-27 Aug. 2009 2009, pp. 1-4, doi: 10.1109/ISAF.2009.5307545.
[112] Z. Wang and F. Narita, "Corona Poling Conditions for Barium Titanate/Epoxy Composites and their Unsteady Wind Energy Harvesting Potential," *Advanced Engineering Materials,* https://doi.org/10.1002/adem.201900169 vol. 21, no. 7, p. 1900169, 2019/07/01 2019, doi: https://doi.org/10.1002/adem.201900169.
[113] T. R. Gururaja, Q. C. Xu, A. R. Ramachandran, A. Halliyal, and R. E. Newnham, "Preparation and Piezoelectric Properties of Fired 0-3 Composites," in *IEEE 1986 Ultrasonics Symposium*, 17-19 Nov. 1986 1986, pp. 703-708, doi: 10.1109/ULTSYM.1986.198825.
[114] C. J. Dias and D. K. Das-Gupta, "Inorganic ceramic/polymer ferroelectric composite electrets," *IEEE Transactions on Dielectrics and Electrical Insulation,* vol. 3, no. 5, pp. 706-734, 1996, doi: 10.1109/94.544188.
[115] W. K. Sakamoto, S. Kagesawa, D. H. Kanda, and D. K. Das-Gupta, "Electrical properties of a composite of polyurethane and ferroelectric ceramics," *Journal of Materials Science,* vol. 33, no. 13, pp. 3325-3329, 1998/07/01 1998, doi: 10.1023/A:1013233329595.
[116] W. K. Sakamoto, S. Shibatta-Katesawa, D. H. F. Kanda, S. H. Fernandes, E. Longo, and G. O. Chierice, "Piezoelectric Effect in Composite Polyurethane–Ferroelectric Ceramics," *physica status solidi (a),* vol. 172, no. 1, pp. 265-271, 1999, doi: https://doi.org/10.1002/(SICI)1521-396X(199903)172:1<265::AID-PSSA265>3.0.CO;2-N.
[117] J. A. Malmonge, L. F. Malmonge, G. C. Fuzari Jr, S. M. Malmonge, and W. K. Sakamoto, "Piezo and dielectric properties of PHB–PZT composite," *Polymer Composites,* https://doi.org/10.1002/pc.20719 vol. 30, no. 9, pp. 1333-1337, 2009/09/01 2009, doi: https://doi.org/10.1002/pc.20719.
[118] W. Nhuapeng and T. Tunkasiri, "Properties of 0–3 Lead Zirconate Titanate–Polymer Composites Prepared in a Centrifuge," *Journal of the American Ceramic Society,* vol. 85, no. 3, pp. 700-702, 2002, doi: https://doi.org/10.1111/j.1151-2916.2002.tb00154.x.
[119] Y. Yang *et al.*, "Flexible piezoelectric pressure sensor based on polydopamine-modified BaTiO3/PVDF composite film for human motion monitoring," *Sensors and Actuators A: Physical,* vol. 301, 2020, doi: 10.1016/j.sna.2019.111789.

[120] W. Choi, J. Lee, Y. Kyoung Yoo, S. Kang, J. Kim, and J. Hoon Lee, "Enhanced sensitivity of piezoelectric pressure sensor with microstructured polydimethylsiloxane layer," *Applied Physics Letters,* vol. 104, no. 12, 2014, doi: 10.1063/1.4869816.
[121] Y. K. Fuh, B. S. Wang, and C. Y. Tsai, "Self-Powered Pressure Sensor with fully encapsulated 3D printed wavy substrate and highly-aligned piezoelectric fibers array," *Sci Rep,* vol. 7, no. 1, p. 6759, Jul 28 2017, doi: 10.1038/s41598-017-07360-z.
[122] Y. R. Wang, J. M. Zheng, G. Y. Ren, P. H. Zhang, and C. Xu, "A flexible piezoelectric force sensor based on PVDF fabrics," *Smart Materials and Structures,* vol. 20, no. 4, 2011, doi: 10.1088/0964-1726/20/4/045009.
[123] T. Sharma, S.-S. Je, B. Gill, and J. X. J. Zhang, "Patterning piezoelectric thin film PVDF–TrFE based pressure sensor for catheter application," *Sensors and Actuators A: Physical,* vol. 177, pp. 87-92, 2012, doi: 10.1016/j.sna.2011.08.019.
[124] E. J. Curry *et al.*, "Biodegradable Piezoelectric Force Sensor," *Proc Natl Acad Sci U S A,* vol. 115, no. 5, pp. 909-914, Jan 30 2018, doi: 10.1073/pnas.1710874115.
[125] M. Akiyama *et al.*, "Flexible piezoelectric pressure sensors using oriented aluminum nitride thin films prepared on polyethylene terephthalate films," *Journal of Applied Physics,* vol. 100, no. 11, 2006, doi: 10.1063/1.2401312.
[126] Y. Ting, Suprapto, A. Nugraha, C. W. Chiu, and H. Gunawan, "Design and characterization of one-layer PVDF thin film for a 3D force sensor," *Sensors and Actuators A: Physical,* vol. 250, pp. 129-137, 2016, doi: 10.1016/j.sna.2016.09.025.
[127] S. Saha, V. Yauvana, S. Chakraborty, and D. Sanyal, "Synthesis and Characterization of Polyvinylidene-fluoride (PVDF) Nanofiber for Application as Piezoelectric Force Sensor," *Materials Today: Proceedings,* vol. 18, pp. 1450-1458, 2019, doi: 10.1016/j.matpr.2019.06.613.
[128] M. A. Qasaimeh, S. Sokhanvar, J. Dargahi, and M. Kahrizi, "PVDF-Based Microfabricated Tactile Sensor for Minimally Invasive Surgery," *Journal of Microelectromechanical Systems,* vol. 18, no. 1, pp. 195-207, 2009, doi: 10.1109/jmems.2008.2008559.
[129] C. Lee and J. A. Tarbutton, "Polyvinylidene fluoride (PVDF) direct printing for sensors and actuators," *The International Journal of Advanced Manufacturing Technology,* vol. 104, no. 5-8, pp. 3155-3162, 2019, doi: 10.1007/s00170-019-04275-z.
[130] H. Kim *et al.*, "Increased piezoelectric response in functional nanocomposites through multiwall carbon nanotube interface and fused-deposition modeling three-dimensional printing," *MRS Communications,* vol. 7, no. 4, pp. 960-966, 2017, doi: 10.1557/mrc.2017.126.
[131] H. Kim *et al.*, "3D printing of polyvinylidene fluoride/photopolymer resin blends for piezoelectric pressure sensing application using the stereolithography technique," *MRS Communications,* vol. 9, no. 3, pp. 1115-1123, 2019.
[132] X. Zhou, K. Parida, O. Halevi, S. Magdassi, and P. S. Lee, "All 3D printed stretchable piezoelectric nanogenerator for self-powered sensor application," *Sensors,* vol. 20, no. 23, p. 6748, 2020.
[133] G. Kalimuldina *et al.*, "A Review of Piezoelectric PVDF Film by Electrospinning and Its Applications," *Sensors,* vol. 20, no. 18, 2020, doi: 10.3390/s20185214.
[134] Y. Zheng, "3 - Fabrication on bioinspired surfaces," in *Bioinspired Design of Materials Surfaces*, Y. Zheng Ed.: Elsevier, 2019, pp. 99-146.
[135] F. Hubenthal, "1.13 - Noble Metal Nanoparticles: Synthesis and Optical Properties," in *Comprehensive Nanoscience and Technology*, D. L. Andrews, G. D. Scholes, and G. P. Wiederrecht Eds. Amsterdam: Academic Press, 2011, pp. 375-435.
[136] S. H. Masood, "10.04 - Advances in Fused Deposition Modeling," in *Comprehensive Materials Processing*, S. Hashmi, G. F. Batalha, C. J. Van Tyne, and B. Yilbas Eds. Oxford: Elsevier, 2014, pp. 69-91.

[137] C. J. Bettinger, J. T. Borenstein, and R. Langer, "Chapter Twenty-Four - Micro- and Nanofabricated Scaffolds," in *Principles of Tissue Engineering (Third Edition)*, R. Lanza, R. Langer, and J. Vacanti Eds. Burlington: Academic Press, 2007, pp. 341-358.
[138] O. Mohamed, "Optimization of fused deposition modeling process parameters: a review of current research and future prospects," *Advances in Manufacturing,* vol. 3, pp. 42-52, 02/25 2015, doi: 10.1007/s40436-014-0097-7.
[139] H. Kim, F. Torres, D. Villagran, C. Stewart, Y. Lin, and T.-L. B. Tseng, "3D Printing of BaTiO3 /PVDF Composites with Electric In Situ Poling for Pressure Sensor Applications," *Macromolecular Materials and Engineering,* vol. 302, no. 11, 2017, doi: 10.1002/mame.201700229.
[140] J. Tarbuttona, T. Leb, G. Helfrichb, and M. Kirkpatrickb, "Phase transformation and shock sensor response of additively manufactured piezoelectric PVDF," *Procedia Manufacturing,* vol. 10, pp. 982-989, 2017.
[141] X. Wang, M. Jiang, Z. Zhou, J. Gou, and D. Hui, "3D printing of polymer matrix composites: A review and prospective," *Composites Part B: Engineering,* vol. 110, pp. 442-458, 2017/02/01/ 2017, doi: https://doi.org/10.1016/j.compositesb.2016.11.034.
[142] A. Muzaffar, M. B. Ahamed, K. Deshmukh, T. Kovářík, T. Křenek, and S. K. K. Pasha, "Chapter 4 - 3D and 4D printing of pH-responsive and functional polymers and their composites," in *3D and 4D Printing of Polymer Nanocomposite Materials*, K. K. Sadasivuni, K. Deshmukh, and M. A. Almaadeed Eds.: Elsevier, 2020, pp. 85-117.
[143] J. C. Najmon, S. Raeisi, and A. Tovar, "2 - Review of additive manufacturing technologies and applications in the aerospace industry," in *Additive Manufacturing for the Aerospace Industry*, F. Froes and R. Boyer Eds.: Elsevier, 2019, pp. 7-31.
[144] J. L. Walker and M. Santoro, "9 - Processing and production of bioresorbable polymer scaffolds for tissue engineering," in *Bioresorbable Polymers for Biomedical Applications*, G. Perale and J. Hilborn Eds.: Woodhead Publishing, 2017, pp. 181-203.
[145] P. X. Ma and J. Elisseeff, *Scaffolding in tissue engineering*. CRC press, 2005.
[146] J. W. Lee, J. Y. Kim, and D.-W. Cho, "Solid free-form fabrication technology and its application to bone tissue engineering," *International journal of stem cells,* vol. 3, no. 2, p. 85, 2010.
[147] C. Chen *et al.*, "Additive Manufacturing of Piezoelectric Materials," *Advanced Functional Materials,* https://doi.org/10.1002/adfm.202005141 vol. 30, no. 52, p. 2005141, 2020/12/01 2020, doi: https://doi.org/10.1002/adfm.202005141.
[148] J. T. Huh, J. J. Yoo, A. Atala, and S. J. Lee, "Chapter 74 - Three-dimensional bioprinting for tissue engineering," in *Principles of Tissue Engineering (Fifth Edition)*, R. Lanza, R. Langer, J. P. Vacanti, and A. Atala Eds.: Academic Press, 2020, pp. 1391-1415.
[149] F. P. Melchels, J. Feijen, and D. W. Grijpma, "A review on stereolithography and its applications in biomedical engineering," *Biomaterials,* vol. 31, no. 24, pp. 6121-6130, 2010.
[150] A. Sotov, A. Kantyukov, A. Popovich, and V. Sufiiarov, "LCD-SLA 3D printing of BaTiO3 piezoelectric ceramics," *Ceramics International,* 2021/07/22/ 2021, doi: https://doi.org/10.1016/j.ceramint.2021.07.216.
[151] W. Chen, F. Wang, K. Yan, Y. Zhang, and D. Wu, "Micro-stereolithography of KNN-based lead-free piezoceramics," *Ceramics International,* vol. 45, no. 4, pp. 4880-4885, 2019/03/01/ 2019, doi: https://doi.org/10.1016/j.ceramint.2018.11.185.
[152] Y. Chen *et al.*, "PZT ceramics fabricated based on stereolithography for an ultrasound transducer array application," *Ceramics International,* vol. 44, no. 18, pp. 22725-22730, 2018/12/15/ 2018, doi: https://doi.org/10.1016/j.ceramint.2018.09.055.
[153] A. Mostafaei *et al.*, "Binder jet 3D printing—Process parameters, materials, properties, modeling, and challenges," *Progress in Materials Science,* vol. 119, p. 100707, 2021.
[154] S. M. Allen and E. M. Sachs, "Three-dimensional printing of metal parts for tooling and other applications," *Metals and Materials,* vol. 6, no. 6, pp. 589-594, 2000.

[155] Y. Zhang, W. Jarosinski, Y.-G. Jung, and J. Zhang, "2 - Additive manufacturing processes and equipment," in *Additive Manufacturing*, J. Zhang and Y.-G. Jung Eds.: Butterworth-Heinemann, 2018, pp. 39-51.
[156] A. Farzadi, M. Solati-Hashjin, M. Asadi-Eydivand, and N. A. Abu Osman, "Effect of Layer Thickness and Printing Orientation on Mechanical Properties and Dimensional Accuracy of 3D Printed Porous Samples for Bone Tissue Engineering," *PLOS ONE,* vol. 9, no. 9, p. e108252, 2014, doi: 10.1371/journal.pone.0108252.
[157] S. M. Gaytan *et al.*, "Fabrication of barium titanate by binder jetting additive manufacturing technology," *Ceramics International,* vol. 41, no. 5, Part A, pp. 6610-6619, 2015/06/01/ 2015, doi: https://doi.org/10.1016/j.ceramint.2015.01.108.
[158] P. Saxena and P. Shukla, "A comprehensive review on fundamental properties and applications of poly(vinylidene fluoride) (PVDF)," *Advanced Composites and Hybrid Materials,* vol. 4, no. 1, pp. 8-26, 2021/03/01 2021, doi: 10.1007/s42114-021-00217-0.
[159] G.-d. Kang and Y.-m. Cao, "Application and modification of poly(vinylidene fluoride) (PVDF) membranes – A review," *Journal of Membrane Science,* vol. 463, pp. 145-165, 2014/08/01/ 2014, doi: https://doi.org/10.1016/j.memsci.2014.03.055.
[160] F. Mullaveettil, R. Dauksevicius, M. Rimasauskas, and V. Grigaliunas, "Fused filament fabrication and mechanical performance of PVDF-based specialty thermoplastics," *The International Journal of Advanced Manufacturing Technology,* 08/27 2021, doi: 10.1007/s00170-021-07887-6.
[161] L. Wu *et al.*, "Recent advances in the preparation of PVDF-based piezoelectric materials," *Nanotechnology Reviews,* vol. 11, no. 1, pp. 1386-1407, 2022, doi: doi:10.1515/ntrev-2022-0082.
[162] S. Abbrent, J. Plestil, D. Hlavata, J. Lindgren, J. Tegenfeldt, and Å. Wendsjö, "Crystallinity and morphology of PVdF–HFP-based gel electrolytes," *Polymer,* vol. 42, no. 4, pp. 1407-1416, 2001/02/01/ 2001, doi: https://doi.org/10.1016/S0032-3861(00)00517-6.
[163] K. Polat, "Energy harvesting from a thin polymeric film based on PVDF-HFP and PMMA blend," *Applied Physics A,* vol. 126, no. 7, p. 497, 2020/06/08 2020, doi: 10.1007/s00339-020-03698-w.
[164] B. S. Lalia, E. Guillen-Burrieza, H. A. Arafat, and R. Hashaikeh, "Fabrication and characterization of polyvinylidenefluoride-co-hexafluoropropylene (PVDF-HFP) electrospun membranes for direct contact membrane distillation," *Journal of Membrane Science,* vol. 428, pp. 104-115, 2013/02/01/ 2013, doi: https://doi.org/10.1016/j.memsci.2012.10.061.
[165] X. Wang, C. Xiao, H. Liu, Q. Huang, and H. Fu, "Fabrication and properties of PVDF and PVDF-HFP microfiltration membranes," *Journal of Applied Polymer Science,* https://doi.org/10.1002/app.46711 vol. 135, no. 40, p. 46711, 2018/10/20 2018, doi: https://doi.org/10.1002/app.46711.
[166] X. He, K. Yao, and B. K. Gan, "Phase transition and properties of a ferroelectric poly(vinylidene fluoride-hexafluoropropylene) copolymer," *Journal of Applied Physics,* vol. 97, no. 8, p. 084101, 2005/04/15 2005, doi: 10.1063/1.1862323.
[167] Y. Huan, Y. Liu, and Y. Yang, "Simultaneous stretching and static electric field poling of poly (vinylidene fluoride-hexafluoropropylene) copolymer films," *Polymer Engineering & Science,* vol. 47, no. 10, pp. 1630-1633, 2007.
[168] F. Oliveira *et al.*, "Process influences on the structure, piezoelectric, and gas-barrier properties of PVDF-TrFE copolymer," *Journal of Polymer Science Part B: Polymer Physics,* vol. 52, no. 7, pp. 496-506, 2014, doi: https://doi.org/10.1002/polb.23443.
[169] K. Tashiro, K. Takano, M. Kobayashi, Y. Chatani, and H. Tadokoro, "Structure and ferroelectric phase transition of vinylidene fluoride-trifluoroethylene copolymers: 2. VDF 55% copolymer," *Polymer,* vol. 25, no. 2, pp. 195-208, 1984/02/01/ 1984, doi: https://doi.org/10.1016/0032-3861(84)90326-4.

[170] K. Omote, H. Ohigashi, and K. Koga, "Temperature dependence of elastic, dielectric, and piezoelectric properties of “single crystalline’’ films of vinylidene fluoride trifluoroethylene copolymer," *Journal of Applied Physics,* vol. 81, no. 6, pp. 2760-2769, 1997, doi: 10.1063/1.364300.
[171] X. Hu, M. You, N. Yi, X. Zhang, and Y. Xiang, "Enhanced Piezoelectric Coefficient of PVDF-TrFE Films via In Situ Polarization," (in English), *Frontiers in Energy Research,* Original Research vol. 9, 2021-August-10 2021, doi: 10.3389/fenrg.2021.621540.
[172] C. Ribeiro *et al.*, "Electroactive poly(vinylidene fluoride)-based structures for advanced applications," *Nature Protocols,* vol. 13, no. 4, pp. 681-704, 2018/04/01 2018, doi: 10.1038/nprot.2017.157.
[173] J. C. Barbosa, J. P. Dias, S. Lanceros-Méndez, and C. M. Costa, "Recent Advances in Poly(vinylidene fluoride) and Its Copolymers for Lithium-Ion Battery Separators," (in eng), *Membranes (Basel),* vol. 8, no. 3, Jul 19 2018, doi: 10.3390/membranes8030045.
[174] L. Yang *et al.*, "Flexible polyvinylidene fluoride based nanocomposites with high and stable piezoelectric performance over a wide temperature range utilizing the strong multi-interface effect," *Composites Science and Technology,* vol. 174, pp. 33-41, 2019/04/12/ 2019, doi: https://doi.org/10.1016/j.compscitech.2019.02.014.
[175] PiezoPVDF. https://piezopvdf.com/PVDF-TrFE-Copolymer-20-gram/ (accessed 11 October, 2023).
[176] Sigma Aldrich. https://www.sigmaaldrich.com/EG/en/product/aldrich/427152 (accessed 11 october, 2023).
[177] F. N. Mullaveettil, R. Dauksevicius, M. Rimasauskas, and V. Grigaliunas, "Fused filament fabrication and mechanical performance of PVDF-based specialty thermoplastics," *The International Journal of Advanced Manufacturing Technology,* vol. 117, no. 11, pp. 3267-3280, 2021.
[178] Wikipedia contributors. "Photolithography." Wikipedia, The Free Encyclopedia. https://en.wikipedia.org/w/index.php?title=Photolithography&oldid=1041506530 (accessed September 7 2021).
[179] OpenWetWare contributors. "Photolithography:Patterned Surfaces." OpenWetWare. https://openwetware.org/mediawiki/index.php?title=Photolithography:Patterned_Surfaces&oldid=939568 (accessed September 7, 2021).
[180] "Electrospinning." Laboratory of Polymers & Biomaterials. http://polybiolab.ippt.pan.pl/18-few-words-about/17-electrospinning (accessed September 6, 2021).
[181] M. Kitsara *et al.*, "Permanently hydrophilic, piezoelectric PVDF nanofibrous scaffolds promoting unaided electromechanical stimulation on osteoblasts," *Nanoscale,* 10.1039/C8NR10384D vol. 11, no. 18, pp. 8906-8917, 2019, doi: 10.1039/C8NR10384D.
[182] N. D. Tien, S. P. Lyngstadaas, J. F. Mano, J. J. Blaker, and H. J. Haugen, "Recent Developments in Chitosan-Based Micro/Nanofibers for Sustainable Food Packaging, Smart Textiles, Cosmeceuticals, and Biomedical Applications," (in eng), *Molecules,* vol. 26, no. 9, p. 2683, 2021, doi: 10.3390/molecules26092683.
[183] L. Wannatong, A. Sirivat, and P. Supaphol, "Effects of solvents on electrospun polymeric fibers: preliminary study on polystyrene," *Polymer International,* https://doi.org/10.1002/pi.1599 vol. 53, no. 11, pp. 1851-1859, 2004/11/01 2004, doi: https://doi.org/10.1002/pi.1599.
[184] X. Shi *et al.*, "Electrospinning of Nanofibers and Their Applications for Energy Devices," *Journal of Nanomaterials,* vol. 2015, p. 140716, 2015/05/25 2015, doi: 10.1155/2015/140716.
[185] B. Utela, D. Storti, R. Anderson, and M. Ganter, "A review of process development steps for new material systems in three dimensional printing (3DP)," *Journal of Manufacturing Processes,* vol. 10, no. 2, pp. 96-104, 2008.

[186] M. Ziaee and N. Crane, "Binder jetting: A review of process, materials, and methods," *Additive manufacturing,* vol. 28, pp. 781-801, 2019.
[187] A. Mostafaei, E. L. Stevens, J. J. Ference, D. E. Schmidt, and M. Chmielus, "Binder jet printing of partial denture metal framework from metal powder," *Mater. Sci. Technol,* pp. 289-291, 2017.
[188] T. D. Ngo, A. Kashani, G. Imbalzano, K. T. Q. Nguyen, and D. Hui, "Additive manufacturing (3D printing): A review of materials, methods, applications and challenges," *Composites Part B: Engineering,* vol. 143, pp. 172-196, 2018/06/15/ 2018, doi: https://doi.org/10.1016/j.compositesb.2018.02.012.
[189] D. A. Porter, T. V. Hoang, and T. A. Berfield, "Effects of in-situ poling and process parameters on fused filament fabrication printed PVDF sheet mechanical and electrical properties," *Additive Manufacturing,* vol. 13, pp. 81-92, 2017.
[190] N. Momenzadeh, "Influences of material extrusion additive manufacturing (MEAM) parameters and additives on polyvinylidene fluoride (PVDF) properties," 2020.
[191] A. A. Samy, A. Golbang, E. Harkin-Jones, E. Archer, D. Tormey, and A. McIlhagger, "Finite element analysis of residual stress and warpage in a 3D printed semi-crystalline polymer: Effect of ambient temperature and nozzle speed," *Journal of Manufacturing Processes,* vol. 70, pp. 389-399, 2021/10/01/ 2021, doi: https://doi.org/10.1016/j.jmapro.2021.08.054.
[192] E. V. Diederichs, M. C. Picard, B. P. Chang, M. Misra, D. F. Mielewski, and A. K. Mohanty, "Strategy To Improve Printability of Renewable Resource-Based Engineering Plastic Tailored for FDM Applications," *ACS Omega,* vol. 4, no. 23, pp. 20297-20307, 2019/12/03 2019, doi: 10.1021/acsomega.9b02795.
[193] A. K. Sood, R. K. Ohdar, and S. S. Mahapatra, "Parametric appraisal of mechanical property of fused deposition modelling processed parts," *Materials & Design,* vol. 31, no. 1, pp. 287-295, 2010/01/01/ 2010, doi: https://doi.org/10.1016/j.matdes.2009.06.016.
[194] H. Kim, F. Torres, Y. Wu, D. Villagran, Y. Lin, and T.-L. Tseng, "Integrated 3D printing and corona poling process of PVDF piezoelectric films for pressure sensor application," *Smart Materials and Structures,* vol. 26, no. 8, p. 085027, 2017/07/13 2017, doi: 10.1088/1361-665x/aa738e.
[195] H. K. Dave, *Fused Deposition Modeling Based 3D Printing*. Springer Nature, 2021.
[196] F. M. Mwema and E. T. Akinlabi, "Basics of Fused Deposition Modelling (FDM)," in *Fused Deposition Modeling: Strategies for Quality Enhancement*, F. M. Mwema and E. T. Akinlabi Eds. Cham: Springer International Publishing, 2020, pp. 1-15.
[197] I. Gibson, D. W. Rosen, B. Stucker, and M. Khorasani, *Additive manufacturing technologies*. Springer, 2021.
[198] A. Ikei, J. Wissman, G. Yesner, and C. Rohde, "3D Printed PVDF," *arXiv preprint arXiv:2102.13084,* 2021.
[199] C. Lee and J. A. Tarbutton, "Electric poling-assisted additive manufacturing process for PVDF polymer-based piezoelectric device applications," *Smart Materials and Structures,* vol. 23, no. 9, p. 095044, 2014/08/15 2014, doi: 10.1088/0964-1726/23/9/095044.
[200] H. Kim *et al.*, "Increased piezoelectric response in functional nanocomposites through multiwall carbon nanotube interface and fused-deposition modeling three-dimensional printing," *MRS Communications,* vol. 7, no. 4, pp. 960-966, 2017, doi: 10.1557/mrc.2017.126.
[201] Nile Polymers. "Flourinar C PVDF Print Settings." https://nilepolymers.com/fluorinar-c-kynar-filament/ (accessed 13 October, 2023).
[202] J. Li, F. Yang, Y. Long, Y. Dong, Y. Wang, and X. Wang, "Bulk ferroelectric metamaterial with enhanced piezoelectric and biomimetic mechanical properties from additive manufacturing," *ACS nano,* vol. 15, no. 9, pp. 14903-14914, 2021.
[203] G. W. Cobb, *Introduction to design and analysis of experiments*. Springer, 1998.
[204] D. C. Montgomery, *Design and analysis of experiments*. John wiley & sons, 2017.

[205] C. J. Wu and M. S. Hamada, *Experiments: planning, analysis, and optimization*. John Wiley & Sons, 2011.
[206] K. P. Menard and N. Menard, *Dynamic mechanical analysis*. CRC press, 2020.
[207] K. D. Vernon-Parry, "Scanning electron microscopy: an introduction," *III-Vs Review,* vol. 13, no. 4, pp. 40-44, 2000/07/01/ 2000, doi: https://doi.org/10.1016/S0961-1290(00)80006-X.
[208] P. Gabbott, "A practical introduction to differential scanning calorimetry," *Principles and applications of thermal analysis,* pp. 1-50, 2008.
[209] H. Kim, F. Torres, D. Villagran, C. Stewart, Y. Lin, and T. L. B. Tseng, "3D printing of BaTiO3/PVDF composites with electric in situ poling for pressure sensor applications," *Macromolecular Materials and Engineering,* vol. 302, no. 11, p. 1700229, 2017.
[210] I. Y. Dmitriev, V. K. Lavrentyev, and G. K. Elyashevich, "Polymorphic transformations in poly(vinylidene fluoride) films during orientation," *Polymer Science Series A,* vol. 48, no. 3, pp. 272-277, 2006/03/01 2006, doi: 10.1134/S0965545X06030084.
[211] H. Kim, T. Fernando, M. Li, Y. Lin, and T.-L. B. Tseng, "Fabrication and characterization of 3D printed BaTiO3/PVDF nanocomposites," *Journal of Composite Materials,* vol. 52, no. 2, pp. 197-206, 2018, doi: 10.1177/0021998317704709.
[212] Y. Yang *et al.*, "Flexible piezoelectric pressure sensor based on polydopamine-modified BaTiO3/PVDF composite film for human motion monitoring," *Sensors and Actuators A: Physical,* vol. 301, p. 111789, 2020/01/01/ 2020, doi: https://doi.org/10.1016/j.sna.2019.111789.
[213] R. Gonçalves *et al.*, "Nucleation of the electroactive β-phase, dielectric and magnetic response of poly(vinylidene fluoride) composites with Fe2O3 nanoparticles," *Journal of Non-Crystalline Solids,* vol. 361, pp. 93-99, 2013/02/01/ 2013, doi: https://doi.org/10.1016/j.jnoncrysol.2012.11.003.
[214] P. K. Panda and B. Sahoo, "PZT to Lead Free Piezo Ceramics: A Review," *Ferroelectrics,* vol. 474, no. 1, pp. 128-143, 2015/01/02 2015, doi: 10.1080/00150193.2015.997146.
[215] Z.-Y. Shen and J.-F. Li, "Enhancement of piezoelectric constant d33 in BaTiO3 ceramics due to nano-domain structure," *Journal of the Ceramic Society of Japan,* vol. 118, no. 1382, pp. 940-943, 2010.
[216] K. Wang and J.-F. Li, "(K, Na)NbO3-based lead-free piezoceramics: Phase transition, sintering and property enhancement," *Journal of Advanced Ceramics,* vol. 1, no. 1, pp. 24-37, 2012/03/01 2012, doi: 10.1007/s40145-012-0003-3.
[217] K. Denishev, "Some metal oxides and their applications for creation of Microsystems (MEMS) and Energy Harvesting Devices (EHD)," *Journal of Physics: Conference Series,* vol. 764, no. 1, p. 012003, 2016/10/01 2016, doi: 10.1088/1742-6596/764/1/012003.
[218] M. C. Tanzi, S. Farè, and G. Candiani, "Chapter 1 - Organization, Structure, and Properties of Materials," in *Foundations of Biomaterials Engineering*, M. C. Tanzi, S. Farè, and G. Candiani Eds.: Academic Press, 2019, pp. 3-103.
[219] H. Jäger, W. Frohs, G. Collin, F. von Sturm, O. Vohler, and G. Nutsch, "Carbon, 1. General," *Ullmann's Encyclopedia of Industrial Chemistry,* 2000.
[220] H. C. Bidsorkhi *et al.*, "Nucleation effect of unmodified graphene nanoplatelets on PVDF/GNP film composites," *Materials Today Communications,* vol. 11, pp. 163-173, 2017/06/01/ 2017, doi: https://doi.org/10.1016/j.mtcomm.2017.04.001.
[221] S. Manna and A. K. Nandi, "Piezoelectric β Polymorph in Poly(vinylidene fluoride)-Functionalized Multiwalled Carbon Nanotube Nanocomposite Films," *The Journal of Physical Chemistry C,* vol. 111, no. 40, pp. 14670-14680, 2007/10/01 2007, doi: 10.1021/jp073102l.
[222] R. K. Layek, S. Samanta, D. P. Chatterjee, and A. K. Nandi, "Physical and mechanical properties of poly (methyl methacrylate)-functionalized graphene/poly (vinylidine fluoride) nanocomposites: Piezoelectric β polymorph formation," *Polymer,* vol. 51, no. 24, pp. 5846-5856, 2010.

[223] M. El Achaby, F. Z. Arrakhiz, S. Vaudreuil, E. M. Essassi, and A. Qaiss, "Piezoelectric β-polymorph formation and properties enhancement in graphene oxide – PVDF nanocomposite films," *Applied Surface Science,* vol. 258, no. 19, pp. 7668-7677, 2012/07/15/ 2012, doi: https://doi.org/10.1016/j.apsusc.2012.04.118.
[224] O. Agboola, E. R. Sadiku, and T. Mokrani, "Chapter 10 - Carbon Containing Nanostructured Polymer Blends," in *Design and Applications of Nanostructured Polymer Blends and Nanocomposite Systems*, S. Thomas, R. Shanks, and S. Chandrasekharakurup Eds. Boston: William Andrew Publishing, 2016, pp. 187-213.
[225] G. Mittal, V. Dhand, K. Y. Rhee, S.-J. Park, and W. R. Lee, "A review on carbon nanotubes and graphene as fillers in reinforced polymer nanocomposites," *Journal of Industrial and Engineering Chemistry,* vol. 21, pp. 11-25, 2015/01/25/ 2015, doi: https://doi.org/10.1016/j.jiec.2014.03.022.
[226] N. Domun, H. Hadavinia, T. Zhang, T. Sainsbury, G. H. Liaghat, and S. Vahid, "Improving the fracture toughness and the strength of epoxy using nanomaterials – a review of the current status," *Nanoscale,* 10.1039/C5NR01354B vol. 7, no. 23, pp. 10294-10329, 2015, doi: 10.1039/C5NR01354B.
[227] H. M. Ning *et al.*, "Improved piezoelectric properties of poly(vinylidene fluoride) nanocomposites containing multi-walled carbon nanotubes," *Smart Materials and Structures,* vol. 22, no. 6, p. 065011, 2013/04/30 2013, doi: 10.1088/0964-1726/22/6/065011.
[228] J. M. MARTÍN-MARTÍNEZ, "Rubber base adhesives," in *Adhesion science and engineering*: Elsevier, 2002, pp. 573-675.
[229] G. Wypych, *Handbook of fillers*. ChemTec Pub. Toronto, 2010.
[230] F. Çeçen, "Activated carbon," *Kirk-Othmer Encyclopedia of Chemical Technology,* pp. 1-34, 2000.
[231] S. R. Klaus, J. Neubauer, and F. Goetz-Neunhoeffer, "Influence of the specific surface area of alumina fillers on CAC hydration kinetics," *Advances in Cement Research,* vol. 28, no. 1, pp. 62-70, 2016, doi: 10.1680/jadcr.15.00012.
[232] https://www.differencebetween.com/difference-between-carbon-black-and-activated-carbon/#:~:text=The%20key%20difference%20between%20carbon%20black%20and%20activated,products%20while%20activated%20carbon%20is%20produced%20from%20charcoal. (accessed 3 Jan, 2022).
[233] L. Wu *et al.*, "Improved piezoelectricity of PVDF-HFP/carbon black composite films," *Journal of Physics D: Applied Physics,* vol. 47, no. 13, p. 135302, 2014/03/11 2014, doi: 10.1088/0022-3727/47/13/135302.
[234] J. Cai *et al.*, "Preparing carbon black/graphene/PVDF-HFP hybrid composite films of high piezoelectricity for energy harvesting technology," *Composites Part A: Applied Science and Manufacturing,* vol. 121, pp. 223-231, 2019.
[235] Sigma Aldrich. https://www.sigmaaldrich.com/EG/en/product/aldrich/699632 (accessed November 20, 2023).
[236] Sigma Aldrich. https://www.sigmaaldrich.com/EG/en/product/sial/05105 (accessed November 21, 2023).
[237] S. Satapathy, P. K. Gupta, S. Pawar, and K. B. R. Varma, "Crystallization of Beta-phase Poly (vinylidene fluoride) films using dimethyl sulfoxide (DMSO) solvent and at suitable annealing condition," *arXiv: Materials Science,* 2008.
[238] M. J. Anderson, P. J. Whitcomb, and M. A. Bezener, *Formulation simplified: finding the sweet spot through design and analysis of experiments with mixtures*. Productivity Press, 2018.
[239] reliawiki. "Mixture Design." https://reliawiki.org/index.php/Mixture_Design (accessed May 29, 2022).
[240] N. I. Mohamad Zen, S. S. Abd Gani, R. Shamsudin, and H. R. Fard Masoumi, "The Use of D-Optimal Mixture Design in Optimizing Development of Okara Tablet Formulation as a Dietary

Supplement," *The Scientific World Journal,* vol. 2015, p. 684319, 2015/06/11 2015, doi: 10.1155/2015/684319.
[241] Z. Jeirani, B. M. Jan, B. S. Ali, I. M. Noor, S. C. Hwa, and W. Saphanuchart, "The optimal mixture design of experiments: Alternative method in optimizing the aqueous phase composition of a microemulsion," *Chemometrics and Intelligent Laboratory Systems,* vol. 112, pp. 1-7, 2012.
[242] G. H. Kim, S. M. Hong, and Y. Seo, "Piezoelectric properties of poly (vinylidene fluoride) and carbon nanotube blends: β-phase development," *Physical chemistry chemical physics,* vol. 11, no. 44, pp. 10506-10512, 2009.
[243] N. Levi, R. Czerw, S. Xing, P. Iyer, and D. L. Carroll, "Properties of polyvinylidene difluoride–carbon nanotube blends," *Nano letters,* vol. 4, no. 7, pp. 1267-1271, 2004.
[244] J. S. Lee *et al.*, "Crystal structure and ferroelectric properties of poly (vinylidene fluoride)-carbon nano tube nanocomposite film," *Molecular Crystals and Liquid Crystals,* vol. 491, no. 1, pp. 247-254, 2008.
[245] L. Wu *et al.*, "Improvement of the piezoelectric properties of PVDF-HFP using AgNWs," *RSC Advances,* 10.1039/C4RA03382E vol. 4, no. 68, pp. 35896-35903, 2014, doi: 10.1039/C4RA03382E.
[246] T. Greeshma, R. Balaji, and S. Jayakumar, "PVDF Phase Formation and Its Influence on Electrical and Structural Properties of PZT-PVDF Composites," *Ferroelectrics Letters Section,* vol. 40, no. 1-3, pp. 41-55, 2013/01/01 2013, doi: 10.1080/07315171.2013.814460.
[247] A. Bouhamed *et al.*, "A hybrid piezoelectric composite flexible film based on PVDF-HFP for boosting power generation," *Composites Science and Technology,* vol. 208, p. 108769, 2021/05/26/ 2021, doi: https://doi.org/10.1016/j.compscitech.2021.108769.
[248] R. Sahoo, S. Mishra, A. Ramadoss, S. Mohanty, S. Mahapatra, and S. K. Nayak, "An approach towards the fabrication of energy harvesting device using Ca-doped ZnO/ PVDF-TrFE composite film," *Polymer,* vol. 205, p. 122869, 2020/09/28/ 2020, doi: https://doi.org/10.1016/j.polymer.2020.122869.
[249] Minitab. "Overview for Response Trace Plot." https://support.minitab.com/en-us/minitab/20/help-and-how-to/statistical-modeling/doe/how-to/mixtures/response-trace-plot/before-you-start/overview/#:~:text=Use%20Response%20Trace%20Plot%2C%20also,reference%20blend%20to%20a%20vertex. (accessed 15 October, 2022).
[250] Minitab. "What is response optimization?" https://support.minitab.com/en-us/minitab/21/help-and-how-to/statistical-modeling/using-fitted-models/supporting-topics/response-optimization/what-is-response-optimization/ (accessed 20 October, 2022).
[251] H. Kim, J. Johnson, L. A. Chavez, C. A. Garcia Rosales, T.-L. B. Tseng, and Y. Lin, "Enhanced dielectric properties of three phase dielectric MWCNTs/BaTiO3/PVDF nanocomposites for energy storage using fused deposition modeling 3D printing," *Ceramics International,* vol. 44, no. 8, pp. 9037-9044, 2018/06/01/ 2018, doi: https://doi.org/10.1016/j.ceramint.2018.02.107.
[252] S. Lanceros-Mendez, J. Mano, A. Costa, and V. H. Schmidt, "FTIR and DSC studies of mechanically deformed β-PVDF films," *Journal of Macromolecular Science, Part B,* vol. 40, no. 3-4, pp. 517-527, 2001.
[253] S. Vidhate, A. Shaito, J. Chung, and N. A. D'Souza, "Crystallization, mechanical, and rheological behavior of polyvinylidene fluoride/carbon nanofiber composites," *Journal of applied polymer science,* vol. 112, no. 1, pp. 254-260, 2009.
[254] A. Jayswal and S. Adanur, "Effect of heat treatment on crystallinity and mechanical properties of flexible structures 3D printed with fused deposition modeling," *Journal of Industrial Textiles,* vol. 51, no. 2_suppl, pp. 2616S-2641S, 2022.
[255] J. Fu, Y. Hou, M. Zheng, Q. Wei, M. Zhu, and H. Yan, "Improving dielectric properties of PVDF composites by employing surface modified strong polarized BaTiO3 particles derived by

molten salt method," *ACS applied materials & interfaces,* vol. 7, no. 44, pp. 24480-24491, 2015.
[256] X. Liu, S. Xu, X. Kuang, and X. Wang, "Ultra-long MWCNTs highly oriented in electrospun PVDF/MWCNT composite nanofibers with enhanced β phase," *RSC advances,* vol. 6, no. 108, pp. 106690-106696, 2016.
[257] Z. Cui, N. T. Hassankiadeh, Y. Zhuang, E. Drioli, and Y. M. Lee, "Crystalline polymorphism in poly (vinylidenefluoride) membranes," *Progress in Polymer Science,* vol. 51, pp. 94-126, 2015.
[258] H. Guo, Q. Wang, J. Liu, C. Du, and B. Li, "Improved interfacial properties for largely enhanced thermal conductivity of poly (vinylidene fluoride)-based nanocomposites via functionalized multi-wall carbon nanotubes," *Applied Surface Science,* vol. 487, pp. 379-388, 2019.
[259] V. S. Bystrov, E. V. Paramonova, I. K. Bdikin, A. V. Bystrova, R. C. Pullar, and A. L. Kholkin, "Molecular modeling of the piezoelectric effect in the ferroelectric polymer poly (vinylidene fluoride)(PVDF)," *Journal of molecular modeling,* vol. 19, pp. 3591-3602, 2013.
[260] L. Persano *et al.*, "Shear Piezoelectricity in Poly (vinylidenefluoride-co-trifluoroethylene): Full Piezotensor Coefficients by Molecular Modeling, Biaxial Transverse Response, and Use in Suspended Energy-Harvesting Nanostructures," *Advanced Materials,* vol. 28, no. 35, pp. 7633-7639, 2016.
[261] Y.-T. Wang, Y.-C. Hu, and K.-R. Chen, "A flexible polyvinylidene fluoride film-loudspeaker," *J Chin Soc Mech Eng,* vol. 36, pp. 59-66, 2015.